MODELING HOT MIX ASPHALT COMPACTION USING A THERMODYNAMICS BASED COMPRESSIBLE VISCOELASTIC MODEL WITHIN THE FRAMEWORK OF MULTIPLE NATURAL CONFIGURATIONS

A Dissertation

by

SARADHI KONERU

Submitted to the Office of Graduate Studies of
Texas A&M University
in partial fulfillment of the requirements for the degree of

DOCTOR OF PHILOSOPHY

August 2010

Major Subject: Civil Engineering

MODELING HOT MIX ASPHALT COMPACTION USING A THERMODYNAMICS BASED COMPRESSIBLE VISCOELASTIC MODEL WITHIN THE FRAMEWORK OF MULTIPLE NATURAL CONFIGURATIONS

A Dissertation

by

SARADHI KONERU

Submitted to the Office of Graduate Studies of
Texas A&M University
in partial fulfillment of the requirements for the degree of

DOCTOR OF PHILOSOPHY

Approved by:

Co-Chairs of Committee,	Kumbakonam R. Rajagopal
	Eyad Masad
Committee Members,	Athanasios Scarpas
	Jay R. Walton
	Dallas Little
Head of Department,	John Niedzwecki

August 2010

Major Subject: Civil Engineering

ABSTRACT

Modeling Hot Mix Asphalt Compaction Using a Thermodynamics Based Compressible Viscoelastic Model within the Framework of Multiple Natural Configurations. (August 2010)

Saradhi Koneru, B. E., Osmania University, Hyderabad, INDIA

M. S., Texas A&M University, College Station, USA

Co–Chairs of Advisory Committee: K. R. Rajagopal
E. Masad

Hot mix asphalt (HMA) is a composite material that exhibits a nonlinear response that is dependent on temperature, type of loading and strain level. The properties of HMA are highly influenced by the type and amount of the constituents used and also depend on its internal structure. In such a material the variable effects of the compaction process assume a central importance in determining material performance. It is generally accepted that the theoretical knowledge about material behavior during compaction is limited and it is therefore hard to predict and manage (the effect of) a compaction process. This work makes an attempt to address such a specific need by developing a continuum model that can be adapted for simulating the compaction of hot mix asphalt (HMA) using the notion of multiple natural configurations. A thermodynamic framework is employed to study the non-linear dissipative response associated with HMA by specifying the forms for the stored energy and the rate of dissipation function for the material; a viscoelastic compressible fluid model is developed using this framework to model the compaction of hot mix asphalt. It is further anticipated that the present work will aid in the development of better constitutive

models capable of capturing the mechanics of processes like compaction both in the laboratory and in the field. The continuum model developed was implemented in the finite element method, which was employed to setup a simulation environment for hot mix asphalt compaction. The finite element method was used for simulating compaction in the laboratory and in various field compaction projects.

To the never ending quest for knowledge and all the people who have supported me on my journey. It has been a pleasure to learn what I have in this leg of my trip.

ACKNOWLEDGMENTS

I would like to thank my advisors Prof. K. R. Rajagopal and Prof. Eyad Masad for their guidance over the years. I thank Professor Rajagopal who has and will always have a big influence on me as a teacher and a researcher. It was a great privilege to have a man with his depth and breadth of knowledge as my advisor. His classes on mechanics were inspiring and exhilarating. I thank him for his guidance, support and inspiration during the course of my education at this institution.

I thank Professor Masad whose class on bituminous materials guided my very first steps into asphalt mechanics. I appreciate the time and support he has given me all these years and am also very grateful for his help with this work. He has continuously pushed me to improve which has inculcated some good habits.

I am grateful to Prof. Scarpas for his mentorship and guidance with regards to my education in the techniques of finite elements. I greatly value the friendship and help of my colleague Cor Kasbergen without whose skills in programming and quick mathematical calculations as well as his expertise with CAPA-3D, much of the work presented here would not have been possible. Also, I am grateful to Prof. Little and Prof. Walton for serving on my committee.

I greatly appreciate the continued support I have received at a personal and professional level over the years from my friends and colleagues. I am glad to have the support of my dear wife Pritha during the many trying times.

I very much appreciate the efforts of Emad Kassem in collecting all the data I have utilized for the compaction simulations and thank him for making the data readily available to me.

I am grateful for my education in not only applied mechanics but also various other issues during the course of my study at this great institution.

TABLE OF CONTENTS

CHAPTER Page

CHAPTER Page

LIST OF TABLES

TABLE Page

LIST OF FIGURES

FIGURE Page

FIGURE Page

FIGURE Page

FIGURE Page

FIGURE Page

FIGURE Page

LIST OF ALGORITHMS

ALGORITHM Page

CHAPTER I

INTRODUCTION

A. Overview

Compaction is a process by which the volume of a mixture of hot asphalt binder, aggregate rocks, filler materials, and airvoids is reduced by the application of external forces to form a dense mass. This densification causes an increase in the unit weight of the material and improves the aggregate interlock ([4],[5]). The goal of compacting an asphalt pavement is to achieve an optimum air void content, to provide a smooth riding surface and to increase the load-bearing capacity of the material under construction [6]. Improper compaction generally leads to poor performance of the asphalt pavement, even if of all other desirable mixture design characteristics being met. This can lead to a premature irreparable damage to asphalt pavements. Such damage typical manifests in the form of permanent deformation, cracking and moisture damage. Hot Mix Asphalt (HMA) is a non-linear fluid like material at the elevated temperatures compaction is typical performed. The materials slowly transforms to a highly viscous non-linear viscoelastic fluid towards the end of the compaction process. The challenge to modeling compaction is the choice of an appropriate material model capable of representing such a transformation of the asphalt mix.

B. Problem Statement

Compaction is an important process that has significant impact on the performance of asphalt pavements. Poor compaction of asphalt mixtures make them suscepti-

---

The journal model is *IEEE Transactions on Automatic Control.*

ble to the permeation of oxygen and moisture. As a result, these mixtures become more prone to failure mechanisms such as cracking and permanent deformation. This study targets the development of a theoretical and computational platform that can me adapted for the simulation of the asphalt mixture compaction processes: the laboratory compaction through a gyratory compactor and the field compaction through a sequence of rolling passes. There are no effective methods/techniques currently available that address or are capable to address the simulation of these two processes. Efforts have been undertaken in this study to specifically fill this void and provide a reasonable starting point to modeling compaction of HMA. The model developed and employed is an isothermal model, that can be modified in the future to account for non-isothermal phenomena, that is capable of exhibiting compressible viscoelastic fluid like response when stimulated by external mechanical means. The model is then implemented in the finite element method to simulate the conditions most relevant to laboratory and field compaction processes. This study is aimed at providing better understanding of the modeling aspects of HMA compaction and has the potential to lead to development of more general integrated approaches to performance prediction and design improvement of pavements such as the intelligent compaction (I.C) systems. Once an appropriate computer simulation environment is in place, we can quickly adapt it to serve our purposes to provide feedback to the controller of the compaction process in a highway construction project. This provides us the context for the present work.

C. Objectives for Research Project

The primary objectives of this research project are as follows:

- Derive a three dimensional constitutive model for highly compressible viscoelas-

tic materials.

- Implement the constitutive model in finite elements.
- Develop a method to determine the model's parameters.
- Utilize the model implemented in finite element to describe the compaction of five asphalt mixtures under the dynamic forces applied in the Superpave[1] gyratory compactor.
- Utilize the model implemented in finite element to simulate the field compaction of asphalt mixtures.

D. Outline of Dissertation

CHAPTER II: Literature Review

- A review of research on compaction modeling is presented.
- A number of relevant studies on asphalt mixture compaction are presented.

CHAPTER III: Constitutive Model Development

- Details of the constitutive model, utilizing the framework of multiple natural configurations, used for capturing HMA response during compaction are presented.
- The equations of the model are formulated to make them amenable to implementing in finite elements.

[1]SUPERPAVE stands for Superior Performing Asphalt Pavements (Harrigan et. al. [7]).

CHAPTER IV: Numerical Implementation in the Finite Element Method

- Algebraic equations are formed from the governing differential equations obtained from the constitutive specification.
- The implementation of the constitutive model in ABAQUS [8] and CAPA-3D is explained briefly and algorithms to implement the model's system of equations in a general Finite Element (F.E) framework are presented.
- The response of the constitutive model to the application of simple deformations is studied and presented.

CHAPTER V: Simulating SUPERPAVE Gyratory Compaction

- The mechanics involved with SUPERPAVE Gyratory Compaction (SGC) are described briefly.
- The boundary conditions necessary to simulate the SGC process are identified and described.
- Simulations that were performed to study the model response with change in the model parameters are presented.
- Results of a sensitivity analysis are presented to gauge the relevance of the parameters in influencing the compaction response.
- SGC simulations are presented as validation for the F.E model by comparing experimental data at two different angles of compaction in the SGC with the model results.

CHAPTER VI: Simulating Field Rolling Compaction

- The finite element model used for field compaction is described.
- The effects of compaction equipment characteristics such as drum weight, amplitude of applied load and frequency of applied vibratory loads are studied.
- Parametric analysis is performed to gauge if model response correlates to response in the laboratory compaction simulation.
- Sensitivity analysis is performed to identify and to reconcile significant parameters in field compaction simulations with those from the SGC simulations.
- The ability to simulate longitudinal joint modeling is demonstrated.

CHAPTER VII: Conclusions and Recommendations

- Observations of material response of the model considered when subject to simple deformation mechanisms.
- Relevant conclusions are drawn correlating the laboratory and field compaction results.
- Factors that impact laboratory and field compaction processes are presented.
- Suggestions are provided for further model improvement and future work with regards to modeling of HMA compaction.

E. Scope and Limitations

The modeling of asphalt mixtures is a rather extensive and complex task Therefore, it would be too ambitious to consider an attempt at trying to solve all the issues

of the whole problem field in a single research project. Therefore, restrictions have been applied to limit the scope in the current research. Firstly, the material mixture, Hot Mix Asphalt (HMA), is treated as a single continuum. A second restriction is that we have assumed isothermal conditions during laboratory and field compaction processes. The third restriction is that simulations for rolling compaction have only been done considering static steel rolling. Despite these limitations, if the modeling and simulation framework developed here proves to work for HMA for the static steel type rollers, then it is expected that the system can be adapted to work for other mixture-roller combinations.

F. Notation

The notations used in this dissertation are similar to those used in standard continuum mechanics texts. Vectors and tensors (second order and fourth order tensors) are represented with bold faced letters. Therefore we have,

a - A Vector,

T - A Second order tensor,

K - A Fourth order tensor.

The gradient and divergence operator with respect to initial reference configuration are denoted as:

$$\text{Grad } \mathbf{a} = \frac{\partial \mathbf{a}}{\partial \mathbf{X}}, \quad \text{Grad } [\mathbf{a}]_{\mathbf{ij}} = \frac{\partial a_i}{\partial X_j},$$
$$\text{Div } \mathbf{T} = \frac{\partial \mathbf{T}}{\partial \mathbf{X}}, \quad \text{Div } [\mathbf{T}]_{\mathbf{i}} = \frac{\partial T_{ij}}{\partial X_j}.$$

The gradient and divergence operator with respect to current configuration are denoted as:

$$\text{grad } \mathbf{a} = \frac{\partial \mathbf{a}}{\partial \mathbf{x}}, \quad \text{grad } [\mathbf{a}]_{\mathbf{ij}} = \frac{\partial a_i}{\partial x_j},$$
$$\text{div } \mathbf{T} = \frac{\partial \mathbf{T}}{\partial \mathbf{x}}, \quad \text{div } [\mathbf{T}]_{\mathbf{i}} = \frac{\partial T_{ij}}{\partial x_j}.$$

CHAPTER II

REVIEW OF THE LITERATURE

A. Background

HMA is a composite material made up of a mixture of graded aggregate rocks bound together by an asphalt binder along with the presence of airvoids. The nature of this mixture is dependent on the type of each of the constituents selected to prepare the mix. HMA derives it nomenclature form the fact that it is mixed, placed, and compacted at elevated temperatures.

Due to its composition, HMA is reported to display nonlinear response even at small strain and exhibits different response in tension and compression particularly for the case of long duration loading. Also, the extreme temperature sensitivity of HMA causes the effects of a change in temperature to have a more significant impact on the mechanical behavior than changes in the loading magnitude (Brown and Snaith [9]). The deformation resistance of HMA is mainly derived from the aggregate matrix and the viscous asphalt binder matrix. Due to the change in microstructure, either due to mechanical changes such as reduction of the air voids or chemical changes such as aging of the asphalt, the response of the aggregate matrix and the asphalt binder matrix to the traffic loading changes over time. Also, the ability of the pavement to stress relax upon load removal change due to continual changes in the microstructure. This change in microstructure and changes in the loading conditions and the environmental conditions and hence the response are the cause for phenomena such as permanent deformation, fatigue cracking, low temperature cracking and moisture induced damage. It is well known that distress due to permanent deformation is due to the accumulation of deformation under repeated traffic loading, resulting in the

development of longitudinal depression along the pavement. This accumulation of deformation depends to a large extent on the one dimensional densification due to air void reduction and the *flow* of the asphalt mortar matrix. A thorough review of the nature, and uses of HMA and many attempts at modeling the material is presented by Krishnan and Rajagopal [10].

The current approach to flexible pavement design relates the engineering properties of asphalt mixtures to pavement distresses and hence are mostly distress prediction models and not constitutive models as usually understood in mechanics. In these models, some measure of distress, for example, the number of cycles to failure, amount of permanent deformation, is related to material properties assuming the asphalt mixtures to be either linear viscoelastic or linear elastic. However, HMA behaves like a non-linear fluid like material at the elevated temperatures, and slowly transforms to a highly viscous non-linear viscoelastic fluid towards the end of the construction process.

Construction of HMA pavements take advantage of the direct and indirect compacting forces exerted by rollers passing over the loose mix to produce dense layers of structurally durable material. This process is known as *compaction*.

B. Hot Mix Asphalt (HMA) Compaction

Proper construction of roadways requires the pavements be laid down according to certain specifications governing the desirable characteristics for the material. For this purpose, construction of pavements starts with the *compaction* process. Compaction reduces the volume of a mixture of hot asphalt binder, aggregate rocks, and filler materials through an application of external forces to form the required dense impervious mass. The motivation for compacting an asphalt pavement is a desire to

achieve an optimum air void content so as to provide a smooth riding surface and to increase the load-bearing capacity of the material under construction (NAPA [6]). The densification of the mixture, due to compaction, causes an increase in the unit weight of the material and improves the aggregate interlock (Corps of Engineers [4], Roberts et. al. [5]). It has been noted extensively in the literature that improper compaction generally leads to poor performance of the asphalt pavement, even if all other desirable mixture design characteristics are met. This can lead to a premature irreparable damage in asphalt pavements. Such damage typical manifests in the form of permanent deformation, cracking and moisture damage.

1. Factors Affecting Compaction

The compaction process is influenced by many factors including the properties of the materials in the mixture, environmental variables, conditions at the work site, and the method of compaction, as detailed by the Corps of Engineers [4], and summarized in some detail by Kassem [11]. The required compaction effort increases with an increase in aggregate angularity, aggregate size, and aggregate hardness. The grade and amount of asphalt binder also influence the compaction process. A mixture produced with too little amount of asphalt is stiff and usually requires more compaction effort than a mixture with high asphalt binder content. Temperatures of the air, mixture and base are important factors that influence compaction (see the handbook by the U. S. Army Corps of Engineers [4]). Also, the compaction effort increases with an increase in layer thickness.

2. Laboratory Versus Field Compaction

Several studies have attempted to examine the relationship between field compaction methods, laboratory compaction methods and mechanical properties. Consuegra et.

al. [12] and Harvey and Monismith [13] evaluated several laboratory compaction methods based on the relationship between the mechanical properties of laboratory specimens and field cores. These studies provided recommendations on the devices that produce laboratory compacted specimens with properties that better relate to those of field cores. Peterson et. al. [14] evaluated the influence of changing the compaction parameters in the SUPERPAVE Gyratory Compactor (SGC) on the mixture mechanical properties and their correlation with mechanical properties of field cores. The control parameters that were varied in this study were angle of gyration, specimen height, gyratory compaction pressure and temperature of the compaction mold. Peterson et. al. [14] found the angle of gyration to be the most important parameter that influenced the mechanical properties.

Masad et. al. [15] used image analysis techniques to study the air void distribution in the SGC. The results showed that the air void distribution in SGC specimens is not uniform and there is higher air void content at the top and the bottom than in the middle. Tashman et. al. [16] compared the air void distribution and mechanical properties of SGC compacted specimens with field cores compacted using different compaction patterns. Tashman et. al. [16] showed that the compaction parameters in the SGC can be changed in order to improve the relationship between the internal structure (including air void distribution) and mechanical properties of SGC specimens and field cores.

A more detailed compilation of the various factors influencing compaction, compaction methods/techniques and summary evaluation of various studies into the compaction of HMA is presented in Huerne [17] and Kassem [11].

3. Modeling HMA Response

The motivation for most studies on HMA behavior has been to develop models to cater to the need to understand response to distresses to which an HMA pavement is subjected, and to determine some experimental variables characterizing the material. Unlike asphalt, for which models that describe the behavior of viscoelastic fluids have been developed, constitutive specifications of HMA have mostly been related to empirical correlations for different types of distresses. Some, studies assuming HMA to be a viscoelastic material have also been carried out. These studies use either a spring-dashpot analogy in the form of a Burger's model (see, for example, Lee et. al. [18], Saal and Labout [19], Saal [20], Van der Poel [21], Reiner [22], Monismith and Secor [23], Secor and Monismith [24], Pagen [25], Monismith et. al. [26], and Huschek [27]), or some simple form of viscoelastic constitutive equation (see, Davis et. al. [28], Huang [29], Moavenzadeh and Soussou [30], Perl et. al. [31], and Kim and Little [32]).

As has been noted by Krishnan and Rajagopal [10], the deformation resistance of HMA is mainly derived from the aggregate matrix and the viscous asphalt mastic. Due to the change in the microstructure (either due to mechanical changes such as reduction of the air voids or chemical changes such as aging of asphalt), the response of the aggregate matrix and the asphalt mastic to the traffic loading changes with time. Also, the ability of the pavement to stress relax upon load removal changes as the microstructure is continuously modified. This change in microstructure and changes in the loading conditions and the environmental conditions, and hence the response, are the cause for phenomena such as rutting, fatigue cracking, low temperature cracking, and moisture induced damage. For instance, it is well known that the distress due to rutting is due to the *accumulation of deformation* under repeated traffic loading

resulting in the development of ruts longitudinally along the pavement. While most of the studies have not considered the mechanism of densification assuming that the pavement will be compacted well during construction ([33], [34]), the plastic flow of the HMA has been assumed to be dependent on temperature, loading rate, and the loading time interval.

There are quite a few models for HMA which consider the microstructure but as with most of the phenomenological models, they neglect the evolution of the microstructure during the life time or consider it, for instance, by means of some *shift factors*. Nijboer [35] conducted microstructural modeling of HMA using the analogy of soil mechanics, postulating that the entire deformation resistance of bituminous mixes can be explained in terms of initial resistance, internal friction, and viscous resistance. Huschek [27] then used a three phase system consisting of regions characterized by viscosity, modulus of elasticity, and a modulus of plasticity. Van der Poel [36] modeled the behavior of asphalt mixes by calculating the rigidity of concentrated solutions of elastic spheres in an elastic medium, using a method developed for dilute dispersions by Frolich and Sack [37]. Hills [38] developed models for the long time creep behavior of asphalt mixes by characterizing the internal structure of the mix by means of the asphalt film thickness. Cheung et. al. [39] and Deshpande and Cebon([40], [41]) have developed models for HMA mixes using isolated contact models and shear box models. Boutin and Auriault [42] used the analogy of a porous media saturated by a viscoelastic fluid to classify the macroscopic behavior of HMA as biphasic, elastic, and viscoelastic depending upon the ratio of the dimension of the pores to the macroscopic wave length. Florea([43], [44]) used a viscoplastic potential to develop an elastic/ viscoplastic model for bituminous concrete.

Recently, Krishnan and Rao ([45], [46]) made attempts at modeling the air voids reduction of HMA using the continuum theory of mixtures and the theory of linear

elastic material with voids. A thermodynamic framework has been recently put into place which can be used for the constitutive description of HMA. This framework has a reasonably general structure within which a host of dissipative processes can be described. This framework, to model HMA, recognizes the change in the microstructure of the material through the changes in the natural configurations of the body. For our purpose here, we understand that a *natural configuration* is a stress free configuration, with further details of the framework presented in Rajagopal ([47]) and later adopted by Rajagopal and co-workers ([48], [49], [10], and [50]).

4. Compaction Models

Very little research has been directed towards modeling hot mix asphalt (HMA) compaction and the material properties that influence compactability. Guler et al. [51] have proposed the use of a porous elasto-plastic (using a modified Gurson-Tvergaard yield function) compaction model. An incremental constitutive relation for the porous material was formulated for this purpose. The researchers focused on obtaining statistically significant parameters for this constitutive relation and obtaining a correlation between the model parameters and mixture variables, i.e. volumetric properties, particle size. Simple linear models were built to predict the model parameters. The displacement field used to represent 3-D compaction is an approximation of the actual motion in an SGC. Also, the model is formulated assuming small strain theory, is time independent and assumes isothermal conditions (no changes in temperature).

Huerne [17], from the Netherlands, used a modified form of soil critical state theory in modeling asphalt mixture compaction. The critical state theory describes granular material behavior by means of a closed yield locus, which gives a boundary between stress states that cause elastic (recoverable) deformations and plastic (irrecoverable) deformations. Huerne's implementation simulates void reduction by

means of plastic volume changes. The Hveem device was used for determining the model's parameters. This model was developed assuming small strain deformation, and consequently, is limited in modeling the high strains involved in the compaction process. Also, the model has many parameters that are not directly linked to mixture properties.

Krishnan and Rao [45] developed a constitutive model for asphalt mixes using mixture theory to model the one dimensional compaction of asphalt mixtures under a static load. This model utilizes the fundamental balance laws to obtain mathematical relations to describe the performance and characteristics of asphalt mixes. While their work places the modeling within the context of a general framework that takes into account the balance laws of mechanics, it ignores certain critical issues concerning the material response such as the evolution of the microstructure of the material being compacted during the process. Also, such an approach to modeling compaction of HMA is limited by the restrictive experimental techniques available to measure the various mixture properties involved in the model.

In summary, previous attempts to model HMA compaction:

- did not account for changes in the material structure during compaction, either explicitly or implicitly through appropriate choices for the total dissipation.
- were not validated using various laboratory and field loading and boundary conditions.
- did not attempt to develop methods for the determination of the model's parameters based on mixture design and material properties.

Recently some effort has been expended in developing material models to describe HMA behavior (Koneru et. al. [52], Masad et. al. [3]), based on a thermodynamically

consistent methodology by employing the framework of 'multiple natural configurations' formalized by Rajagopal [47]. An account of the model presented by Koneru et. al. [52] is presented in here.

5. Intelligent Compaction

An important motivation for developing a material model to be used in compaction simulations is the concept of intelligent compaction (IC). Moore [53] defines intelligent compaction as a system that applies to a vibratory roller. An IC system automatically adjusts its energy output of the roller so as neither to under-compact or over-compact materials. IC of soil and asphalt layers is a relatively new technology introduced in the USA for compaction control (Rahman et. al. [54]). IC for HMA compaction is in an even more early stage. This new compaction concept is however gaining attention from the asphalt paving industry. The model developed here and its derivative application in a simulation environment can be used for obtaining correlations between pavement designs and model characteristics. This shall enable the decision process in an IC control system for HMA.

CHAPTER III

THERMO-MECHANICAL MODEL FOR HMA

The framework to model HMA recognizes that corresponding to any current configuration of the body, we can have several associated natural configurations. The body would attained possibly one such configuration when the tractions are removed, preferably a stress free state. The specific natural configuration the body would attain depends on the process. For example, perfectly elastic materials have a unique stress free configuration, deferring only by a rigid body motion from each other, and during the deformation the underlying microstructural mechanism does not change and the body returns to the same stress free state upon the removal of applied traction. For a classical viscoelastic material, capable of instantaneous elastic response, we can associate the stress free state obtained by an instantaneous elastic unloading response as a natural configuration. To develop a model for the HMA capable of representing the transformation of the mix (i.e. low-viscosity fluid-like to high-viscosity fluid-like) we begin with the same assumption by associating the natural configuration of the material with the stress free state obtained upon instantaneous elastic unloading. The model developed can be described as an isothermal, compressible, viscoelastic, nonlinear fluid-like model[1].

A. Kinematics

Consider a body B in a configuration $\kappa_r(\mathcal{B})$, Figure 1. For convenience, we shall henceforth use κ_r to denote $\kappa_r(\mathcal{B})$. Let $\mathbf{X}$ denote a typical position of a material point in κ_r. Let $\kappa_{c(t)}$ denote the configuration occupied by the body B at time t. The

[1]The model presented in this Chapter has been adopted from the paper [52] with kind permission from Elsevier

motion of the body is defined as a one-to-one mapping which assigns to each point $\mathbf{X}$ in κ_r a corresponding point $\mathbf{x}$ in $\kappa_{c(t)}$:

$$\mathbf{x} = \chi_{\kappa_r}(\mathbf{X}; t). \tag{A.1}$$

The displacement $\mathbf{u}(\mathbf{X}; t)$ that the particles undergo is given by

$$\mathbf{u}(\mathbf{X}; t) := \mathbf{x}(\mathbf{X}; t) - \mathbf{X} \tag{A.2}$$

The deformation gradient $\mathbf{F}_{\kappa_r}$ is defined through:

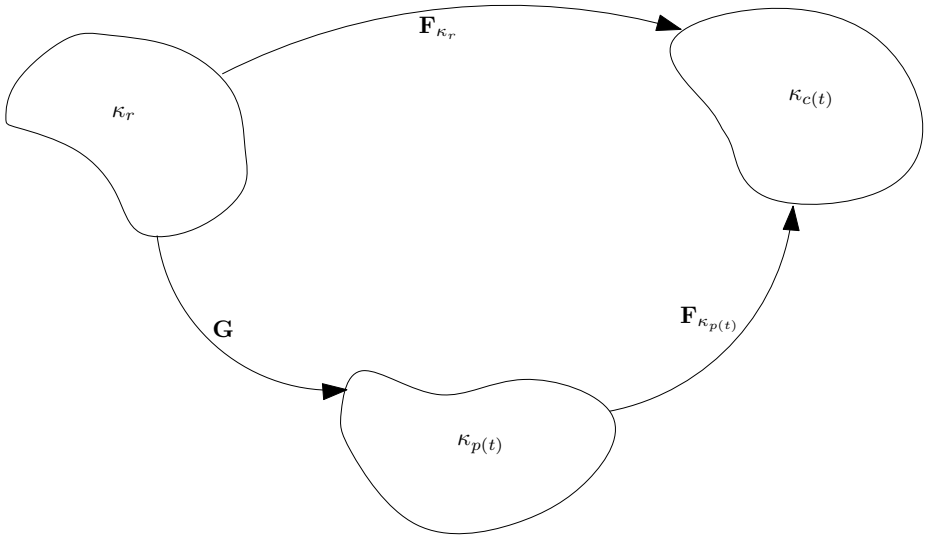

Fig. 1.: Representation of the evolution of 'natural configurations' associated with microstructural transformations resulting from material response to external stimulus

$$\mathbf{F}_{\kappa_r} = \quad \frac{\partial \chi_{\kappa_r}(\mathbf{X}; t)}{\partial \mathbf{X}}. \tag{A.3}$$

We shall assume that $\det(\mathbf{F}_{\kappa_r}) > 0$. It follows from the polar decomposition theorem that,

$$\mathbf{F}_{\kappa_r} = \mathbf{R}_{\kappa_r}\mathbf{U}_{\kappa_r} = \mathbf{V}_{\kappa_r}\mathbf{R}_{\kappa_r}, \tag{A.4}$$

where $\mathbf{R}_{\kappa_r}$ is a proper orthogonal tensor. $\mathbf{U}_{\kappa_r}$, $\mathbf{V}_{\kappa_r}$ are positive definite symmetric tensors.

The left and right Cauchy-Green stretch tensors, $\mathbf{B}_{\kappa_r}$ and $\mathbf{C}_{\kappa_r}$ are defined through:

$$\mathbf{B}_{\kappa_r} := \mathbf{V}^2 = \mathbf{F}_{\kappa_r}\mathbf{F}_{\kappa_r}^T, \tag{A.5}$$

$$\mathbf{C}_{\kappa_r} := \mathbf{U}^2 = \mathbf{F}_{\kappa_r}^T\mathbf{F}_{\kappa_r}. \tag{A.6}$$

The velocity $\mathbf{v}$ of a material point is defined as,

$$\mathbf{v} := \frac{\partial \chi_{\kappa_r}(\mathbf{X};t)}{\partial t}. \tag{A.7}$$

The velocity gradient, Ł, is related to the deformation gradient $\mathbf{F}_{\kappa_r}$ through,

$$Ł := \text{grad}\mathbf{v} = \dot{\mathbf{F}}_{\kappa_r}\mathbf{F}_{\kappa_r}^{-1}. \tag{A.8}$$

The symmetric part of the velocity gradient denoted by $\mathbf{D}$ is given by,

$$\mathbf{D} = \frac{Ł + Ł^T}{2}. \tag{A.9}$$

Now we have,

$$\mathbf{G} := \mathbf{F}_{\kappa_r \to \kappa_{p(t)}} = \mathbf{F}_{\kappa_{p(t)}}^{-1}\mathbf{F}_{\kappa_r}. \tag{A.10}$$

Now, using the conventional definition for the velocity gradient, Ł and defining the velocity gradient $\mathbf{L}_{\kappa_{p(t)}}$ associated with mapping $\mathbf{G}$ through

$$\mathbf{L}_{\kappa_{p(t)}} = \dot{\mathbf{G}}\mathbf{G}^{-1}, \tag{A.11}$$

with its symmetric part given by

$$\mathbf{D}_{\kappa_{p(t)}} = \frac{\mathbf{L}_{\kappa_{p(t)}} + \mathbf{L}_{\kappa_{p(t)}}^T}{2}. \tag{A.12}$$

For future use we will introduce the upper convected Oldroyd derivative of $\mathbf{B}_{\kappa_{p(t)}}$

through:

$$\overset{\nabla}{\mathbf{B}}_{\kappa_{p(t)}} := \dot{\mathbf{B}}_{\kappa_{p(t)}} - \text{Ł}\mathbf{B}_{\kappa_{p(t)}} - \mathbf{B}_{\kappa_{p(t)}}\text{Ł}^T = -2\mathbf{F}_{\kappa_{p(t)}}\mathbf{D}_{\kappa_{p(t)}}\mathbf{F}^T_{\kappa_{p(t)}}. \tag{A.13}$$

We shall define the density associated with the natural configuration $\kappa_{p(t)}$ through

$$\rho_{\kappa_{p(t)}} = \rho \text{III}_{\mathbf{F}_{\kappa_{p(t)}}} = \rho\sqrt{\text{III}_{\mathbf{B}_{\kappa_{p(t)}}}}. \tag{A.14}$$

We note that

$$\rho_{\kappa_r} = \rho_{\kappa_{p(t)}}\text{III}_{\mathbf{G}}. \tag{A.15}$$

1. Thermodynamics of Dissipative Materials

Now let us reconsider the reduced energy dissipation equation in the following form

$$\mathbf{T}.\text{Ł} - \rho\dot{\psi} - \rho\zeta\dot{\theta} - \frac{\text{q.grad}\theta}{\theta} = \rho\theta\Xi = \xi \geq 0. \tag{A.16}$$

Now, splitting the entropy production into two parts, that due to thermal effects and that due to mechanical dissipation and requiring both of them to be individually non-negative leads to:

$$\mathbf{T}.\text{Ł} - \rho\dot{\psi} = \hat{\xi} \geq 0. \tag{A.17}$$

B. Constitutive Model

In the current model temperature is assumed to be constant during laboratory compaction. For the general case the temperature effect can be accounted for by allowing the material parameters in the constitutive model to be different at different temperatures.

We thereafter assume the specific Helmholtz potential for the solid, ψ, is given as follows:

$$\psi = \frac{\mu(\text{III}_{\mathbf{G}})}{2\rho_{\kappa_{p(t)}}}\left(\text{I}_{\mathbf{B}_{\kappa_{p(t)}}} - 3 - \ln\left(\text{III}_{\mathbf{B}_{\kappa_{p(t)}}}\right)\right). \tag{B.1}$$

We specify the rate of dissipation due to the mechanical working ($\hat{\xi}$) to be:

$$\hat{\xi} = \eta(\mathrm{III}_{\mathbf{G}})\mathbf{D}_{\kappa_{p(t)}} \cdot \mathbf{B}_{\kappa_{p(t)}}\mathbf{D}_{\kappa_{p(t)}} \tag{B.2}$$

As the mixture is considered a single constituent, the 'shear modulus' like function, μ, can be thought of as a material property that reflects the characteristics of the aggregate matrix and the 'viscosity' function, η, reflects the characteristics of the asphalt mastic. Such a specification of the rate of dissipation corresponds to a material with a power-law type viscosity and is therefore used here to model the Non-Newtonian fluid like nature of the mix. Now, during compaction, the aggregate matrix which is initially in a loose form slowly evolves into a dense aggregate matrix. This densification is further aided by the changes in the asphalt mastic due to densification and reduction of mastic film thickness. The specific forms for the shear modulus and viscosity functions chosen ((B.3a), (B.3b)) represent such evolution.

To take into consideration the highly compressible behavior during the initial stages of compaction and the material hardening as the material reaches the limits of compressibility towards the end of the compaction process, we make the following choices for μ and η

$$\mu = \hat{\mu}(1 + \lambda_1(\mathrm{III}_{\mathbf{G}})^{2n_1})^{q_1} \tag{B.3a}$$

$$\eta = \hat{\eta}(1 + \lambda_2(\mathrm{III}_{\mathbf{G}})^{2n_2})^{q_2} \tag{B.3b}$$

1. Derivation of the Constitutive Expression for the Stress

We expand the total (material) time derivative of ψ using the chain rule of differentiation as follows:

$$\begin{aligned}\dot{\psi} &= \frac{\partial\psi}{\partial \mathrm{I}_{\mathbf{B}_{\kappa_{p(t)}}}}\dot{\mathrm{I}}_{\mathbf{B}_{\kappa_{p(t)}}} + \frac{\partial\psi}{\partial \mathrm{III}_{\mathbf{B}_{\kappa_{p(t)}}}}\dot{\mathrm{III}}_{\mathbf{B}_{\kappa_{p(t)}}} + \frac{\partial\psi}{\partial \mathrm{III}_{\mathbf{G}}}\dot{\mathrm{III}}_{\mathbf{G}} \\ &= 2\frac{\partial\psi}{\partial \mathrm{I}_{\mathbf{B}_{\kappa_{p(t)}}}}\mathbf{B}_{\kappa_{p(t)}}\cdot\left(\mathbf{D}-\mathbf{D}_{\kappa_{p(t)}}\right) + 2\frac{\partial\psi}{\partial \mathrm{III}_{\mathbf{B}_{\kappa_{p(t)}}}}\mathrm{III}_{\mathbf{B}_{\kappa_{p(t)}}}\,\mathbf{I}\cdot\left(\mathbf{D}-\mathbf{D}_{\kappa_{p(t)}}\right) \\ &\quad + \frac{\partial\psi}{\partial \mathrm{III}_{\mathbf{G}}}\mathrm{III}_{\mathbf{G}}\,\mathbf{I}\cdot\mathbf{D}_{\kappa_{p(t)}}\end{aligned} \tag{B.4}$$

Therefore, substituting the derivative $\dot{\psi}$ into the reduced form of the energy dissipation equation obtained as a consequence of the second law, we obtain

$$\begin{aligned}&\mathbf{T}.\mathbf{D} - \rho\Bigg[2\frac{\partial\psi}{\partial \mathrm{I}_{\mathbf{B}_{\kappa_{p(t)}}}}\left(\mathbf{B}_{\kappa_{p(t)}}\cdot\mathbf{D}-\mathbf{B}_{\kappa_{p(t)}}\cdot\mathbf{D}_{\kappa_{p(t)}}\right) \\ &+ 2\frac{\partial\psi}{\partial \mathrm{III}_{\mathbf{B}_{\kappa_{p(t)}}}}\mathrm{III}_{\mathbf{B}_{\kappa_{p(t)}}}\left(\mathbf{I}\cdot\mathbf{D}-\mathbf{I}\cdot\mathbf{D}_{\kappa_{p(t)}}\right) + \frac{\partial\psi}{\partial \mathrm{III}_{\mathbf{G}}}\mathrm{III}_{\mathbf{G}}\mathbf{I}\cdot\mathbf{D}_{\kappa_{p(t)}}\Bigg] = \hat{\xi}\geq 0\end{aligned} \tag{B.5}$$

where $\mathrm{I}_{\mathbf{B}_{\kappa_{p(t)}}}$ and $\mathrm{III}_{\mathbf{B}_{\kappa_{p(t)}}}$ are the first and third invariants of $\mathbf{B}_{\kappa_{p(t)}}$ and also $\mathrm{III}_{\mathbf{G}}$ is the third invariant of the tensor $\mathbf{G}$. Rearranging the equations we get

$$\begin{aligned}&\left[\mathbf{T} - 2\rho\frac{\partial\psi}{\partial \mathrm{I}_{\mathbf{B}_{\kappa_{p(t)}}}}\mathbf{B}_{\kappa_{p(t)}} - 2\rho\mathrm{III}_{\mathbf{B}_{\kappa_{p(t)}}}\frac{\partial\psi}{\partial \mathrm{III}_{\mathbf{B}_{\kappa_{p(t)}}}}\mathbf{I}\right]\cdot\mathbf{D} + \left[2\rho\frac{\partial\psi}{\partial \mathrm{I}_{\mathbf{B}_{\kappa_{p(t)}}}}\mathbf{B}_{\kappa_{p(t)}}\right. \\ &\left. + 2\rho\mathrm{III}_{\mathbf{B}_{\kappa_{p(t)}}}\frac{\partial\psi}{\partial \mathrm{III}_{\mathbf{B}_{\kappa_{p(t)}}}}\mathbf{I} - \rho\mathrm{III}_{\mathbf{G}}\frac{\partial\psi}{\partial \mathrm{III}_{\mathbf{G}}}\mathbf{I}\right]\cdot\mathbf{D}_{\kappa_{p(t)}} = \hat{\xi}\geq 0.\end{aligned} \tag{B.6}$$

Now considering the form chosen for the rate of dissipation function, we shall assume that

$$\begin{aligned}\mathbf{T} &= \underbrace{2\rho\mathrm{III}_{\mathbf{B}_{\kappa_{p(t)}}}\frac{\partial\psi}{\partial \mathrm{III}_{\mathbf{B}_{\kappa_{p(t)}}}}}_{\alpha_1}\mathbf{I} + \underbrace{2\rho\frac{\partial\psi}{\partial \mathrm{I}_{\mathbf{B}_{\kappa_{p(t)}}}}}_{\alpha_2}\mathbf{B}_{\kappa_{p(t)}} \\ &= \alpha_1\mathbf{I} + \alpha_2\mathbf{B}_{\kappa_{p(t)}}\end{aligned} \tag{B.7}$$

thereby reducing the constraint posed by the second law to the following form

$$\left(\mathbf{T} - \underbrace{\rho \mathrm{III}_{\mathbf{G}} \frac{\partial \psi}{\partial \mathrm{III}_{\mathbf{G}}}}_{k} \mathbf{I}\right) \cdot \mathbf{D}_{\kappa_{p(t)}} = \hat{\xi} \tag{B.8}$$

2. Maximization of the Rate of Dissipation

Applying the standard method of constrained maximization with Lagrange multiplier λ to maximize the rate of dissipation $\hat{\xi}$ with the constraint imposed by the second law (A.17), we have

$$h = \hat{\xi} + \lambda \left[(\mathbf{T} - k\mathbf{I}) \cdot \mathbf{D}_{\kappa_{p(t)}} - \hat{\xi} \right] \tag{B.9}$$

where,

$$k := \rho \, \mathrm{III}_{\mathbf{G}} \frac{\partial \psi}{\partial \mathrm{III}_{\mathbf{G}}} \tag{B.10}$$

Also remembering that the material is isotropic, we can choose (without any loss in generality) that the configuration $\kappa_{p(t)}$ is rotated such that

$$\mathbf{F}_{\kappa_{p(t)}} = \mathbf{V}_{\kappa_{p(t)}} \tag{B.11}$$

Now differentiating h with $\mathbf{D}_{\kappa_{p(t)}}$ using the chosen form for $\hat{\xi}$ (B.2) and then equating it to zero, we have

$$\begin{aligned}
&\frac{\partial h}{\partial \mathbf{D}_{\kappa_{p(t)}}} = \frac{\partial \hat{\xi}}{\partial \mathbf{D}_{\kappa_{p(t)}}} + \lambda \left[(\mathbf{T} - k\mathbf{I}) - \frac{\partial \hat{\xi}}{\partial \mathbf{D}_{\kappa_{p(t)}}} \right] = 0 \\
\Rightarrow &\left(\frac{\lambda - 1}{\lambda} \right) \frac{\partial \hat{\xi}}{\partial \mathbf{D}_{\kappa_{p(t)}}} - (\mathbf{T} - k\mathbf{I}) = 0 \\
\Rightarrow &\left(\frac{\lambda - 1}{\lambda} \right) 2\eta \mathbf{B}_{\kappa_{p(t)}} \mathbf{D}_{\kappa_{p(t)}} = \mathbf{T} - k\mathbf{I} \qquad \text{(B.12)} \\
\Rightarrow &2 \left(\frac{\lambda - 1}{\lambda} \right) \mathbf{D}_{\kappa_{p(t)}} \cdot \mathbf{B}_{\kappa_{p(t)}} \mathbf{D}_{\kappa_{p(t)}} = (\mathbf{T} - k\mathbf{I}) \cdot \mathbf{D}_{\kappa_{p(t)}} \\
\Rightarrow &2 \left(\frac{\lambda - 1}{\lambda} \right) \hat{\xi} = (\mathbf{T} - k\mathbf{I}) \cdot \mathbf{D}_{\kappa_{p(t)}} = \hat{\xi}, \text{ from constitutive assumption (B.2)} \\
\Rightarrow &\left(\frac{\lambda - 1}{\lambda} \right) = \frac{1}{2} \\
\Rightarrow &\lambda = 2
\end{aligned}$$

Therefore, by substituting for λ in (B.12) we have

$$\mathbf{T} - k\mathbf{I} = \eta \mathbf{B}_{\kappa_{p(t)}} \mathbf{D}_{\kappa_{p(t)}} \qquad \text{(B.13)}$$

Now, pre-multiplying with $\mathbf{V}^{-1}_{\kappa_{p(t)}}$ and post-multiplying with $\mathbf{V}_{\kappa_{p(t)}}$ we obtain

$$\mathbf{V}^{-1}_{\kappa_{p(t)}} (\mathbf{T} - k\mathbf{I}) \mathbf{V}_{\kappa_{p(t)}} = \eta \mathbf{V}_{\kappa_{p(t)}} \mathbf{D}_{\kappa_{p(t)}} \mathbf{V}_{\kappa_{p(t)}} \qquad \text{(B.14)}$$

3. Evolution Equation for $\mathbf{B}_{\kappa_{p(t)}}$

Thereafter, recalling (A.13) and (B.11), we obtain the evolution equation for $\mathbf{B}_{\kappa_{p(t)}}$ in the following form,

$$\begin{aligned}
\overset{\nabla}{\mathbf{B}}_{\kappa_{p(t)}} &= -\frac{2}{\eta} \left(\mathbf{V}^{-1}_{\kappa_{p(t)}} \mathbf{T} \mathbf{V}_{\kappa_{p(t)}} - k\mathbf{I} \right) \\
&= -\frac{2}{\eta} \left[(\alpha_1 - k)\mathbf{I} + \alpha_2 \mathbf{B}_{\kappa_{p(t)}} \right] \qquad \text{(B.15)}
\end{aligned}$$

Now substituting (B.7) in (B.13) and then pre multiplying with $\mathbf{B}_{\kappa_{p(t)}}^{-1}$ and then taking trace of the resulting equation we obtain:

$$(\alpha_1 - k)\mathbf{I} + \alpha_2 \mathbf{B}_{\kappa_{p(t)}} = \eta \mathbf{B}_{\kappa_{p(t)}} \mathbf{D}_{\kappa_{p(t)}} \tag{B.16}$$

$$(\alpha_1 - k)\mathbf{B}_{\kappa_{p(t)}}^{-1} + \alpha_2 \mathbf{I} = \eta \mathbf{D}_{\kappa_{p(t)}}$$

$$\Rightarrow \text{tr}\left(\mathbf{D}_{\kappa_{p(t)}}\right) = \frac{(\alpha_1 - k)\text{tr}\left(\mathbf{B}_{\kappa_{p(t)}}^{-1}\right) + 3\alpha_2}{\eta} \tag{B.17}$$

Consider (B.16) and take its trace to get

$$\text{tr}\left(\mathbf{B}_{\kappa_{p(t)}} \mathbf{D}_{\kappa_{p(t)}}\right) = \frac{3(\alpha_1 - k) + \alpha_2 \text{tr}\left(\mathbf{B}_{\kappa_{p(t)}}\right)}{\eta} \tag{B.18}$$

Now substituting (B.17) and (B.18) in (B.8) we obtain the constraint expression for all the permissible $\mathbf{D}_{\kappa_{p(t)}}$ as:

$$\left((\alpha_1 - k)\mathbf{I} + \alpha_2 \mathbf{B}_{\kappa_{p(t)}}\right) \cdot \mathbf{D}_{\kappa_{p(t)}} = \hat{\xi} = \eta \mathbf{D}_{\kappa_{p(t)}} \cdot \mathbf{B}_{\kappa_{p(t)}} \mathbf{D}_{\kappa_{p(t)}}$$

$$(\alpha_1 - k)\text{tr}\left(\mathbf{D}_{\kappa_{p(t)}}\right) + \alpha_2 \text{tr}\left(\mathbf{B}_{\kappa_{p(t)}} \mathbf{D}_{\kappa_{p(t)}}\right) = \eta \mathbf{D}_{\kappa_{p(t)}} \cdot \mathbf{B}_{\kappa_{p(t)}} \mathbf{D}_{\kappa_{p(t)}}$$

$$\Rightarrow \frac{(\alpha_1 - k)\left[(\alpha_1 - k)\text{tr}\left(\mathbf{B}_{\kappa_{p(t)}}^{-1}\right) + 3\alpha_2\right] + \alpha_2\left[3(\alpha_1 - k) + \alpha_2 \text{tr}\left(\mathbf{B}_{\kappa_{p(t)}}\right)\right]}{\eta}$$

$$= \eta \mathbf{D}_{\kappa_{p(t)}} \cdot \mathbf{B}_{\kappa_{p(t)}} \mathbf{D}_{\kappa_{p(t)}}$$

$$\Rightarrow \mathbf{D}_{\kappa_{p(t)}} \cdot \mathbf{B}_{\kappa_{p(t)}} \mathbf{D}_{\kappa_{p(t)}} =$$

$$\underbrace{\frac{1}{\eta^2}\left[(\alpha_1 - k)\left((\alpha_1 - k)\text{tr}\left(\mathbf{B}_{\kappa_{p(t)}}^{-1}\right) + 6\alpha_2\right) + \alpha_2^2 \text{tr}\left(\mathbf{B}_{\kappa_{p(t)}}\right)\right]}_{\delta}$$

$$\Rightarrow \mathbf{D}_{\kappa_{p(t)}} \cdot \mathbf{B}_{\kappa_{p(t)}} \mathbf{D}_{\kappa_{p(t)}} = \delta \tag{B.19}$$

where the implicit functions δ, α_1 and α_2 are given by the following equations,

$$\delta = \left[\frac{1}{\eta^2}\left\{(\alpha_1 - k)\left((\alpha_1 - k)\mathrm{I}_{\mathbf{B}^{-1}_{\kappa_{p(t)}}} + 6\alpha_2\right) + \alpha_2^2 \mathrm{I}_{\mathbf{B}_{\kappa_{p(t)}}}\right\}\right] \tag{B.20a}$$

$$\alpha_1 = 2\rho \mathrm{III}_{\mathbf{B}_{\kappa_{p(t)}}} \frac{\partial \psi}{\partial \mathrm{III}_{\mathbf{B}_{\kappa_{p(t)}}}} \tag{B.20b}$$

$$\alpha_2 = 2\rho \frac{\partial \psi}{\partial \mathrm{I}_{\mathbf{B}_{\kappa_{p(t)}}}} \tag{B.20c}$$

$$k = \rho \mathrm{III}_{\mathbf{G}} \frac{\partial \psi}{\partial \mathrm{III}_{\mathbf{G}}} \tag{B.20d}$$

$$\left.\frac{\partial \psi}{\partial \mathrm{III}_{\mathbf{G}}}\right|_{\mathrm{III}_{\mathbf{B}_{\kappa_{p(t)}}} \text{ fixed}} = \frac{\mathrm{I}_{\mathbf{B}_{\kappa_{p(t)}}} - 3 - \ln\left(\mathrm{III}_{\mathbf{B}_{\kappa_{p(t)}}}\right)}{2\rho\sqrt{\mathrm{III}_{\mathbf{B}_{\kappa_{p(t)}}}}} \left(\frac{\partial \mu}{\partial \mathrm{III}_{\mathbf{G}}} + \frac{\mu}{\mathrm{III}_{\mathbf{G}}}\right) \tag{B.20e}$$

$$\left.\frac{\partial \mu}{\partial \mathrm{III}_{\mathbf{G}}}\right|_{\mathrm{III}_{\mathbf{B}_{\kappa_{p(t)}}} \text{ fixed}} = 2\lambda_1 n_1 q_1 \hat{\mu} {\mathrm{III}_{\mathbf{G}}}^{(2n_1-1)} (1 + \lambda_1 {\mathrm{III}_{\mathbf{G}}}^{2n_1})^{(q_1-1)} \tag{B.20f}$$

$$\left.\frac{\partial \psi}{\partial \mathrm{III}_{\mathbf{B}_{\kappa_{p(t)}}}}\right|_{\mathrm{III}_{\mathbf{G}} \text{ fixed}} = -\frac{\mu}{4\rho {\mathrm{III}_{\mathbf{B}_{\kappa_{p(t)}}}}^{3/2}} \left[\mathrm{I}_{\mathbf{B}_{\kappa_{p(t)}}} - 1 - \ln\left(\mathrm{III}_{\mathbf{B}_{\kappa_{p(t)}}}\right)\right] \tag{B.20g}$$

$$\frac{\partial \psi}{\partial \mathrm{I}_{\mathbf{B}_{\kappa_{p(t)}}}} = \frac{\mu}{2\rho\sqrt{\mathrm{III}_{\mathbf{B}_{\kappa_{p(t)}}}}} \tag{B.20h}$$

α_1, α_2 and k carry the same dimensions as $\hat{\mu}$; and η has the same dimensions as $\hat{\mu}$, hence we use the following non-dimensionalizations to rewrite (B.15):

$$\bar{\alpha}_1 = \frac{\alpha_1}{\hat{\mu}};\ \bar{\alpha}_2 = \frac{\alpha_2}{\hat{\mu}};\ \bar{k} = \frac{k}{\hat{\mu}};\ \bar{\eta} = \frac{\eta}{\hat{\eta}} \tag{B.21}$$

We also define an initial relaxation time for the evolution equation and a non-dimensional form for time t as follows:

$$\tau = \frac{\hat{\eta}}{2\hat{\mu}};\ \bar{t} = \frac{t}{\tau} \tag{B.22}$$

Thereafter, we can write the evolution equation (B.15), as

$$\begin{aligned}\overset{\nabla}{\mathbf{B}}_{\kappa_{p(t)}} &= -\frac{2\hat{\mu}}{\bar{\eta}\hat{\eta}}\left[(\bar{\alpha}_1-\bar{k})\mathbf{I}+\bar{\alpha}_2\mathbf{B}_{\kappa_{p(t)}}\right]\\ &= -\frac{1}{\tau\bar{\eta}}\left[(\bar{\alpha}_1-\bar{k})\mathbf{I}+\bar{\alpha}_2\mathbf{B}_{\kappa_{p(t)}}\right]\end{aligned} \tag{B.23}$$

Now we can define a convected derivative with respect to the time parameter $\bar{t}$, denoting it $(\overset{\nabla'}{\cdot})$, as

$$\begin{aligned}(\overset{\nabla}{\cdot}) &= (\overset{\nabla'}{\cdot})(\overset{\nabla}{\bar{t}})\\ &= (\overset{\nabla'}{\cdot})\frac{\partial\bar{t}}{\partial t} = \frac{1}{\tau}(\overset{\nabla'}{\cdot})\end{aligned} \tag{B.24}$$

Now using the definition of the convected derivative with respect to a new non-dimensional time parameter (B.24), we can write the evolution equation (B.23) in a completely non-dimensional form as:

$$\begin{aligned}\overset{\nabla}{\mathbf{B}}_{\kappa_{p(t)}} = \frac{1}{\tau}\overset{\nabla'}{\mathbf{B}}_{\kappa_{p(t)}} &= -\frac{1}{\tau\bar{\eta}}\left[(\bar{\alpha}_1-\bar{k})\mathbf{I}+\bar{\alpha}_2\mathbf{B}_{\kappa_{p(t)}}\right]\\ \overset{\nabla'}{\mathbf{B}}_{\kappa_{p(t)}} &= -\frac{1}{\bar{\eta}}\left[(\bar{\alpha}_1-\bar{k})\mathbf{I}+\bar{\alpha}_2\mathbf{B}_{\kappa_{p(t)}}\right]\end{aligned} \tag{B.25}$$

C. Analytical Calculations Using a Semi-inverse Approach

For validation of the model we need to consider the 3D compressive deformation with an applied dead load and dynamic boundary conditions such as present in the SGC, as the SGC experiments provide the only qualitative data regarding mechanical behavior of the material. However to do this we need to implement the model in a F.E methodology that will enable us to model the 3D behavior in general. As such we choose to study the developed model through analytical calculations aided in part by the computations. Presented in this section is the formulation for such a study and the calculations done using the mathematical equation solving software, MATLAB [55].

We develop the governing equations of motion for the constrained 1D compression of the material model using a semi-inverse approach by prescribing the necessary deformation field for this case. The model's response to constant stress and constant strain is then illustrated before we provide an F.E implementation formulation/scheme in Chapter IV.

1. Kinematics of One-dimensional Constrained Compression

We, therefore, shall assume the following form for the deformation in cylindrical coordinates:

$$r(t) = R\ ,\ \theta(t) = \Theta\ ,\ z(t) = \Lambda(t)Z \tag{C.1}$$

where $\Lambda(t)$ represents the stretch in the direction of loading, as a function of time. The deformation gradient referred to the reference configuration is therefore given by

$$[\mathbf{F}_{\kappa_r}] = \text{diag}\{1, 1, \Lambda(t)\} \tag{C.2a}$$

$$[\mathbf{L}_{\kappa_r}] = \text{diag}\left\{0, 0, \frac{\dot{\Lambda}(t)}{\Lambda(t)}\right\} = [\mathbf{D}_{\kappa_r}] \tag{C.2b}$$

$$[\mathbf{B}_{\kappa_r}] = \text{diag}\{1, 1, \Lambda^2(t)\} = [\mathbf{C}_{\kappa_r}] \tag{C.2c}$$

The strain measures with respect to the reference configuration, the current configuration and their total time derivatives are given as follows:

$$[\mathbf{E}] = \frac{[\mathbf{C}_{\kappa_r} - \mathbf{I}]}{2} = \text{diag}\left\{0, 0, \frac{1}{2}(\Lambda^2(t) - 1)\right\} \tag{C.3a}$$

$$[\mathbf{e}] = \frac{[\mathbf{I} - \mathbf{B}_{\kappa_r}^{-1}]}{2} = \text{diag}\left\{0, 0, \frac{1}{2}\left(1 - \frac{1}{\Lambda^2(t)}\right)\right\} \tag{C.3b}$$

$$[\dot{\mathbf{E}}] = \mathbf{F}_{\kappa_r}^T \mathbf{D}_{\kappa_r} \mathbf{F}_{\kappa_r} = \text{diag}\{0, 0, \Lambda(t)\dot{\Lambda}(t)\} \tag{C.4a}$$

$$[\dot{\mathbf{e}}] = \mathbf{D}_{\kappa_r} - (\mathbf{e}\mathbf{L}_{\kappa_r} + \mathbf{L}_{\kappa_r}^T \mathbf{e}) = \text{diag}\left\{0, 0, \frac{\dot{\Lambda}(t)}{\Lambda^3(t)}\right\} \tag{C.4b}$$

The response from the natural configuration and the evolution of the natural configuration that are consistent with the above prescribed motion are given by

$$[\mathbf{F}_{\kappa_{p(t)}}] = \text{diag}\{1, 1, b(t)\}, \quad \text{and} \tag{C.5}$$

$$[\mathbf{G}] = \text{diag}\{1, 1, g(t)\} \tag{C.6}$$

Therefore, we have the velocity gradient and the left stretch tensor with respect to the evolving natural configurations as

$$[\mathbf{L}_{\kappa_{p(t)}}] = \text{diag}\left\{0, 0, \frac{\dot{g}(t)}{g(t)}\right\} = [\mathbf{D}_{\kappa_{p(t)}}] \tag{C.7}$$

$$[\mathbf{B}_{\kappa_{p(t)}}] = \text{diag}\{1, 1, b^2(t)\} \tag{C.8}$$

Now, from the following relationship

$$\mathbf{F}_{\kappa_r} = \mathbf{F}_{\kappa_{p(t)}} \mathbf{G} \tag{C.9}$$

we have,

$$\Lambda(t) = b(t) \cdot g(t) \tag{C.10}$$

a. Thermodynamic Quantities for a One-dimensional Deformation Field

The specific Helmholtz potential is calculated as:

$$\psi(t) = \frac{\mu[b^2(t) - 1 - 2\ln(b(t))]}{2\rho b(t)} \tag{C.11}$$

and the total rate of dissipation is accounted to be

$$\hat{\xi}(t) = \eta \left(\dot{g}(t) \frac{b(t)}{g(t)} \right)^2 \tag{C.12}$$

2. One-dimensional Creep Deformation

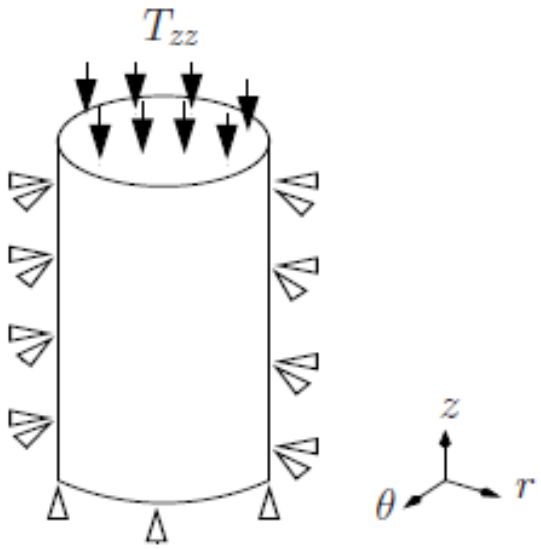

Fig. 2.: Schematic for the one-dimensional compression problem

Now, since the deformation is prescribed in the forms given by (C.2a), (C.5) and (C.6), we can not prescribe a specific lateral stress condition. Such a constraint on the choice of stress will render the system over-constrained and hence no unique solution exists. We therefore choose the diagonal components of stress as unknowns except for the prescribed creep load. Hence, we apply a constant compressive stress along the axial z-direction (Figure 2), therefore we have

$$[\mathbf{T}] = \text{diag}\{T_{rr}, T_{\theta\theta}, T_{zz}\} \tag{C.13}$$

a. Model Equations Corresponding to One-dimensional Deformation

Therefore, we have the material functions in the following form:

$$\mu(g) = \hat{\mu}(1 + \lambda_1(g(t))^{2n_1})^{q_1} \tag{C.14a}$$

$$\eta(g) = \hat{\eta}(1 + \lambda_2(g(t))^{2n_2})^{q_2} \tag{C.14b}$$

The constitutive equation for the stress in the z-direction gives us the following condition for $b(t)$

$$T_{zz} = \alpha_1 \, + \, \alpha_2 b^2(t) \tag{C.15}$$

where, using the general definitions (B.20b) and (B.20c) we can write

$$\alpha_1 = -\frac{\mu}{2b(t)}[b^2(t) + 1 - 2\ln(b(t))] \tag{C.16a}$$

$$\alpha_2 = \frac{\mu}{b(t)} \tag{C.16b}$$

The evolution equation in the direction of applied load is obtained using (B.15), as

$$\frac{\partial B_{zz}}{\partial t} + v_z \frac{\partial B_{zz}}{\partial z} - 2L_{zz}B_{zz} = C_1 \, + \, C_2 \, B_{zz} \tag{C.17a}$$

$$2b(t)\dot{b}(t) - 2\frac{\dot{\Lambda}(t)}{\Lambda(t)}b^2(t) = C_1 + C_2 b^2(t) \tag{C.17b}$$

where,

$$C_1 = -\frac{2(\alpha_1 - k)}{\eta} \tag{C.18a}$$

$$C_2 = -\frac{2\alpha_2}{\eta} \tag{C.18b}$$

By utilizing the definitions in the expressions (B.20d), (B.20e) and (A.15) we obtain

$$\frac{\partial \mu}{\partial \mathrm{III}_{\mathbf{G}}} = \frac{\partial \mu}{\partial g(t)} = 2\lambda_1 n_1 q_1 \hat{\mu} g(t)^{(2n_1-1)}(1 + \lambda_1 g(t)^{2n_1})^{(q_1-1)} \tag{C.19a}$$

$$k = \frac{(b^2(t) - 1 - 2\ln b(t))}{2b(t)} \left(g(t)\frac{\partial \mu}{\partial g(t)} + \mu \right) \tag{C.19b}$$

Now, consider (C.10), and take its derivative with respect to time to get

$$\frac{\dot{\Lambda}(t)}{\Lambda(t)} = \frac{\dot{b}(t)}{b(t)} + \frac{\dot{g}(t)}{g(t)} \tag{C.20}$$

Thereafter, on further simplification using (C.20) in (C.17b) we obtain the following:

$$\dot{g}(t) = -\frac{g(t)}{2}\left(\frac{C_1}{b^2(t)} + C_2\right) \tag{C.21}$$

which is to be solved in conjunction with the constraint equation due to applied stress given (using C.15) by

$$\begin{aligned} T_{zz} &= -\frac{\mu}{2b(t)}[b^2(t) + 1 - 2\ln(b(t))] + \mu b(t) \\ &= \mu\left[b(t) - \frac{1}{2}\left\{b(t) + \frac{1}{b(t)} - 2\frac{\ln(b(t))}{b(t)}\right\}\right] \end{aligned} \tag{C.22}$$

subject to the initial condition for $g(t)$ given by

$$g(0) = 1 \tag{C.23}$$

We can, thereafter, calculate the radial and angular components of the stress from the following expression after making use of (C.16):

$$T_{rr} = T_{\theta\theta} = \alpha_1 + \alpha_2 \tag{C.24}$$

b. Dimensionless Form of the Model Equations for the One-dimensional Deformation

Now recalling the non-dimensionalizations defined in (B.21) and (B.22), we rewrite the equations describing the 1D constrained compression. We begin by expressing the kinematical quantities such as the stretches and the total velocity gradient (C.2b)

in non-dimensional form as follows:

$$b(t) = b(\bar{t}\tau) = \tilde{b}(\bar{t});\ g(t) = g(\bar{t}\tau) = \tilde{g}(\bar{t}); \tag{C.25a}$$

$$\Lambda(t) = \Lambda(\bar{t}\tau) = \tilde{\Lambda}(\bar{t});\ L(t) = L(\bar{t}\tau) = \tilde{L}(\bar{t}); \tag{C.25b}$$

$$\begin{aligned}\bar{L}(\bar{t}) &= \tau L(\bar{t}) = \tau L(t) \\ &= \text{diag}\left\{0, 0, \tau\frac{\dot{\Lambda}(t)}{\Lambda(t)}\right\} = \text{diag}\left\{0, 0, \frac{\left(\tilde{\Lambda}\right)'(\bar{t})}{\tilde{\Lambda}(\bar{t})}\right\}\end{aligned} \tag{C.25c}$$

$$T_{zz}(t) = T_{zz}(\bar{t}\tau) = \tilde{T}_{zz}(\bar{t}) \tag{C.25d}$$

where, $(.)'$ denotes partial derivative with respect to the independent argument of the function (i.e $\bar{t}$ here). For simplicity we can think of $\tilde{(.)}$ as denoting a time normalization and $\bar{(.)}$ referring to normalization with respect to a context-relevant physical quantity. Henceforth, for the sake of convenience we shall not explicitly write down

the arguments.

$$\tau = \frac{\hat{\eta}}{2\hat{\mu}} \tag{C.26a}$$

$$\tilde{\mu} = \mu(\tilde{g}) = \hat{\mu}(1 + \lambda_1 (\tilde{g})^{2n_1})^{q_1} \tag{C.26b}$$

$$\tilde{\eta} = \eta(\tilde{g}) = \hat{\eta}(1 + \lambda_2 (\tilde{g})^{2n_2})^{q_2} \tag{C.26c}$$

$$\tilde{\alpha}_1 = -\frac{\tilde{\mu}}{2\tilde{b}}[\tilde{b}^2 + 1 - 2\ln(\tilde{b})] \tag{C.26d}$$

$$\tilde{\alpha}_2 = \frac{\tilde{\mu}}{\tilde{b}} \tag{C.26e}$$

$$\frac{\partial \mu}{\partial g} = \frac{\partial \tilde{\mu}}{\partial g} = \frac{\partial \tilde{\mu}}{\partial \tilde{g}} = 2\lambda_1 n_1 q_1 \hat{\mu} \tilde{g}^{(2n_1-1)}(1 + \lambda_1 \tilde{g}^{2n_1})^{(q_1-1)} \tag{C.26f}$$

$$\begin{aligned}\frac{\partial^2 \mu}{\partial g^2} =& \frac{\partial^2 \tilde{\mu}}{\partial g^2} = \frac{\partial^2 \tilde{\mu}}{\partial \tilde{g}^2} \\ =& 2\lambda_1 n_1 q_1 \hat{\mu} \tilde{g}^{(2n_1-2)}(1 + \lambda_1 \tilde{g}^{2n_1})^{(q_1-2)} \\ & [2n_1 - 1 + \lambda_1 \tilde{g}^{(2n_1-1)}(2n_1 q_1 + (2n_1 - 1)\tilde{g})]\end{aligned} \tag{C.26g}$$

$$\frac{\partial \eta}{\partial g} = \frac{\partial \tilde{\eta}}{\partial g} = \frac{\partial \tilde{\eta}}{\partial \tilde{g}} = 2\lambda_2 n_2 q_2 \hat{\eta} \tilde{g}^{(2n_2-1)}(1 + \lambda_2 \tilde{g}^{2n_2})^{(q_2-1)} \tag{C.26h}$$

$$\tilde{k} = \frac{\tilde{b}^2 - 1 - 2\ln(\tilde{b})}{2\tilde{b}} \left(\tilde{g} \frac{\partial \tilde{\mu}}{\partial \tilde{g}} + \tilde{\mu} \right) \tag{C.26i}$$

$$\tilde{C}_1 = -\frac{2(\tilde{\alpha}_1 - \tilde{k})}{\tilde{\eta}} \tag{C.27a}$$

$$\tilde{C}_2 = -\frac{2\tilde{\alpha}_2}{\tilde{\eta}} \tag{C.27b}$$

Now, the relation between the two different types of time derivatives is obtained as:

$$\begin{aligned}\dot{g}(t) &= (\tilde{g}(\bar{t}))' (\dot{\bar{t}}) \\ &= \frac{1}{\tau} (\tilde{g}(\bar{t}))'\end{aligned} \tag{C.28}$$

We, thereafter, reformulate the evolution equation (C.21), making use of (C.28) and can solve it for $\tilde{g}$ subject to the constraint we obtain by making use of (C.25a)

in (C.22).

$$\tilde{g}' = -\frac{\tau\tilde{g}}{2}\left(\frac{\tilde{C}_1}{\tilde{b}^2} + \tilde{C}_2\right) \tag{C.29}$$

$$\begin{aligned}\tilde{T}_{zz} &= -\frac{\tilde{\mu}}{2\tilde{b}}[\tilde{b}^2 + 1 - 2\ln(\tilde{b})] + \tilde{\mu}\tilde{b} \\ &= \tilde{\mu}\left[\tilde{b} - \frac{1}{2}\left\{\tilde{b} + \frac{1}{\tilde{b}} - 2\frac{\ln(\tilde{b})}{\tilde{b}}\right\}\right]\end{aligned} \tag{C.30}$$

However, we choose to make the parametric functions $\tilde{\mu}$, $\tilde{C}_1$, $\tilde{C}_2$ and $\tilde{T}_{zz}$ dimensionless, similar to what was done earlier for the generalized evolution equation (B.23). Considering that the specific application here is a 1D constraint creep, we can normalize the axial stress $\tilde{T}_{zz}$ and other similar dimensional quantities using the initial applied creep load $\tilde{T}_{zz}(0)$. This is done using the following dimensionless quantities:

$$\bar{\tilde{\mu}} = \frac{\tilde{\mu}}{\tilde{T}_{zz}(0)} \tag{C.31a}$$

$$\bar{\tilde{\alpha}}_1 = \frac{\tilde{\alpha}_1}{\tilde{T}_{zz}(0)} \tag{C.31b}$$

$$\bar{\tilde{\alpha}}_2 = \frac{\tilde{\alpha}_2}{\tilde{T}_{zz}(0)} \tag{C.31c}$$

$$\bar{\tilde{C}}_1 = \tau\tilde{C}_1 \tag{C.31d}$$

$$\bar{\tilde{C}}_2 = \tau\tilde{C}_2 \tag{C.31e}$$

$$\begin{aligned}\bar{\tilde{T}}_{zz} &= \frac{\tilde{T}_{zz}}{\tilde{T}_{zz}(0)} \\ &= \frac{\bar{\tilde{\mu}}}{2}\left(\tilde{b} - \frac{1}{\tilde{b}} + 2\frac{\ln(\tilde{b})}{\tilde{b}}\right)\end{aligned} \tag{C.31f}$$

and thereafter using (C.31), the differential equation (C.29) can be written as

$$\tilde{g}' = -\frac{\tilde{g}}{2}\left(\frac{\bar{\tilde{C}}_1}{\tilde{b}^2} + \bar{\tilde{C}}_2\right) \tag{C.32}$$

which can be solved for $\tilde{g}(\bar{t})$ subject to the constraint (C.31f) and the following initial conditions,

$$\begin{aligned}
&\tilde{g}(0) = 1, \text{ with } \tilde{b}(0) \text{ calculated from the following algebraic equation:} \\
&\tilde{b}(0) - \frac{1}{2}\left\{\tilde{b}(0) + \frac{1}{\tilde{b}(0)} - 2\frac{\ln(\tilde{b}(0))}{\tilde{b}(0)}\right\} = \frac{\tilde{T}_{zz}}{\hat{\mu}}(1+\lambda_1)^{-q_1} \\
&\Rightarrow \tilde{b}^2(0) - 2\frac{\tilde{T}_{zz}}{\hat{\mu}}(1+\lambda_1)^{-q_1}\tilde{b}(0) + 2\ln(\tilde{b}(0)) - 1 = 0
\end{aligned} \tag{C.33}$$

We then calculate the non-dimensional radial and angular components of the stress from the following expression:

$$\bar{\tilde{T}}_{rr} = \bar{\tilde{T}}_{\theta\theta} = \bar{\tilde{\alpha}}_1 + \bar{\tilde{\alpha}}_2 \tag{C.34}$$

c. Solution of the System of Nonlinear Equations Using $MATLAB$

The system of equations to be solved can be written in a matrix format suited for implementing in MATLAB [55]. Let y represent the vector of solutions variables $\tilde{g}$ and $\tilde{b}$, then we have

$$y = \begin{pmatrix} \tilde{g} \\ \tilde{b} \end{pmatrix}; \quad f = \begin{pmatrix} f_1 \\ f_2 \end{pmatrix} \tag{C.35}$$

Thereafter we rewrite the equations to be solved simultaneously as a system of implicit differential-algebraic equations:

$$\begin{aligned}
&M(\bar{t}, y)y(\bar{t}) = f(\bar{t}, y) \\
&\begin{bmatrix} \tilde{b}^2 & 0 \\ 0 & \varepsilon\tilde{b} \end{bmatrix} \begin{pmatrix} \tilde{g} \\ \tilde{b} \end{pmatrix} = \begin{pmatrix} -0.5\tilde{g}(\bar{\tilde{C}}_1 + \tilde{b}^2\bar{\tilde{C}}_2) \\ \tilde{b}\bar{\tilde{T}}_{zz} - 0.5\bar{\tilde{\mu}}(\tilde{b}^2 - 1 + 2\ln\tilde{b}) \end{pmatrix}
\end{aligned} \tag{C.36}$$

Where ε is a very small multiplicative constant and M is called the mass matrix for the system. Further, the jacobian of iteration for this system is then given by

$$J := \left[\frac{\partial f}{\partial y}\right] = \begin{bmatrix} \dfrac{\partial f_1}{\partial \tilde{g}} & \dfrac{\partial f_1}{\partial \tilde{b}} \\ \\ \dfrac{\partial f_2}{\partial \tilde{g}} & \dfrac{\partial f_2}{\partial \tilde{b}} \end{bmatrix} \tag{C.37}$$

$$\frac{\partial f_1}{\partial \tilde{g}} = -0.5(\bar{\tilde{C}}_1 + \tilde{b}^2 \bar{\tilde{C}}_2) - 0.5\tilde{g}\left(\frac{\partial \bar{\tilde{C}}_1}{\partial \tilde{g}} + \tilde{b}^2 \frac{\partial \bar{\tilde{C}}_2}{\partial \tilde{g}}\right) \tag{C.38a}$$

$$\frac{\partial f_1}{\partial \tilde{b}} = -0.5\tilde{g}\left(\frac{\partial \bar{\tilde{C}}_1}{\partial \tilde{b}} + 2\tilde{b}\bar{\tilde{C}}_2 + \tilde{b}^2 \frac{\partial \bar{\tilde{C}}_2}{\partial \tilde{b}}\right) \tag{C.38b}$$

$$\frac{\partial f_2}{\partial \tilde{g}} = -0.5\left(\frac{\tilde{b}^2 - 1 + 2\ln \tilde{b}}{T_{zz}(0)}\right)\frac{\partial \tilde{\mu}}{\partial \tilde{g}} \tag{C.38c}$$

$$\frac{\partial f_2}{\partial \tilde{b}} = \bar{\tilde{T}}_{zz} - \bar{\tilde{\mu}}\left(\tilde{b} + \frac{1}{\bar{\tilde{b}}}\right) \tag{C.38d}$$

where,

$$\frac{\partial \bar{\tilde{C}}_1}{\partial \tilde{g}} = \tau \frac{\partial \tilde{C}_1}{\partial \tilde{g}} = -\frac{\tau}{\tilde{\eta}}\left[-\frac{(\tilde{\alpha}_1 - \tilde{k})}{\tilde{\eta}}\frac{\partial \tilde{\eta}}{\partial \tilde{g}} + \left(\frac{\partial \tilde{\alpha}_1}{\partial \tilde{g}} - \frac{\partial \tilde{k}}{\partial \tilde{g}}\right)\right] \tag{C.39a}$$

$$\frac{\partial \bar{\tilde{C}}_1}{\partial \tilde{b}} = \tau \frac{\partial \tilde{C}_1}{\partial \tilde{b}} = \frac{2\tau}{\tilde{b}\tilde{\eta}}\left(-\frac{\partial \tilde{\mu}}{\partial \tilde{g}} + \frac{\tilde{\alpha}_2}{\tilde{\eta}}\frac{\partial \tilde{\eta}}{\partial \tilde{g}}\right) \tag{C.39b}$$

$$\frac{\partial \bar{\tilde{C}}_2}{\partial \tilde{g}} = \tau \frac{\partial \tilde{C}_2}{\partial \tilde{g}} = -\frac{2\tau}{\tilde{\eta}}\left(\frac{\partial \tilde{\alpha}_1}{\partial \tilde{b}} - \frac{\partial \tilde{k}}{\partial \tilde{b}}\right) \tag{C.39c}$$

$$\frac{\partial \bar{\tilde{C}}_2}{\partial \tilde{b}} = \tau \frac{\partial \tilde{C}_2}{\partial \tilde{b}} = -\frac{2\tau}{\tilde{\eta}}\frac{\partial \tilde{\alpha}_2}{\partial \tilde{b}} \tag{C.39d}$$

and

$$\frac{\partial\tilde{\alpha}_1}{\partial\tilde{g}} = -\left(\frac{\tilde{b}^2+1-2\ln\tilde{b}}{2\tilde{b}}\right)\frac{\partial\tilde{\mu}}{\partial\tilde{g}} \tag{C.40a}$$

$$\frac{\partial\tilde{k}}{\partial\tilde{g}} = \left(\frac{\tilde{b}^2-1-2\ln\tilde{b}}{2\tilde{b}}\right)\left(2\frac{\partial\tilde{\mu}}{\partial\tilde{g}}+\tilde{g}\frac{\partial^2\tilde{\mu}}{\partial\tilde{g}^2}\right) \tag{C.40b}$$

$$\frac{\partial\tilde{\alpha}_2}{\partial\tilde{g}} = \frac{1}{\tilde{b}}\frac{\partial\tilde{\mu}}{\partial\tilde{g}} \tag{C.40c}$$

$$\frac{\partial\tilde{\alpha}_1}{\partial\tilde{b}} = \frac{\tilde{\mu}}{2\tilde{b}^2}(3-\tilde{b}^2-2\ln\tilde{b}) \tag{C.40d}$$

$$\frac{\partial\tilde{k}}{\partial\tilde{b}} = \left(\tilde{g}\frac{\partial\tilde{\mu}}{\partial\tilde{g}}+\tilde{\mu}\right)\left(\frac{\tilde{b}^2-1+2\ln\tilde{b}}{2\tilde{b}^2}\right) \tag{C.40e}$$

$$\frac{\partial\tilde{\alpha}_2}{\partial\tilde{b}} = -\frac{\tilde{\mu}}{\tilde{b}^2} \tag{C.40f}$$

Further, using (C.11) and (C.12), we can calculate the non-dimensional thermodynamic quantities as follows:

$$\begin{aligned}\psi(t) &= \frac{\mu[b^2(t)-1-2\ln(b(t))]}{2\rho b(t)} \\ &= \frac{\mu[b^2(t)-1-2\ln(b(t))]b(t)g(t)}{2\rho_r b(t)} \\ \Rightarrow \bar{\tilde{\psi}} = 2\frac{\psi(\bar{t})\rho_r}{T_{zz}(0)} &= \bar{\tilde{\mu}}\left(\tilde{b}^2-1-2\ln\tilde{b}\right)\tilde{g}\end{aligned} \tag{C.41}$$

and

$$\begin{aligned}\hat{\xi}(t) &= \eta\left(\dot{g}(t)\frac{b(t)}{g(t)}\right)^2 \\ \Rightarrow \bar{\tilde{\xi}} = \frac{\hat{\xi}(\bar{t})}{\hat{\eta}} &= \bar{\tilde{\eta}}\left(\frac{\tilde{g}'}{\tau}\frac{\tilde{b}}{\tilde{g}}\right)^2\end{aligned} \tag{C.42}$$

Typical plots obtained for the given material by calculating the solution to the semi-inverse creep problem using MATLAB [55] and the material parameters in Table I are depicted in Figure 3 and Figure 4. The material model is subject to a sudden (step) normal stress and the deformation response shows the viscoelastic nature of

Table I.: Parameters employed for the study of the material response when subject to one dimensional constrained compression. Also used in Chapter IV for finite element calculations

$\hat{\mu}$, (MPa)	n_1	λ_1	q_1	$\hat{\eta}$, (MPa.s)	n_2	λ_2	q_2
810	4.0	0.25	-15	1400	2.5	0.25	-25

the material. The strain lags behind stress owing to the material's viscoelasticity. Upon instantaneous removal of load the material rebounds partial to attain a permanent strain. A plot of some of the relevant field variables calculated after obtaining the solution is presented in Figure 4, the non-dimensionalized stored energy, $\bar{\bar{\psi}}$, has negative values owing the the non-dimensionalization of $\bar{\mu}$ with respect to $\bar{T}_{zz}(0)$. The stored energy starts off high and then dissipates (though the rate of dissipation decreases) to become zero upon unloading. The natural configuration of the material evolves as well during the process and its evolution is also presented in Figure 4. The plot shows that the material does return to a natural (stress-free) configuration upon unloading, thereby the dissipation occurs due to a change in microstructure of the material.

3. Stress Relaxation

We can similarly derive governing equations of motion for the 1D deformation under a constant applied strain (Figure 5), i.e. with respect to the current configuration, and observe the corresponding stress response as a function of time. Consider (C.20), now for a constant strain rate experiment (using (C.3b)) we will have

$$\mathbf{e}_{zz}(t) = \frac{1}{2}\left\{1 - \frac{1}{\Lambda^2(t)}\right\} = C, \text{ a constant} \tag{C.43}$$

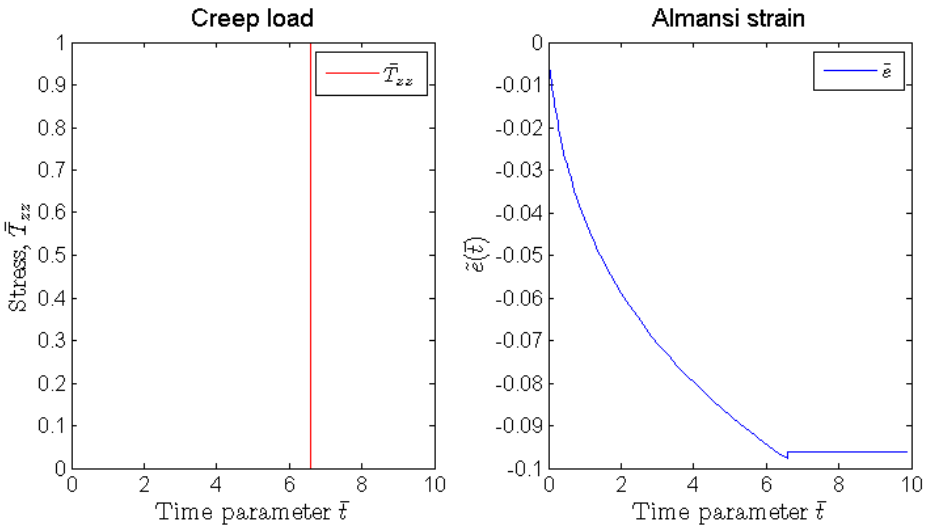

Fig. 3.: Creep solution for the material model for HMA, kinematical terms are non-dimensional quantities

$$\Rightarrow \Lambda(t) = \frac{1}{\sqrt{1-2C}} \tag{C.44}$$

Now substituting (C.44) in (C.17b), we obtain

$$\dot{b}(t) = \frac{1}{2b(t)}\left[C_1 + C_2 b^2(t)\right] \tag{C.45}$$

subject to the initial conditions given by

$$\begin{aligned} &\mathbf{e}_{zz}(0) = 0 \Rightarrow \Lambda(0) = \pm 1 \text{ (we will consider the positive initial stretch, } \Lambda(0) = 1) \\ &\Rightarrow b(0) = \frac{1}{\Lambda(0)};\ g(0) = 1 \text{ (in initial reference configuration } \mathbf{D}_{\kappa_r} = \mathbf{G} = \mathbf{I}) \end{aligned} \tag{C.46}$$

We, thereafter, solve (C.44) and (C.45) simultaneously for $g(t)$ and $b(t)$ and calculate the Cauchy stress components T_{rr}, $T_{\theta\theta}$ and T_{zz} using (C.16), (C.24) and (C.22).

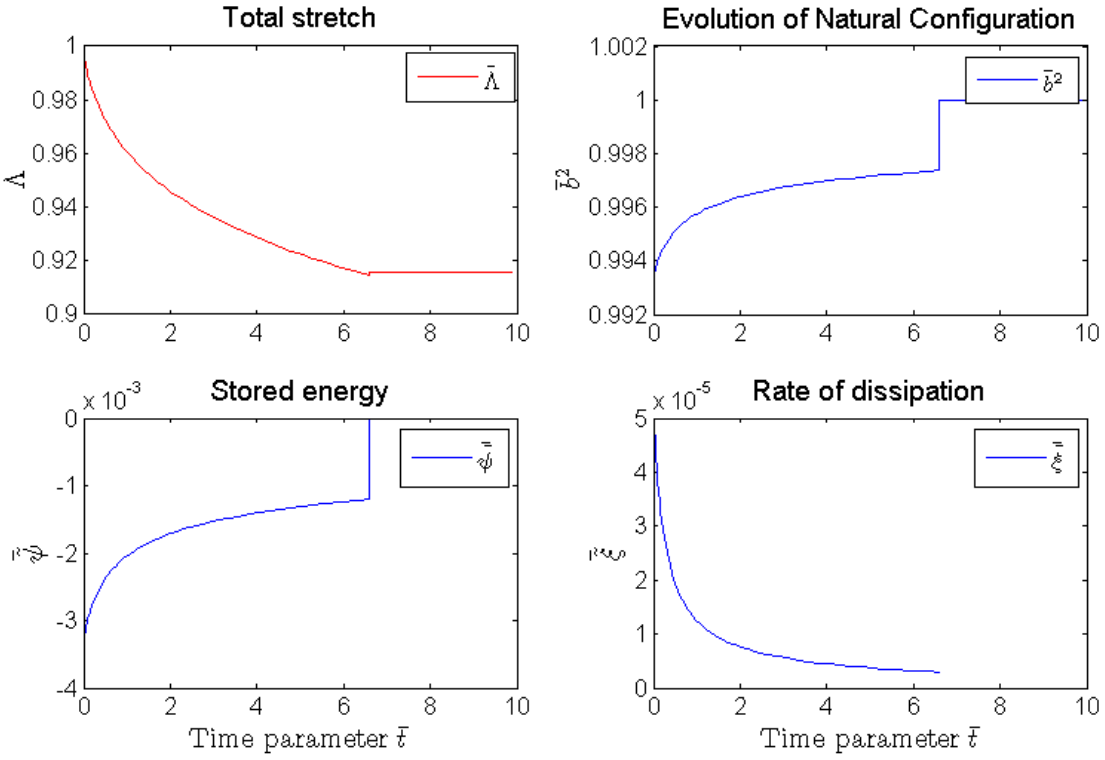

Fig. 4.: Field variables calculated from the solution to the one dimensional creep problem, all quantities have been non-dimensionalized

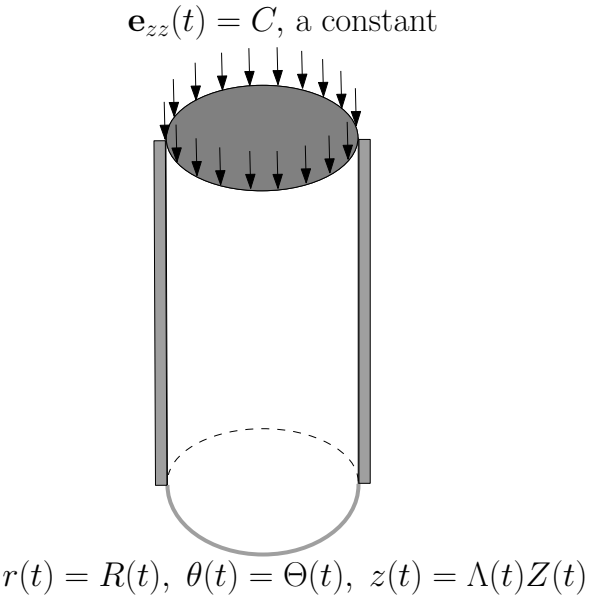

Fig. 5.: Schematic for the one-dimensional stress relaxation problem

a. Dimensionless Form for Governing Equations of Stress Relaxation

Now using the earlier representations for time normalization, $\tilde{(.)}$, and normalization with respect to a context relevant quantity, $\bar{(.)}$, we can write the governing equations of motion for the stress relaxation as follows:

Firstly, we redefine some of the non-dimensional quantities as

$$\bar{\tilde{\mu}} = \frac{\tilde{\mu}}{\hat{\mu}} \tag{C.47a}$$

$$\bar{\tilde{\alpha}}_1 = \frac{\tilde{\alpha}_1}{\hat{\mu}} \tag{C.47b}$$

$$\bar{\tilde{\alpha}}_2 = \frac{\tilde{\alpha}_2}{\hat{\mu}} \tag{C.47c}$$

$$\begin{aligned} \bar{\tilde{T}}_{zz} &= \frac{\tilde{T}_{zz}}{\hat{\mu}} \\ &= \bar{\tilde{\mu}} \left[\tilde{b} - \frac{1}{2} \left\{ \tilde{b} + \frac{1}{\tilde{b}} - 2\frac{\ln(\tilde{b})}{\tilde{b}} \right\} \right] \end{aligned} \tag{C.47d}$$

and obtain the relation between the two different types of time derivative as:

$$\begin{aligned}\dot{b}(t) &= \left(\tilde{b}(\bar{t})\right)' (\dot{\bar{t}}) \\ &= \frac{1}{\tau}\left(\tilde{b}(\bar{t})\right)'\end{aligned} \tag{C.48}$$

we henceforth use concise notation by dropping the use of explicit arguments, and write the governing equations as

$$\tilde{b}\tilde{g} = \frac{1}{\sqrt{1-2\bar{C}}} \tag{C.49}$$

$$\begin{aligned}(\tilde{b})' &= \frac{\tau}{2\tilde{b}}\left[\tilde{C}_1 + \tilde{C}_2\tilde{b}^2\right] \\ &= \frac{1}{2\tilde{b}}\left[\bar{\tilde{C}}_1 + \bar{\tilde{C}}_2\tilde{b}^2\right]\end{aligned} \tag{C.50}$$

(C.49) and (C.50) are to be solved for $\tilde{g}$ and $\tilde{b}$, subject to the initial conditions:

$$\tilde{g}(0) = 1;\ \tilde{b}(0) = \frac{1}{\Lambda(0)} = \frac{1}{\sqrt{1-2\bar{C}}} \tag{C.51}$$

Thereafter, the stress components can be calculated using the expressions in (C.47b), (C.47c), (C.34) and (C.47d). Also, we calculate the non-dimensional thermodynamic quantities using

$$\bar{\tilde{\psi}} = 2\frac{\psi(\bar{t})\rho_r}{\hat{\mu}} = \bar{\tilde{\mu}}\left(\tilde{b}^2 - 1 - 2\ln\tilde{b}\right)\tilde{g} \tag{C.52}$$

and

$$\bar{\tilde{\xi}} = \frac{\hat{\xi}(\bar{t})}{\hat{\eta}} = \bar{\tilde{\eta}}\left(\frac{\tilde{g}'}{\tau}\frac{\tilde{b}}{\tilde{g}}\right)^2 \tag{C.53}$$

The above analysis for calculating the response of the model to a step input strain results in the characteristics shown in Figure 6. The applied compressive strain is 0.005 and the resultant stress response, non-dimensionalized with respect to $\bar{\hat{\mu}}$,

depicted in Figure 6 shows that the stress relaxes slowly and reaches a stress-free state. The stress-free state is reached after the material dissipates the stored energy due to changes in the microstructure. It is to be noted again that the non-dimensionalized stored energy, $\bar{\bar{\psi}}$, has negative values owing the the non-dimensionalization of $\bar{\mu}$ with respect to $\bar{T}_{zz}(0)$.

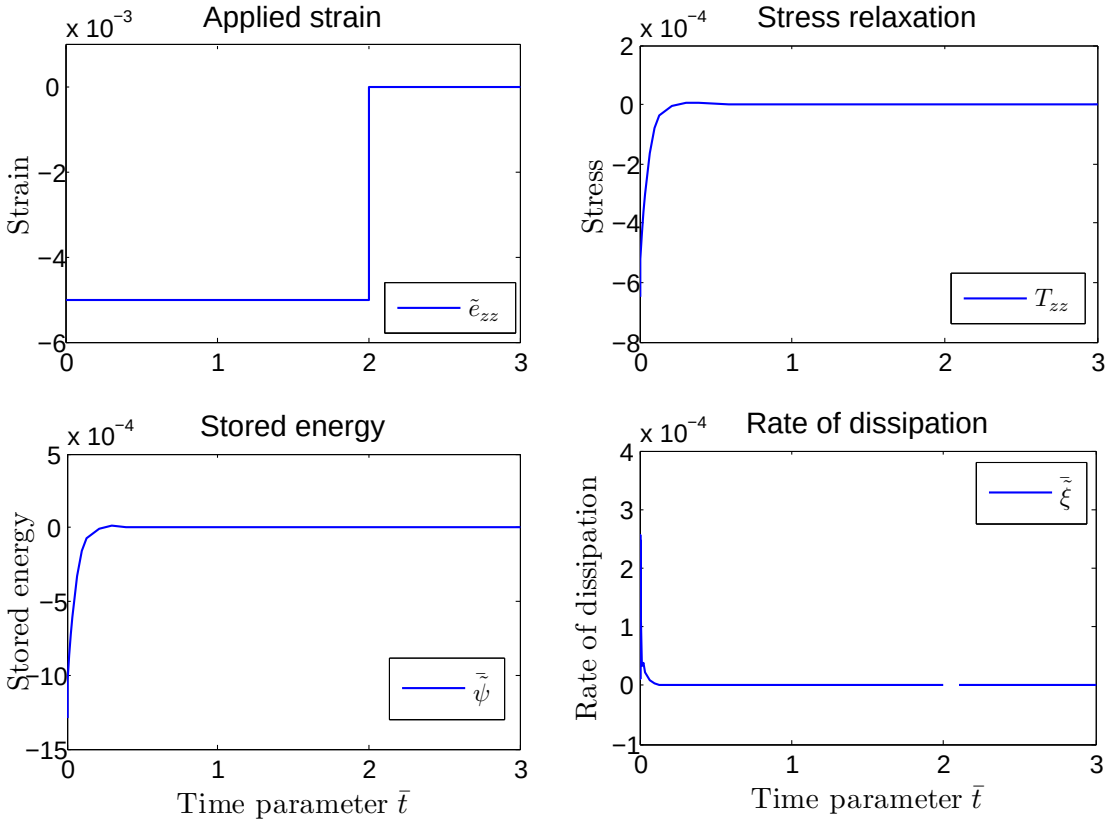

Fig. 6.: Field variables calculated from the solution to the one dimensional constant strain problem, all quantities have been non-dimensionalized

CHAPTER IV

NUMERICAL IMPLEMENTATION IN THE FINITE ELEMENT METHOD

The modeling framework and the proposed model for compaction were introduced earlier. This model will be further developed and improved in this study to account for the behavior of HMA subjected to compaction in the field. To this end the model was implemented in ABAQUS [8] and in the three-dimensional Computer Aided Pavement Analysis, CAPA-3D, finite element software developed at the Delft University of Technology, Netherlands ([56], [57]). CAPA-3D has been developed as a finite element based platform to serve the computational needs of the research group *Mechanics of Structural Systems* at TU Delft and of those international teams which cooperate with them. Over the years, it has evolved into a fully fledged finite element system for static or dynamic analysis of very large scale three dimensional pavement and soil engineering models. It consists of a sophisticated user interface, a powerful highly parallelized band-optimizing mesh generator, high quality user controlled graphical output, several material and element types, and a variety of specialized algorithms for the more efficient analysis of pavement constructions. Among others, these include a moving load simulation algorithm and a contact algorithm. These algorithms are essential for modeling the compaction process.

A. Finite Element Implementation of the Model

We can schematically visualize the incremental evolution of the natural configuration in Figure 7 as the material deforms under external influences.

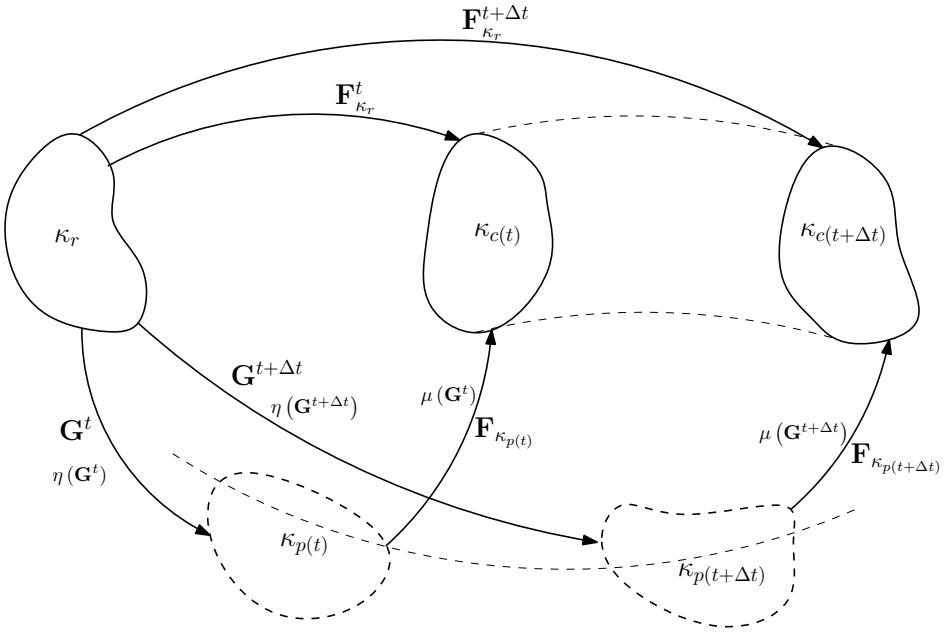

Fig. 7.: Representation of the incremental evolution of 'natural configuration'

1. Invariants of $\mathbf{B}_{\kappa_{p(t)}}$ and $\mathbf{G}$

Let us define the invariants of $\mathbf{B}_{\kappa_{p(t)}}$ as follows:

$$\mathrm{I}_{\mathbf{B}_{\kappa_{p(t)}}} = \mathrm{tr}\left(\mathbf{B}_{\kappa_{p(t)}}\right);\ \mathrm{II}_{\mathbf{B}_{\kappa_{p(t)}}} = \mathrm{tr}\left(\mathbf{B}^2_{\kappa_{p(t)}}\right);\ \mathrm{III}_{\mathbf{B}_{\kappa_{p(t)}}} = \det\left(\mathbf{B}_{\kappa_{p(t)}}\right) \tag{A.1}$$

We use similar definitions for the invariants of $\mathbf{G}$, presently, we write:

$$\mathrm{I}_{\mathbf{G}} = \mathrm{tr}\left(\mathbf{G}\right);\ \mathrm{II}_{\mathbf{G}} = \mathrm{tr}\left(\mathbf{G}^2\right);\ \mathrm{III}_{\mathbf{G}} = \det\left(\mathbf{G}\right) \tag{A.2}$$

For the sake of brevity we introduce the following notation in the matter that follows:

a. Notation for subscripts

κ_r becomes r

$\kappa_{r\to p(t)}$ becomes VE(*referring to the Viscous Evolution*)

$\kappa_{p(t)}$ becomes pe

$(\cdot)$ signifies scalar product between two tensors

Therefore, we have, for example

$$\mathbf{F}_{\kappa_r} = \mathbf{F}_r \tag{A.3a}$$

$$\mathbf{C}_{\kappa_r \to \kappa_{p(t)}} = \mathbf{C}_{VE} \tag{A.3b}$$

$$\mathbf{F}_{\kappa_{p(t)}} = \mathbf{F}_{pe} \tag{A.3c}$$

$$\mathbf{B}_{pe} = \mathbf{F}_r \mathbf{C}_{VE}^{-1} \mathbf{F}_r^T \tag{A.3d}$$

Also, recall

$$\overset{\nabla}{\mathbf{B}}_{pe} := \dot{\mathbf{B}}_{pe} - \mathbf{L}_r \mathbf{B}_{pe} - \mathbf{B}_{pe} \mathbf{L}_r^T \tag{A.4}$$

$$= -2\mathbf{F}_{pe} \mathbf{D}_{pe} \mathbf{F}_{pe}^T \tag{A.5}$$

$$= \mathbf{F}_r \left(\dot{\overline{\mathbf{C}_{VE}^{-1}}} \right) \mathbf{F}_r^T \tag{A.6}$$

Now, using the equivalence between (A.4) and (A.6) we can write, in a numerically discretized form:

$$\begin{aligned} &\mathbf{B}_{pe}^{t+\Delta t} - \mathbf{B}_{pe}^{t} - \Delta t \left(\mathbf{L}_r^{t+\Delta t} \mathbf{B}_{pe}^{t+\Delta t} + \mathbf{B}_{pe}^{t+\Delta t} \left(\mathbf{L}_r^T \right)^{t+\Delta t} \right) \\ &= \mathbf{F}_r^{t+\Delta t} \left(\left(\mathbf{C}_{VE}^{-1} \right)^{t+\Delta t} - \left(\mathbf{C}_{VE}^{-1} \right)^{t} \right) \left(\mathbf{F}_r^T \right)^{t+\Delta t} \end{aligned} \tag{A.7}$$

For the sake of calculating updates to the solution satisfying a residual, we treat $\mathbf{F}_r^{t+\Delta t}$ as known for each current time increment $(t + \Delta t)$. Hence, based on (A.7) we will then have, as an example, a relationship of the following kind:

$$\begin{aligned} &\left. \frac{\partial \mathbf{B}_{pe}}{\partial \mathbf{B}_{pe}} \right|^{t+\Delta t} - \Delta t \left(\mathbf{L}_r^{t+\Delta t} \left. \frac{\partial \mathbf{B}_{pe}}{\partial \mathbf{B}_{pe}} \right|^{t+\Delta t} + \left. \frac{\partial \mathbf{B}_{pe}}{\partial \mathbf{B}_{pe}} \right|^{t+\Delta t} \left(\mathbf{L}_r^T \right)^{t+\Delta t} \right) \\ &= \mathbf{F}_r^{t+\Delta t} \left(\left. \frac{\partial \mathbf{C}_{VE}^{-1}}{\partial \mathbf{B}_{pe}} \right|^{t+\Delta t} \right) \left(\mathbf{F}_r^T \right)^{t+\Delta t} \end{aligned} \tag{A.8}$$

Hence, we can use either equivalent representations for $\overset{\nabla}{\mathbf{B}}_{pe}$, according to the choice of the quantity we want to calculate. We only need to be aware that $\mathbf{F}_r$ is to be treated as a 'known' value during computations of the components of the iteration jacobian.

2. Residual Equation for Computing $\mathbf{B}_{pe}$

Using (A.4) we can write (B.15) as

$$\dot{\mathbf{B}}_{pe} - \mathbf{L}_r\mathbf{B}_{pe} - \mathbf{B}_{pe}\mathbf{L}_r^T = -\frac{2}{\eta}\left(\alpha_2\mathbf{B}_{pe} + (\alpha_1 - k)\mathbf{I}\right) \tag{A.9}$$

Implicit numerical discretization of the evolution equation (A.9) gives us an expression that is used to form a residual equation to solve for $\mathbf{B}_{pe}$. Therefore, we have

$$\mathbf{B}_{pe}^{t+\Delta t} - \mathbf{B}_{pe}^{t} - \Delta t\left(\mathbf{L}_r^{t+\Delta t}\mathbf{B}_{pe}^{t+\Delta t} + \mathbf{B}_{pe}^{t+\Delta t}\left(\mathbf{L}_r^T\right)^{t+\Delta t}\right) = -\frac{2\Delta t}{\eta}\left(\alpha_2\mathbf{B}_{pe}^{t+\Delta t} + (\alpha_1 - k)\mathbf{I}\right) \tag{A.10}$$

and the required residual equation can be written as follows

$$\begin{aligned}\mathbf{R}^{t+\Delta t} :=& \mathbf{B}_{pe}^{t+\Delta t} - \mathbf{B}_{pe}^{t} - \Delta t\left(\mathbf{L}_r^{t+\Delta t}\mathbf{B}_{pe}^{t+\Delta t} + \mathbf{B}_{pe}^{t+\Delta t}\left(\mathbf{L}_r^T\right)^{t+\Delta t}\right) \\ &+ \frac{2\Delta t}{\eta}\left(\alpha_2\mathbf{B}_{pe}^{t+\Delta t} + (\alpha_1 - k)\mathbf{I}\right)\end{aligned} \tag{A.11}$$

which can be written, dropping the superscripts indicating current time integration step, as

$$\mathbf{R} := \mathbf{B}_{pe} - \mathbf{B}_{pe}^{t} - \Delta t\left(\mathbf{L}_r\mathbf{B}_{pe} + \mathbf{B}_{pe}\mathbf{L}_r^T\right) + \frac{2\Delta t}{\eta}\left(\alpha_2\mathbf{B}_{pe} + (\alpha_1 - k)\mathbf{I}\right) \tag{A.12}$$

a. Jacobian of Iteration for the Residual $\mathbf{R}(\mathbf{B}_{pe})$

Now using (A.12) we form the required jacobian as follows [1]:

$$\frac{\partial \mathbf{R}}{\partial \mathbf{B}_{pe}} = \frac{\partial \mathbf{B}_{pe}}{\partial \mathbf{B}_{pe}} - \Delta t \left(\mathbf{L}_r \frac{\partial \mathbf{B}_{pe}}{\partial \mathbf{B}_{pe}} + \frac{\partial \mathbf{B}_{pe}}{\partial \mathbf{B}_{pe}} \mathbf{L}_r^T \right) + 2\Delta t \left[\alpha_2 \mathbf{B}_{pe} + (\alpha_1 - k)\mathbf{I} \right] \otimes \frac{\partial \eta^{-1}}{\partial \mathbf{B}_{pe}} + \frac{2\Delta t}{\eta} \left[\mathbf{B}_{pe} \otimes \frac{\partial \alpha_2}{\partial \mathbf{B}_{pe}} + \alpha_2 \frac{\partial \mathbf{B}_{pe}}{\partial \mathbf{B}_{pe}} + \mathbf{I} \otimes \left(\frac{\partial \alpha_1}{\partial \mathbf{B}_{pe}} - \frac{\partial k}{\partial \mathbf{B}_{pe}} \right) \right] \tag{A.13}$$

Now we need to calculate $\frac{\partial \eta^{-1}}{\partial \mathbf{B}_{pe}}$, $\frac{\partial \alpha_1}{\partial \mathbf{B}_{pe}}$, $\frac{\partial \alpha_2}{\partial \mathbf{B}_{pe}}$ and $\frac{\partial k}{\partial \mathbf{B}_{pe}}$ which are dependent on the derivative $\frac{\partial \mathrm{III}_{\mathbf{G}}}{\partial \mathbf{B}_{pe}}$. We therefore first calculate this as follows,

$$\begin{aligned} \frac{\partial \mathrm{III}_{\mathbf{G}}}{\partial \mathbf{B}_{pe}} &= \mathrm{III}_{\mathbf{F}_r} \frac{\partial \left(\sqrt{\mathrm{III}_{\mathbf{B}_{pe}}} \right)^{-1}}{\partial \mathbf{B}_{pe}} \\ &= -\frac{\mathrm{III}_{\mathbf{F}_r}}{2\mathrm{III}_{\mathbf{B}_{pe}}^{3/2}} \frac{\partial \mathrm{III}_{\mathbf{B}_{pe}}}{\partial \mathbf{B}_{pe}} \\ &= -\frac{\mathrm{III}_{\mathbf{F}_r}}{2\sqrt{\mathrm{III}_{\mathbf{B}_{pe}}}} \mathbf{B}_{pe}^{-T} \end{aligned} \tag{A.14}$$

Now,

$$\frac{\partial \mu}{\partial \mathrm{III}_{\mathbf{G}}} = 2\hat{\mu} n_1 \lambda_1 q_1 \mathrm{III}_{\mathbf{G}}^{(2n_1-1)} \left(1 + \lambda_1 \mathrm{III}_{\mathbf{G}}^{2n_1} \right)^{(q_1-1)} \tag{A.15}$$

$$\begin{aligned} \frac{\partial \mu}{\partial \mathbf{B}_{pe}} &= 2\hat{\mu} n_1 \lambda_1 q_1 \mathrm{III}_{\mathbf{G}}^{(2n_1-1)} \left(1 + \lambda_1 \mathrm{III}_{\mathbf{G}}^{2n_1} \right)^{(q_1-1)} \frac{\partial \mathrm{III}_{\mathbf{G}}}{\partial \mathbf{B}_{pe}} \\ &= \underbrace{\left(2\hat{\mu} n_1 \lambda_1 q_1 \mathrm{III}_{\mathbf{G}}^{(2n_1-1)} \left(1 + \lambda_1 \mathrm{III}_{\mathbf{G}}^{2n_1} \right)^{(q_1-1)} \left(-\frac{\mathrm{III}_{\mathbf{F}_r}}{2\sqrt{\mathrm{III}_{\mathbf{B}_{pe}}}} \right) \right)}_{\alpha} \mathbf{B}_{pe}^{-T} \\ &= \alpha \mathbf{B}_{pe}^{-T} \end{aligned} \tag{A.16}$$

[1] Most long calculations in this chapter have been made exploiting the indicial form for the equations and then the result is presented here in direct notation owing to its typographical clarity

$$\begin{aligned}
\frac{\partial \eta^{-1}}{\partial \mathbf{B}_{pe}} &= -\frac{1}{\eta^2}\frac{\partial \eta}{\partial \mathbf{B}_{pe}} \\
&= -\frac{1}{\eta^2}\frac{\partial \eta}{\partial \mathrm{III}_{\mathbf{G}}}\frac{\partial \mathrm{III}_{\mathbf{G}}}{\partial \mathbf{B}_{pe}} \\
&= -\frac{1}{\eta^2}\underbrace{\left(2\hat{\eta} n_2 \lambda_2 q_2 \mathrm{III}_{\mathbf{G}}^{(2n_2-1)}\left(1+\lambda_2 \mathrm{III}_{\mathbf{G}}^{2n_2}\right)^{(q_2-1)}\left(-\frac{\mathrm{III}_{\mathbf{F}_r}}{2\sqrt{\mathrm{III}_{\mathbf{B}_{pe}}}}\right)\right)}_{\beta}\mathbf{B}_{pe}^{-T} \\
&= -\frac{\beta}{\eta^2}\mathbf{B}_{pe}^{-T}
\end{aligned} \tag{A.17}$$

$$\begin{aligned}
\frac{\partial \alpha_2}{\partial \mathbf{B}_{pe}} &= \frac{\partial}{\partial \mathrm{III}_{\mathbf{B}_{pe}}}\left(\frac{\mu}{\sqrt{\mathrm{III}_{\mathbf{B}_{pe}}}}\right) \\
&= \frac{1}{\sqrt{\mathrm{III}_{\mathbf{B}_{pe}}}}\left(\frac{\partial \mu}{\partial \mathbf{B}_{pe}} - \frac{\mu}{2}\mathbf{B}_{pe}^{-T}\right) \\
&= \frac{1}{\sqrt{\mathrm{III}_{\mathbf{B}_{pe}}}}\left(\alpha - \frac{\mu}{2}\right)\mathbf{B}_{pe}^{-T}
\end{aligned} \tag{A.18}$$

$$\begin{aligned}
\frac{\partial \alpha_1}{\partial \mathbf{B}_{pe}} &= \frac{\partial}{\partial \mathbf{B}_{pe}}\left[-\frac{\mu}{2\sqrt{\mathrm{III}_{\mathbf{B}_{pe}}}}\left(\mathrm{I}_{\mathbf{B}_{pe}} - 1 - \ln(\mathrm{III}_{\mathbf{B}_{pe}})\right)\right] \\
&= -\left[\frac{\left(\mathrm{I}_{\mathbf{B}_{pe}} - 1 - \ln(\mathrm{III}_{\mathbf{B}_{pe}})\right)}{2\sqrt{\mathrm{III}_{\mathbf{B}_{pe}}}}\frac{\partial \mu}{\partial \mathbf{B}_{pe}} - \frac{\mu\left(\mathrm{I}_{\mathbf{B}_{pe}} - 1 - \ln(\mathrm{III}_{\mathbf{B}_{pe}})\right)}{4\mathrm{III}_{\mathbf{B}_{pe}}^{3/2}}\frac{\partial \mathrm{III}_{\mathbf{B}_{pe}}}{\partial \mathbf{B}_{pe}}\right. \\
&\quad \left. + \frac{\mu}{2\sqrt{\mathrm{III}_{\mathbf{B}_{pe}}}}\left(\mathbf{I} - \frac{1}{\mathrm{III}_{\mathbf{B}_{pe}}}\frac{\partial \mathrm{III}_{\mathbf{B}_{pe}}}{\partial \mathbf{B}_{pe}}\right)\right] \\
&= \overbrace{-\frac{1}{2\sqrt{\mathrm{III}_{\mathbf{B}_{pe}}}}\left[\left(\alpha - \frac{\mu}{2}\right)\left(\mathrm{I}_{\mathbf{B}_{pe}} - 1 - \ln(\mathrm{III}_{\mathbf{B}_{pe}})\right) - \mu\right]}^{\sigma}\mathbf{B}_{pe}^{-T} \\
&\quad - \frac{\mu}{2\sqrt{\mathrm{III}_{\mathbf{B}_{pe}}}}\mathbf{I} \\
&= \sigma \mathbf{B}_{pe}^{-T} - \frac{\mu}{2\sqrt{\mathrm{III}_{\mathbf{B}_{pe}}}}\mathbf{I}
\end{aligned} \tag{A.19}$$

$$
\begin{aligned}
\frac{\partial k}{\partial \mathbf{B}_{pe}} &= \frac{\partial}{\partial \mathbf{B}_{pe}}\left[\frac{1}{2\sqrt{\mathrm{III}_{\mathbf{B}_{pe}}}}\left(\mathrm{I}_{\mathbf{B}_{pe}}-3-\ln(\mathrm{III}_{\mathbf{B}_{pe}})\right)\left(\mathrm{III}_{\mathbf{G}}\frac{\partial \mu}{\partial \mathrm{III}_{\mathbf{G}}}+\mu\right)\right] \\
&= \left(\mathrm{I}_{\mathbf{B}_{pe}}-3-\ln(\mathrm{III}_{\mathbf{B}_{pe}})\right)\left(\mathrm{III}_{\mathbf{G}}\frac{\partial \mu}{\partial \mathrm{III}_{\mathbf{G}}}+\mu\right)\left(-\frac{1}{4\mathrm{III}_{\mathbf{B}_{pe}}^{3/2}}\right)\frac{\partial \mathrm{III}_{\mathbf{B}_{pe}}}{\partial \mathbf{B}_{pe}} \\
&\quad + \frac{1}{2\sqrt{\mathrm{III}_{\mathbf{B}_{pe}}}}\left(\mathrm{III}_{\mathbf{G}}\frac{\partial \mu}{\partial \mathrm{III}_{\mathbf{G}}}+\mu\right)\left(\mathbf{I}-\frac{1}{\mathrm{III}_{\mathbf{B}_{pe}}}\frac{\partial \mathrm{III}_{\mathbf{B}_{pe}}}{\partial \mathbf{B}_{pe}}\right) \\
&\quad + \frac{\left(\mathrm{I}_{\mathbf{B}_{pe}}-3-\ln(\mathrm{III}_{\mathbf{B}_{pe}})\right)}{2\sqrt{\mathrm{III}_{\mathbf{B}_{pe}}}}\Bigg(2\hat{\mu}n_1\lambda_1 q_1\frac{\partial}{\partial \mathbf{B}_{pe}}\left(\mathrm{III}_{\mathbf{G}}^{2n_1}(1+\lambda_1\mathrm{III}_{\mathbf{G}}^{2n_1})^{(q_1-1)}\right) \\
&\quad + \frac{\partial \mu}{\partial \mathbf{B}_{pe}}\Bigg) \\
&= -\frac{\left(\mathrm{I}_{\mathbf{B}_{pe}}-3-\ln(\mathrm{III}_{\mathbf{B}_{pe}})\right)}{4\sqrt{\mathrm{III}_{\mathbf{B}_{pe}}}}\left(\mathrm{III}_{\mathbf{G}}\frac{\partial \mu}{\partial \mathrm{III}_{\mathbf{G}}}+\mu\right)\mathbf{B}_{pe}^{-T} \\
&\quad + \frac{1}{2\sqrt{\mathrm{III}_{\mathbf{B}_{pe}}}}\left(\mathrm{III}_{\mathbf{G}}\frac{\partial \mu}{\partial \mathrm{III}_{\mathbf{G}}}+\mu\right)\left(\mathbf{I}-\mathbf{B}_{pe}^{-T}\right)+\frac{\left(\mathrm{I}_{\mathbf{B}_{pe}}-3-\ln(\mathrm{III}_{\mathbf{B}_{pe}})\right)}{2\sqrt{\mathrm{III}_{\mathbf{B}_{pe}}}} \\
&\quad \Bigg[2\hat{\mu}n_1\lambda_1 q_1\Bigg\{2n_1\mathrm{III}_{\mathbf{G}}^{2n_1-1}(1+\lambda_1\mathrm{III}_{\mathbf{G}}^{2n_1})^{(q_1-1)}+2n_1\lambda_1(q_1-1)\mathrm{III}_{\mathbf{G}}^{4n_1-1} \\
&\quad (1+\lambda_1\mathrm{III}_{\mathbf{G}}^{2n_1})^{(q_1-2)}\Bigg\}\frac{\partial \mathrm{III}_{\mathbf{G}}}{\partial \mathbf{B}_{pe}}+\alpha\mathbf{B}_{pe}^{-T}\Bigg] \\
&= \gamma\mathbf{I}+\omega\mathbf{B}_{pe}^{-T} \qquad \text{(A.20)}
\end{aligned}
$$

where,

$$
\gamma = \frac{1}{2\sqrt{\mathrm{III}_{\mathbf{B}_{pe}}}}\left(\mathrm{III}_{\mathbf{G}}\frac{\partial \mu}{\partial \mathrm{III}_{\mathbf{G}}}+\mu\right) \qquad \text{(A.21)}
$$

$$
\begin{aligned}
\omega = & -\frac{\left(\mathrm{I}_{\mathbf{B}_{pe}}-3-\ln(\mathrm{III}_{\mathbf{B}_{pe}})\right)}{4\sqrt{\mathrm{III}_{\mathbf{B}_{pe}}}}\left(\mathrm{III}_{\mathbf{G}}\frac{\partial\mu}{\partial\mathrm{III}_{\mathbf{G}}}+\mu\right)-\frac{1}{2\sqrt{\mathrm{III}_{\mathbf{B}_{pe}}}}\Bigg(\mathrm{III}_{\mathbf{G}}\frac{\partial\mu}{\partial\mathrm{III}_{\mathbf{G}}} \\
& +\mu\Bigg)+\frac{\left(\mathrm{I}_{\mathbf{B}_{pe}}-3-\ln(\mathrm{III}_{\mathbf{B}_{pe}})\right)}{2\sqrt{\mathrm{III}_{\mathbf{B}_{pe}}}}\Bigg[4\hat{\mu}n_1^2\lambda_1q_1\mathrm{III}_{\mathbf{G}}^{2n_1-1}(1+\lambda_1\mathrm{III}_{\mathbf{G}}^{2n_1})^{(q_1-2)} \\
& \left\{1+\lambda_1\mathrm{III}_{\mathbf{G}}^{2n_1}+\lambda_1(q_1-1)\mathrm{III}_{\mathbf{G}}^{2n_1}\right\}\left(-\frac{\mathrm{III}_{\mathbf{F}_r}}{2\sqrt{\mathrm{III}_{\mathbf{B}_{pe}}}}\right)+\alpha\Bigg] \\
= & -\frac{\left(\mathrm{I}_{\mathbf{B}_{pe}}-1-\ln(\mathrm{III}_{\mathbf{B}_{pe}})\right)}{4\sqrt{\mathrm{III}_{\mathbf{B}_{pe}}}}\left(\mathrm{III}_{\mathbf{G}}\frac{\partial\mu}{\partial\mathrm{III}_{\mathbf{G}}}+\mu\right)+\frac{\left(\mathrm{I}_{\mathbf{B}_{pe}}-3-\ln(\mathrm{III}_{\mathbf{B}_{pe}})\right)}{2\sqrt{\mathrm{III}_{\mathbf{B}_{pe}}}} \\
& \Bigg[4\hat{\mu}n_1^2\lambda_1q_1\mathrm{III}_{\mathbf{G}}^{2n_1-1}(1+\lambda_1\mathrm{III}_{\mathbf{G}}^{2n_1})^{(q_1-2)}\left\{1+\lambda_1q_1\mathrm{III}_{\mathbf{G}}^{2n_1}\right\} \\
& \left(-\frac{\mathrm{III}_{\mathbf{G}}}{2}\right)+\alpha\Bigg] \\
= & -\frac{\left(\mathrm{I}_{\mathbf{B}_{pe}}-1-\ln(\mathrm{III}_{\mathbf{B}_{pe}})\right)}{4\sqrt{\mathrm{III}_{\mathbf{B}_{pe}}}}\left(\mathrm{III}_{\mathbf{G}}\frac{\partial\mu}{\partial\mathrm{III}_{\mathbf{G}}}+\mu\right)+\frac{\left(\mathrm{I}_{\mathbf{B}_{pe}}-3-\ln(\mathrm{III}_{\mathbf{B}_{pe}})\right)}{2\sqrt{\mathrm{III}_{\mathbf{B}_{pe}}}} \qquad \text{(A.22)} \\
& \Bigg[\alpha-2\hat{\mu}n_1^2\lambda_1q_1\mathrm{III}_{\mathbf{G}}^{2n_1}(1+\lambda_1\mathrm{III}_{\mathbf{G}}^{2n_1})^{(q_1-2)}\left\{1+\lambda_1q_1\mathrm{III}_{\mathbf{G}}^{2n_1}\right\}\Bigg]
\end{aligned}
$$

Now substituting (A.20), (A.19), (A.18) and (A.17) in (A.13), we obtain

$$\begin{aligned}
\frac{\partial \mathbf{R}}{\partial \mathbf{B}_{pe}} =& \Big(1+\underbrace{\frac{2\Delta t}{\eta}\alpha_2}_{\delta}\Big)\mathbf{I_4} - \Delta t(\mathbf{L}_r\mathbf{I_4}+\mathbf{I_4}\mathbf{L}_r^T) - \frac{2\Delta t}{\eta}\frac{\beta}{\eta}\left[\alpha_2\mathbf{B}_{pe}+(\alpha_1-k)\mathbf{I}\right] \\
& \otimes \mathbf{B}_{pe}^{-T} + \frac{2\Delta t}{\eta}\Bigg[\frac{1}{\sqrt{\mathrm{III}_{\mathbf{B}_{pe}}}}\Big(\alpha-\frac{\mu}{2}\Big)\mathbf{B}_{pe}\otimes\mathbf{B}_{pe}^{-T} + \mathbf{I}\otimes\Bigg((\sigma-\omega)\mathbf{B}_{pe}^{-T} \\
& - \big(\frac{\mu}{2\sqrt{\mathrm{III}_{\mathbf{B}_{pe}}}}+\gamma\big)\mathbf{I}\Bigg)\Bigg] \\
=& (1+\delta\alpha_2)\mathbf{I_4} - \Delta t(\mathbf{L}_r\mathbf{I_4}+\mathbf{I_4}\mathbf{L}_r^T) - \delta\Bigg[\frac{\beta\alpha_2}{\eta}\mathbf{B}_{pe}\otimes\mathbf{B}_{pe}^{-T} \qquad \text{(A.23)} \\
& + \frac{\beta}{\eta}(\alpha_1-k)\mathbf{I}\otimes\mathbf{B}_{pe}^{-T} - \Bigg\{\frac{1}{\sqrt{\mathrm{III}_{\mathbf{B}_{pe}}}}\Big(\alpha-\frac{\mu}{2}\Big)\mathbf{B}_{pe}\otimes\mathbf{B}_{pe}^{-T} \\
& + (\sigma-\omega)\mathbf{I}\otimes\mathbf{B}_{pe}^{-T} - \Big(\frac{\mu}{2\sqrt{\mathrm{III}_{\mathbf{B}_{pe}}}}+\gamma\Big)\mathbf{I}\otimes\mathbf{I}\Bigg\}\Bigg] \\
=& (1+\delta\alpha_2)\mathbf{I_4} - \Delta t(\mathbf{L}_r\mathbf{I_4}+\mathbf{I_4}\mathbf{L}_r^T) - \delta\Bigg[\Big(\frac{\beta\alpha_2}{\eta}-\frac{1}{\sqrt{\mathrm{III}_{\mathbf{B}_{pe}}}}\big(\alpha-\frac{\mu}{2}\big)\Big) \\
& \mathbf{B}_{pe}\otimes\mathbf{B}_{pe}^{-T} + \Big(\frac{\beta}{\eta}(\alpha_1-k)-(\sigma-\omega)\Big)\mathbf{I}\otimes\mathbf{B}_{pe}^{-T} \\
& + \Big(\frac{\mu}{2\sqrt{\mathrm{III}_{\mathbf{B}_{pe}}}}+\gamma\Big)\mathbf{I}\otimes\mathbf{I}\Bigg] \\
=& (1+\delta\alpha_2)\mathbf{I_4} - \Delta t(\mathbf{L}_r\mathbf{I_4}+\mathbf{I_4}\mathbf{L}_r^T) - \delta[\varphi_1\mathbf{B}_{pe}\otimes\mathbf{B}_{pe}^{-T} \qquad \text{(A.24)} \\
& + \varphi_2\mathbf{I}\otimes\mathbf{B}_{pe}^{-T} + \varphi_3\mathbf{I}\otimes\mathbf{I}]
\end{aligned}$$

with

$$\varphi_1 = \frac{\beta\alpha_2}{\eta} - \frac{1}{\sqrt{\mathrm{III}_{\mathbf{B}_{pe}}}}\big(\alpha-\frac{\mu}{2}\big) \qquad \text{(A.25a)}$$

$$\varphi_2 = \frac{\beta}{\eta}(\alpha_1-k) - (\sigma-\omega) \qquad \text{(A.25b)}$$

$$\varphi_3 = \frac{\mu}{2\sqrt{\mathrm{III}_{\mathbf{B}_{pe}}}} + \gamma \qquad \text{(A.25c)}$$

and the residual expressed as

$$\mathbf{R} := \mathbf{B}_{pe} - \mathbf{B}_{pe}^t - \Delta t\left(\mathbf{L}_r\mathbf{B}_{pe}+\mathbf{B}_{pe}\mathbf{L}_r^T\right) + \delta\left(\alpha_2\mathbf{B}_{pe}+(\alpha_1-k)\mathbf{I}\right) \qquad \text{(A.26)}$$

b. Component Representations for the Jacobian and the Residual

The jacobian and the residual given by (A.24) and (A.26), respectively, can be expressed in terms of their cartesian components as follows:

$$\begin{aligned}\left(\frac{\partial \mathbf{R}}{\partial \mathbf{B}_{pe}}\right)_{ijkl} &= (1+\delta\alpha_2)\delta_{ik}\delta_{jl} - \Delta t\left((\mathbf{L}_r)_{im}\,\delta_{mk}\delta_{jl} + \delta_{ik}\delta_{jm}\,(\mathbf{L}_r)_{lm}\right) \\ &\quad - \delta[\varphi_1(\mathbf{B}_{pe})_{ij}(\mathbf{B}_{pe}^{-T})_{kl} + \varphi_2\delta_{ij}(\mathbf{B}_{pe}^{-T})_{kl} + \varphi_3\delta_{ij}\delta_{kl}] \\ &= (1+\delta\alpha_2)\delta_{ik}\delta_{jl} - \Delta t\left((\mathbf{L}_r)_{ik}\,\delta_{jl} + \delta_{ik}\,(\mathbf{L}_r)_{lj}\right) \\ &\quad - \delta\left[(\varphi_1(\mathbf{B}_{pe})_{ij} + \varphi_2\delta_{ij})(\mathbf{B}_{pe}^{-1})_{lk} + \varphi_3\delta_{ij}\delta_{kl}\right]\end{aligned} \tag{A.27}$$

$$\begin{aligned}\mathbf{R} = &\ (\mathbf{B}_{pe})_{ij} - (\mathbf{B}_{pe}^{t})_{ij} - \Delta t\left((\mathbf{L}_r)_{im}\,(\mathbf{B}_{pe})_{mj} + (\mathbf{B}_{pe})_{im}\,(\mathbf{L}_r)_{jm}\right) \\ &+ \delta\left(\alpha_2(\mathbf{B}_{pe})_{ij} + (\alpha_1 - k)(\delta)_{ij}\right) \\ = &\ (1+\delta\alpha_2)(\mathbf{B}_{pe})_{ij} - (\mathbf{B}_{pe}^{t})_{ij} - \Delta t\left((\mathbf{L}_r)_{im}\,(\mathbf{B}_{pe})_{mj} + (\mathbf{B}_{pe})_{im}\,(\mathbf{L}_r)_{jm}\right) \\ &+ \delta(\alpha_1 - k)(\delta)_{ij}\end{aligned} \tag{A.28}$$

3. Residual Equation for Calculating $\mathbf{C}_{VE}^{-1}$

Let us begin from the evolution equation given by (B.15) and using (A.6) rewrite it in the following form:

$$\mathbf{R}^{t+\Delta t} := \left(\mathbf{C}_{VE}^{-1}\right)^{t+\Delta t} - \left(\mathbf{C}_{VE}^{-1}\right)^{t} + \frac{2\Delta t}{\eta}\left(\alpha_2\left(\mathbf{C}_{VE}^{-1}\right)^{t+\Delta t} + (\alpha_1 - k)\left(\mathbf{C}_{r}^{-1}\right)^{t+\Delta t}\right) \tag{A.29}$$

a. Jacobian of Iteration for the Residual $\mathbf{R}(\mathbf{C}_{VE}^{-1})$

Now using the above expression for $\mathbf{R}$ we can form a jacobian for the NR iteration solution for $\mathbf{C}_{VE}^{-1}$. Therefore, (dropping the superscripts) we have,

$$\frac{\partial \mathbf{R}}{\partial \mathbf{C}_{VE}^{-1}} = \frac{\partial \mathbf{C}_{VE}^{-1}}{\partial \mathbf{C}_{VE}^{-1}} + 2\Delta t \left[\alpha_2 \mathbf{C}_{VE}^{-1} + (\alpha_1 - k)\mathbf{C}_r^{-1}\right] \otimes \left(\frac{\partial \eta^{-1}}{\partial \mathbf{B}_{pe}} \frac{\partial \mathbf{B}_{pe}}{\partial \mathbf{C}_{VE}^{-1}}\right) + \frac{2\Delta t}{\eta}\left[\alpha_2 \frac{\partial \mathbf{C}_{VE}^{-1}}{\partial \mathbf{C}_{VE}^{-1}} + \mathbf{C}_{VE}^{-1} \otimes \left(\frac{\partial \alpha_2}{\partial \mathbf{B}_{pe}} \frac{\partial \mathbf{B}_{pe}}{\partial \mathbf{C}_{VE}^{-1}}\right) + \mathbf{C}_r^{-1} \otimes \left(\left(\frac{\partial \alpha_1}{\partial \mathbf{B}_{pe}} - \frac{\partial k}{\partial \mathbf{B}_{pe}}\right) \frac{\partial \mathbf{B}_{pe}}{\partial \mathbf{C}_{VE}^{-1}}\right)\right] \tag{A.30}$$

We now make use of the calculations we made for the derivatives $\frac{\partial \eta^{-1}}{\partial \mathbf{B}_{pe}}$, $\frac{\partial \alpha_1}{\partial \mathbf{B}_{pe}}$, $\frac{\partial \alpha_2}{\partial \mathbf{B}_{pe}}$ and $\frac{\partial k}{\partial \mathbf{B}_{pe}}$ in (a). Thereafter the only derivative we need to calculate is $\frac{\partial \mathbf{B}_{pe}}{\partial \mathbf{C}_{VE}^{-1}}$.

$$\begin{aligned} \frac{\partial \mathbf{B}_{pe}}{\partial \mathbf{C}_{VE}^{-1}} &= \frac{\partial}{\partial \mathbf{C}_{VE}^{-1}} \left(\mathbf{F}_r \mathbf{C}_{VE}^{-1} \mathbf{F}_r^T\right) \\ &= \mathbf{F}_r \left(\frac{\partial \mathbf{C}_{VE}^{-1}}{\partial \mathbf{C}_{VE}^{-1}}\right) \mathbf{F}_r^T \end{aligned} \tag{A.31}$$

we thereafter express (A.31) in components as:

$$\begin{aligned} \left(\frac{\partial \mathbf{B}_{pe}}{\partial \mathbf{C}_{VE}^{-1}}\right)_{ijmn} &= (\mathbf{F}_r)_{ip} \delta_{pm} \delta_{qn} (\mathbf{F}_r)_{jq} \\ &= (\mathbf{F}_r)_{im} (\mathbf{F}_r)_{jn} \end{aligned} \tag{A.32}$$

Also recalling (A.3d), we can write

$$\mathbf{B}_{pe}^{-T} = \mathbf{F}_r^{-T} \mathbf{C}_{VE} \mathbf{F}_r^{-1} \tag{A.33}$$

Now we express the relevant tensorial terms on the RHS of (A.30) in component forms as follows:

$$\begin{aligned}
&\left[\left\{\alpha_2\mathbf{C}_{VE}^{-1}+(\alpha_1-k)\mathbf{C}_r^{-1}\right\}\otimes\left(\frac{\partial\eta^{-1}}{\partial\mathbf{B}_{pe}}\frac{\partial\mathbf{B}_{pe}}{\partial\mathbf{C}_{VE}^{-1}}\right)\right]_{ijkl}\\
&=\left\{\alpha_2\mathbf{C}_{VE}^{-1}+(\alpha_1-k)\mathbf{C}_r^{-1}\right\}_{ij}\left(\frac{\partial\eta^{-1}}{\partial\mathbf{B}_{pe}}\frac{\partial\mathbf{B}_{pe}}{\partial\mathbf{C}_{VE}^{-1}}\right)_{kl}\\
&=\left[\alpha_2(\mathbf{C}_{VE}^{-1})_{ij}+(\alpha_1-k)(\mathbf{C}_r^{-1})_{ij}\right]\left[-\frac{\beta}{\eta^2}\left(\mathbf{B}_{pe}^{-T}\frac{\partial\mathbf{B}_{pe}}{\partial\mathbf{C}_{VE}^{-1}}\right)_{kl}\right]\\
&=-\frac{\beta}{\eta^2}\left[\alpha_2(\mathbf{C}_{VE}^{-1})_{ij}+(\alpha_1-k)(\mathbf{C}_r^{-1})_{ij}\right](\mathbf{C}_{VE})_{kl}
\end{aligned}\tag{A.34}$$

similarly,

$$\begin{aligned}
&\left[\mathbf{C}_{VE}^{-1}\otimes\left(\frac{\partial\alpha_2}{\partial\mathbf{B}_{pe}}\frac{\partial\mathbf{B}_{pe}}{\partial\mathbf{C}_{VE}^{-1}}\right)\right]_{ijkl}=(\mathbf{C}_{VE}^{-1})_{ij}\left(\frac{\partial\alpha_2}{\partial\mathbf{B}_{pe}}\frac{\partial\mathbf{B}_{pe}}{\partial\mathbf{C}_{VE}^{-1}}\right)_{kl}\\
&=(\mathbf{C}_{VE}^{-1})_{ij}\frac{1}{\sqrt{\mathrm{III}_{\mathbf{B}_{pe}}}}\left(\alpha-\frac{\mu}{2}\right)\left(\mathbf{B}_{pe}^{-T}\frac{\partial\mathbf{B}_{pe}}{\partial\mathbf{C}_{VE}^{-1}}\right)_{kl}\\
&=\frac{1}{\sqrt{\mathrm{III}_{\mathbf{B}_{pe}}}}\left(\alpha-\frac{\mu}{2}\right)(\mathbf{C}_{VE}^{-1})_{ij}(\mathbf{B}_{pe}^{-T})_{ab}\left(\frac{\partial\mathbf{B}_{pe}}{\partial\mathbf{C}_{VE}^{-1}}\right)_{abkl}\\
&=\frac{1}{\sqrt{\mathrm{III}_{\mathbf{B}_{pe}}}}\left(\alpha-\frac{\mu}{2}\right)(\mathbf{C}_{VE}^{-1})_{ij}(\mathbf{F}_r^{-T}\mathbf{C}_{VE}\mathbf{F}_r^{-1})_{ab}(\mathbf{F}_r)_{ak}(\mathbf{F}_r)_{bl}\\
&=\frac{1}{\sqrt{\mathrm{III}_{\mathbf{B}_{pe}}}}\left(\alpha-\frac{\mu}{2}\right)(\mathbf{C}_{VE}^{-1})_{ij}(\mathbf{C}_{VE})_{kl}
\end{aligned}\tag{A.35}$$

and

$$\begin{aligned}
&\left[\mathbf{C}_r^{-1}\otimes\left(\left(\frac{\partial\alpha_1}{\partial\mathbf{B}_{pe}}-\frac{\partial k}{\partial\mathbf{B}_{pe}}\right)\frac{\partial\mathbf{B}_{pe}}{\partial\mathbf{C}_{VE}^{-1}}\right)\right]_{ijkl}\\
&=(\mathbf{C}_r^{-1})_{ij}\left(\left(\frac{\partial\alpha_1}{\partial\mathbf{B}_{pe}}-\frac{\partial k}{\partial\mathbf{B}_{pe}}\right)\frac{\partial\mathbf{B}_{pe}}{\partial\mathbf{C}_{VE}^{-1}}\right)_{kl}\\
&=(\mathbf{C}_r^{-1})_{ij}\left[(\sigma-\omega)\left(\mathbf{B}_{pe}^{-T}\frac{\partial\mathbf{B}_{pe}}{\partial\mathbf{C}_{VE}^{-1}}\right)_{kl}-\left(\frac{\mu}{2\sqrt{\mathrm{III}_{\mathbf{B}_{pe}}}}+\gamma\right)\left(\mathbf{I}\frac{\partial\mathbf{B}_{pe}}{\partial\mathbf{C}_{VE}^{-1}}\right)_{kl}\right]\\
&=(\mathbf{C}_r^{-1})_{ij}\left[(\sigma-\omega)(\mathbf{F}_r^{-T}\mathbf{C}_{VE}\mathbf{F}_r^{-1})_{ab}(\mathbf{F}_r)_{ak}(\mathbf{F}_r)_{bl}-\left(\frac{\mu}{2\sqrt{\mathrm{III}_{\mathbf{B}_{pe}}}}+\gamma\right)\delta_{ab}(\mathbf{F}_r)_{ak}(\mathbf{F}_r)_{bl}\right]\\
&=(\mathbf{C}_r^{-1})_{ij}\left[(\sigma-\omega)(\mathbf{C}_{VE})_{kl}-\left(\frac{\mu}{2\sqrt{\mathrm{III}_{\mathbf{B}_{pe}}}}+r\right)(\mathbf{C}_r)_{kl}\right] \qquad \text{(A.36)}
\end{aligned}$$

Returning the component forms to corresponding direct notation, we have

$$\left\{\alpha_2\mathbf{C}_{VE}^{-1}+(\alpha_1-k)\mathbf{C}_r^{-1}\right\}\otimes\left(\frac{\partial\eta^{-1}}{\partial\mathbf{B}_{pe}}\frac{\partial\mathbf{B}_{pe}}{\partial\mathbf{C}_{VE}^{-1}}\right)=-\frac{\beta}{\eta^2}\left[\alpha_2\mathbf{C}_{VE}^{-1}+(\alpha_1-k)\mathbf{C}_r^{-1}\right]\otimes\mathbf{C}_{VE} \qquad \text{(A.37)}$$

$$\mathbf{C}_{VE}^{-1}\otimes\left(\frac{\partial\alpha_2}{\partial\mathbf{B}_{pe}}\frac{\partial\mathbf{B}_{pe}}{\partial\mathbf{C}_{VE}^{-1}}\right)=\frac{1}{\sqrt{\mathrm{III}_{\mathbf{B}_{pe}}}}\left(\alpha-\frac{\mu}{2}\right)\mathbf{C}_{VE}^{-1}\otimes\mathbf{C}_{VE} \qquad \text{(A.38)}$$

and

$$\begin{aligned}
&\mathbf{C}_r^{-1}\otimes\left(\left(\frac{\partial\alpha_1}{\partial\mathbf{B}_{pe}}-\frac{\partial k}{\partial\mathbf{B}_{pe}}\right)\frac{\partial\mathbf{B}_{pe}}{\partial\mathbf{C}_{VE}^{-1}}\right)\\
&\quad=\mathbf{C}_r^{-1}\otimes\left[(\sigma-\omega)\mathbf{C}_{VE}-\left(\frac{\mu}{2\sqrt{\mathrm{III}_{\mathbf{B}_{pe}}}}+\gamma\right)\mathbf{C}_r\right] \qquad \text{(A.39)}
\end{aligned}$$

Now substituting (A.37), (A.38) and (A.39) in (A.30) we have

$$\begin{aligned}
\frac{\partial \mathbf{R}}{\partial \mathbf{C}_{VE}^{-1}} = & \left(1+\frac{2\Delta t}{\eta}\alpha_2\right)\mathbf{I_4} + \frac{2\Delta t}{\eta}\Bigg[-\frac{\beta}{\eta}(\alpha_2\mathbf{C}_{VE}^{-1} + (\alpha_1 - k)\mathbf{C}_r^{-1}) \otimes \mathbf{C}_{VE} \\
& + \frac{1}{\sqrt{\mathrm{III}_{\mathbf{B}_{pe}}}}\left(\alpha - \frac{\mu}{2}\right)\mathbf{C}_{VE}^{-1} \otimes \mathbf{C}_{VE} + \mathbf{C}_r^{-1} \otimes \Bigg\{(\sigma-\omega)\mathbf{C}_{VE} \\
& - \left(\frac{\mu}{2\sqrt{\mathrm{III}_{\mathbf{B}_{pe}}}} + \gamma\right)\mathbf{C}_r\Bigg\}\Bigg] \\
= & \left(1+\frac{2\Delta t}{\eta}\alpha_2\right)\mathbf{I_4} + \underbrace{\frac{2\Delta t}{\eta}}_{\delta}\Bigg[\overbrace{\left\{\frac{1}{\sqrt{\mathrm{III}_{\mathbf{B}_{pe}}}}\left(\alpha - \frac{\mu}{2}\right) - \frac{\beta}{\eta}\alpha_2\right\}}^{\phi_1}\mathbf{C}_{VE}^{-1} \otimes \mathbf{C}_{VE} \\
& \underbrace{\left\{(\sigma-\omega) - \frac{\beta}{\eta}(\alpha_1 - k)\right\}}_{\phi_2}\mathbf{C}_r^{-1} \otimes \mathbf{C}_{VE} - \underbrace{\left\{\frac{\mu}{2\sqrt{\mathrm{III}_{\mathbf{B}_{pe}}}} + \gamma\right\}}_{\phi_3}\mathbf{C}_r^{-1} \otimes \mathbf{C}_r\Bigg] \\
= & (1+\delta\alpha_2)\mathbf{I_4} + \delta\Big[(\phi_1\mathbf{C}_{VE}^{-1} + \phi_2\mathbf{C}_r^{-1}) \otimes \mathbf{C}_{VE} - \phi_3\mathbf{C}_r^{-1} \otimes \mathbf{C}_r\Big] \qquad \text{(A.40)}
\end{aligned}$$

where,

$$\phi_1 = \frac{1}{\sqrt{\mathrm{III}_{\mathbf{B}_{pe}}}}\left(\alpha - \frac{\mu}{2}\right) - \frac{\beta}{\eta}\alpha_2 \qquad \text{(A.41a)}$$

$$\phi_2 = (\sigma - \omega) - \frac{\beta}{\eta}(\alpha_1 - k) \qquad \text{(A.41b)}$$

$$\phi_3 = \frac{\mu}{2\sqrt{\mathrm{III}_{\mathbf{B}_{pe}}}} + \gamma \qquad \text{(A.41c)}$$

and the residual expressed as

$$\mathbf{R} := \mathbf{C}_{VE}^{-1} - \left(\mathbf{C}_{VE}^{-1}\right)^t + \delta\left(\alpha_2\mathbf{C}_{VE}^{-1} + (\alpha_1 - k)\mathbf{C}_r^{-1}\right) \qquad \text{(A.42)}$$

b. Component Representations for the Jacobian and the Residual

The jacobian and the residual given by (A.40) and (A.42), respectively, can be expressed in terms of their cartesian components as follows:

$$\begin{aligned}\left(\frac{\partial \mathbf{R}}{\partial \mathbf{C}_{VE}^{-1}}\right)_{ijkl} &= (1+\delta\alpha_2)\delta_{ik}\delta_{jl}+\delta\big[(\phi_1(\mathbf{C}_{VE}^{-1})_{ij}+\phi_2(\mathbf{C}_r^{-1})_{ij}) \\ &\qquad (\mathbf{C}_{VE})_{kl}-\phi_3(\mathbf{C}_r^{-1})_{ij}(\mathbf{C}_r)_{kl}\big] \\ &= (1+\delta\alpha_2)\delta_{ik}\delta_{jl}+\delta\big[\phi_1(\mathbf{C}_{VE}^{-1})_{ij}(\mathbf{C}_{VE})_{kl} \\ &\qquad +(\mathbf{C}_r^{-1})_{ij}(\phi_2(\mathbf{C}_{VE})_{kl}-\phi_3(\mathbf{C}_r)_{kl})\big]\end{aligned} \tag{A.43}$$

$$\begin{aligned}\mathbf{R} &= (\mathbf{C}_{VE}^{-1})_{ij}-\left(\mathbf{C}_{VE}^{-1}\right)_{ij}^{t}+\delta\left(\alpha_2(\mathbf{C}_{VE}^{-1})_{ij}+(\alpha_1-k)(\mathbf{C}_r^{-1})_{ij}\right) \\ &= (1+\delta\alpha_2)(\mathbf{C}_{VE}^{-1})_{ij}-\left(\mathbf{C}_{VE}^{-1}\right)_{ij}^{t}+\delta(\alpha_1-k)(\mathbf{C}_r^{-1})_{ij}\end{aligned} \tag{A.44}$$

4. Verification of Finite Element Implementation

We now proceed to solve the same type of constrained compression problems as presented in Chapter III, Section C using the finite element implementation of the model in CAPA-3D. In finite elements, these problems have been solved by employing a 20-noded three dimensional solid element. The representative material element is constrained to move only in a normal direction (z-direction by convention here). A comparison is drawn between the solutions obtained from the analysis (with aid from the calculations from MATLAB) presented therein and the solutions obtained using the method of finite elements. The compressive strain applied here is 0.05. The material properties used are presented in Table I. Inputs to the model are given by linearly increasing the input to a constant value and then keeping the input at this value, removing the input is then, also, done by linearly decreasing from the maximum value to no-input. The comparison for the constant applied stress is presented in

Figure 8 and that for constant applied strain is presented in Figure 9. The calculated (using MATLAB) values of the stretch and stress in response to applied stress and strain respectively and the corresponding finite element solutions agree well, as can be observed from Figures 8 and 9. This serves as validation for the implementation of the model in CAPA-3D using the method of finite elements.

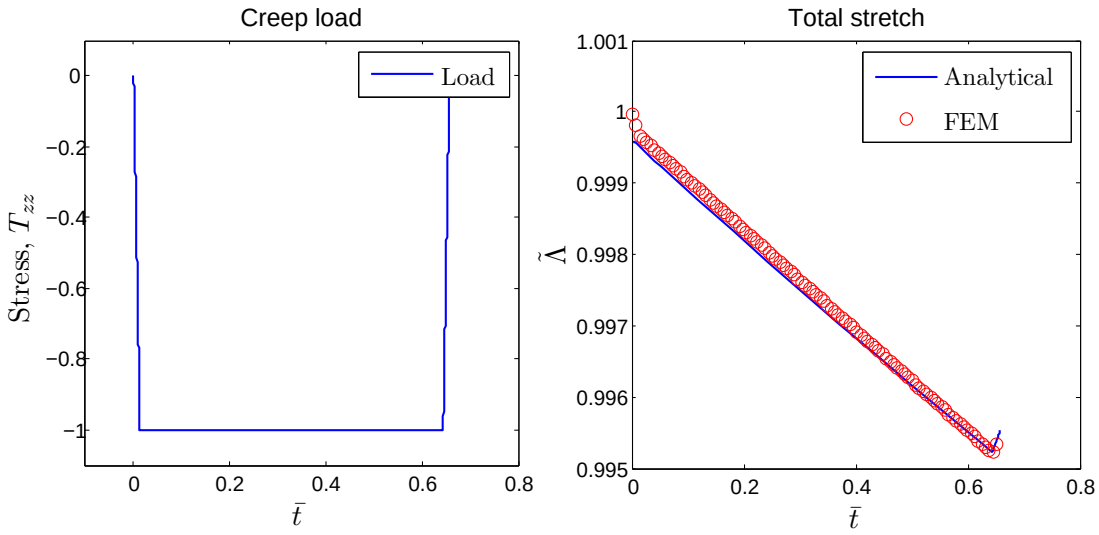

Fig. 8.: Finite element solution to the model response to applied constant stress

a. Constant Shear

The developed finite element implementation a constant shear rate problem is solved. The schematic representation for such a model is given in Figure 10. The unit cube is subject to a rate type shear deformation expressed by (A.45) and the boundary conditions to be applied to a unit cube are such that the cube is constrained to move

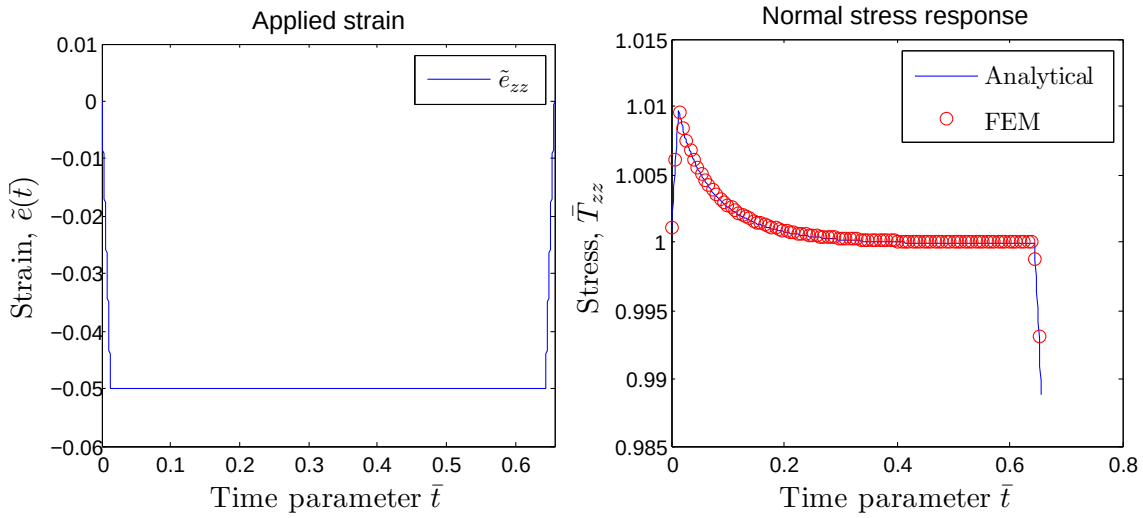

Fig. 9.: Finite element solution to the model response to applied constant strain (compressive 0.05)

only in a lateral direction indicating a shear deformation, see Figure 10.

$$[\mathbf{F}] = \begin{pmatrix} 0 & \gamma & 0 \\ 0 & 0 & 0 \\ 0 & 0 & 0 \end{pmatrix} \tag{A.45}$$

where, γ represents the shear rate of the deformation. T_{12} represents the shear in the xy-plane (see Figure 10), $T_{11} - T_{22}$ represents the first normal stress, and $T_{22} - T_{33}$ represents the second normal stress. We observe from Figures 11, 12, and 13 that material response corresponds with that of a non-linear material due to the exhibition of normal stress differences.

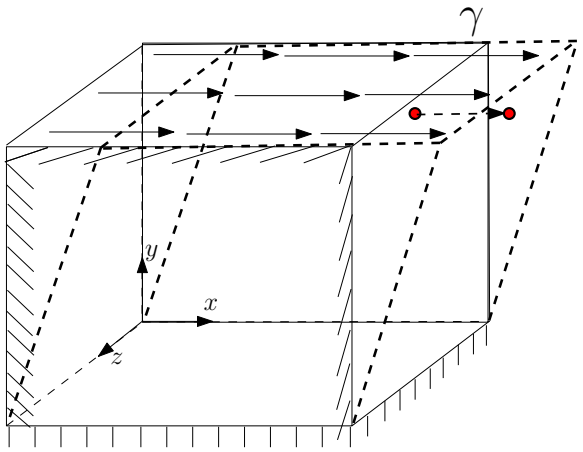

Fig. 10.: Schematic of the constant shear loading applied to a unit cube

b. Constant Shear Rate

Again, using the developed finite element implementation a constant shear rate problem is solved. The schematic representation for such a model is given in Figure 14. The unit cube is subject to a rate type shear deformation expressed by (A.46) and the boundary conditions to be applied to a unit cube are such that the cube is constrained to move only in a lateral direction indicating a shear deformation, see Figure 14.

$$[\mathbf{L}] = \begin{pmatrix} 0 & \kappa & 0 \\ 0 & 0 & 0 \\ 0 & 0 & 0 \end{pmatrix} \tag{A.46}$$

where, κ represents the shear rate of the deformation. T_{12} represents the shear in the xy-plane (see Figure 14), $T_{11} - T_{22}$ represents the first normal stress, and $T_{22} - T_{33}$ represents the second normal stress. We observe from Figures 15, 17, and 18 that material response corresponds with that of a non-linear material due to the exhibition of normal stress differences (though small in comparison with the shear stress T_{12}). It is to be noted that for the chosen set of parameters, model seems to exhibit near linear shear stress (T_{12}) versus shear rate characteristics. Such characteristics typically rep-

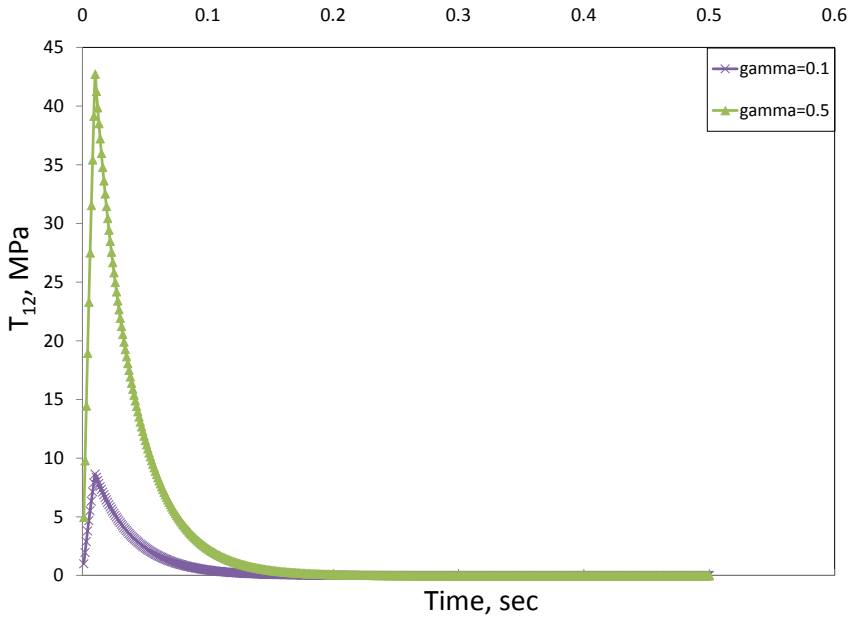

Fig. 11.: Shear stress (T_{12}) observed in response to constant shear loading

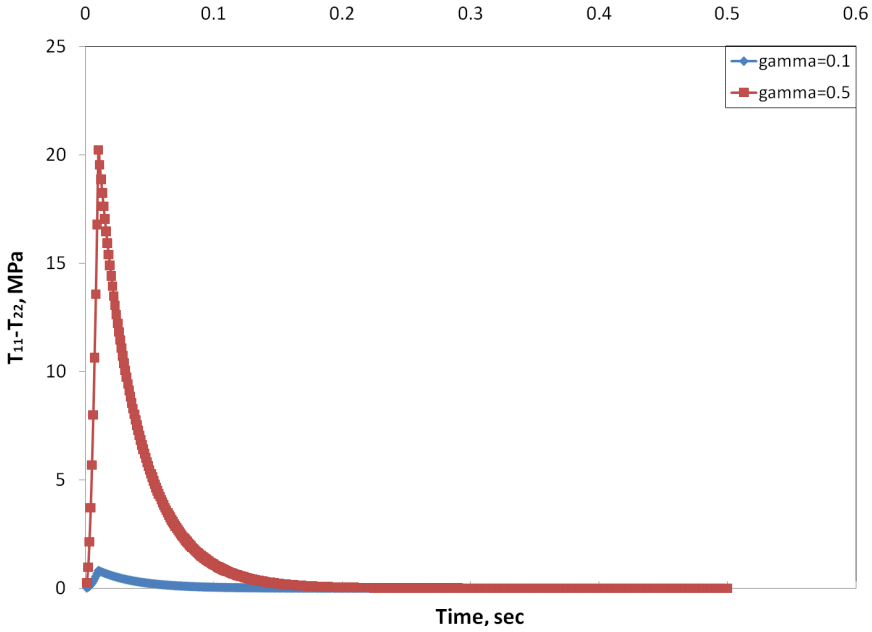

Fig. 12.: Comparison of the first normal stress ($T_{11} - T_{22}$) response to constant shear loading

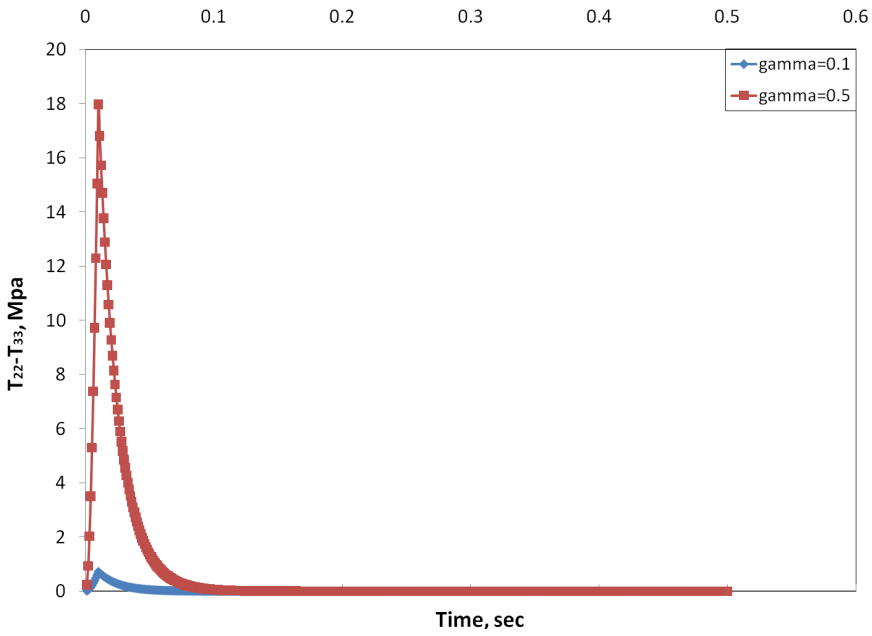

Fig. 13.: Comparison of the second normal stress ($T_{22} - T_{33}$) response to constant shear loading

resent the response due a fluid with the rate of dissipation similar to Newtonian fluid. However, the model does exhibit normal stress differences, a typical characteristic of non-Newtonian Fluids, as evidenced in Figures 17 and 18 and hence we observe that the model behaves like a non-Newtonian fluid and the choice of the parameters shall enhance the shear thickening nature of the model (unlike in Figure 16). This feature of the model is very useful for the purposes of modeling compaction in the laboratory or the field as the material in those situations undergoes shear thickening behavior. Our choice of model functions for μ and η ((B.3a) and (B.3b), respectively) ensure such a transition in the material's property.

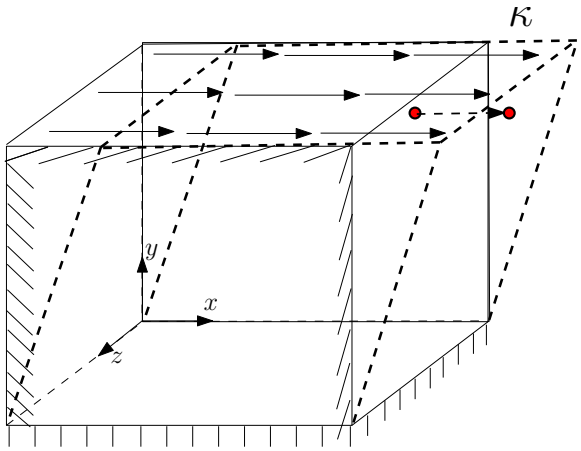

Fig. 14.: Schematic of constant shear rate applied to a unit cube

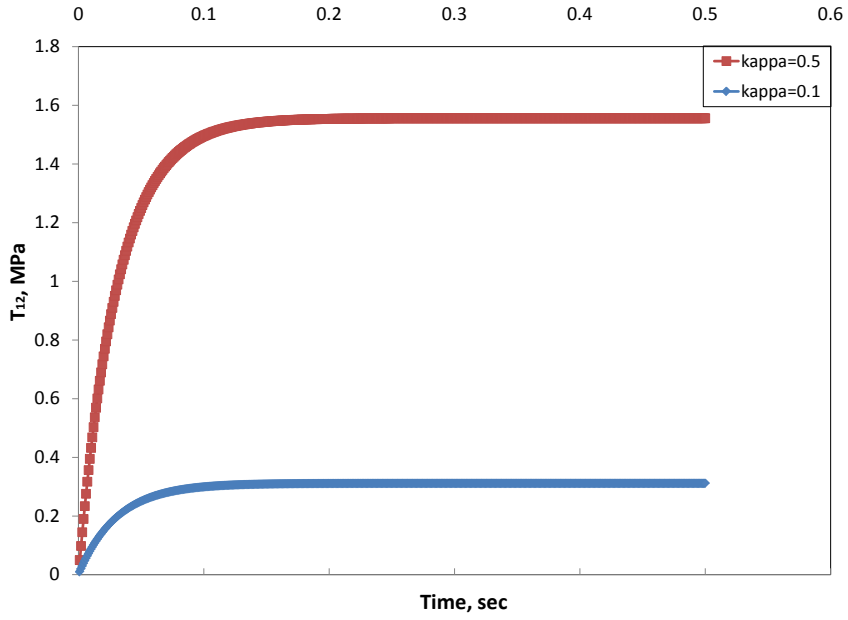

Fig. 15.: Shear stress (T_{12}) response to constant shear rate loading

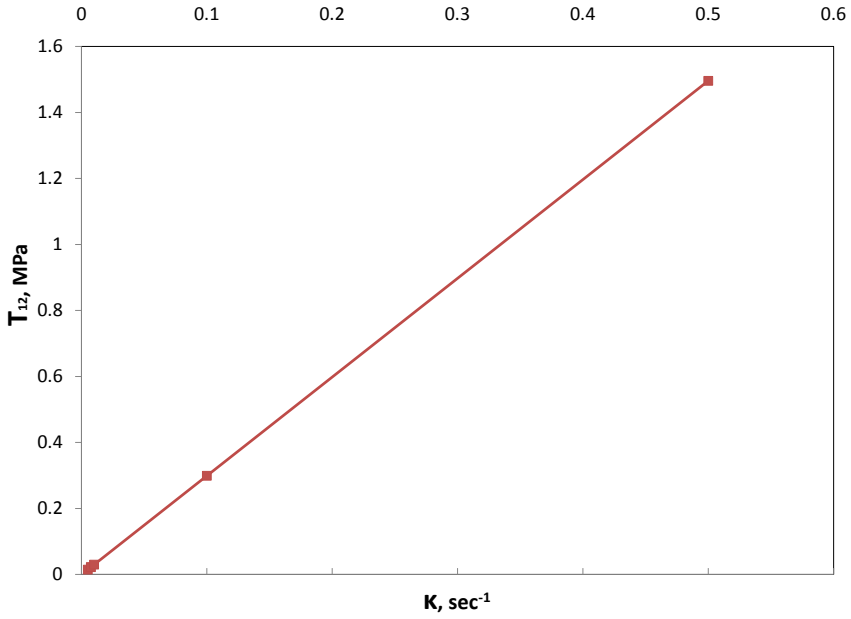

Fig. 16.: Shear stress (T_{12}) response due to different shear rates (using model parameters in Table I)

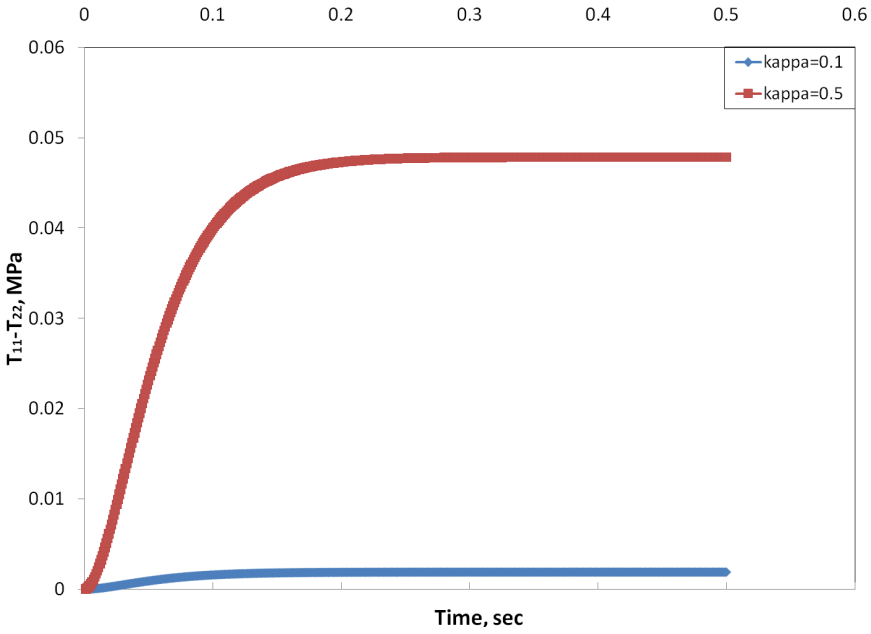

Fig. 17.: Comparison of the first normal stress ($T_{11} - T_{22}$) response to constant shear rate loading

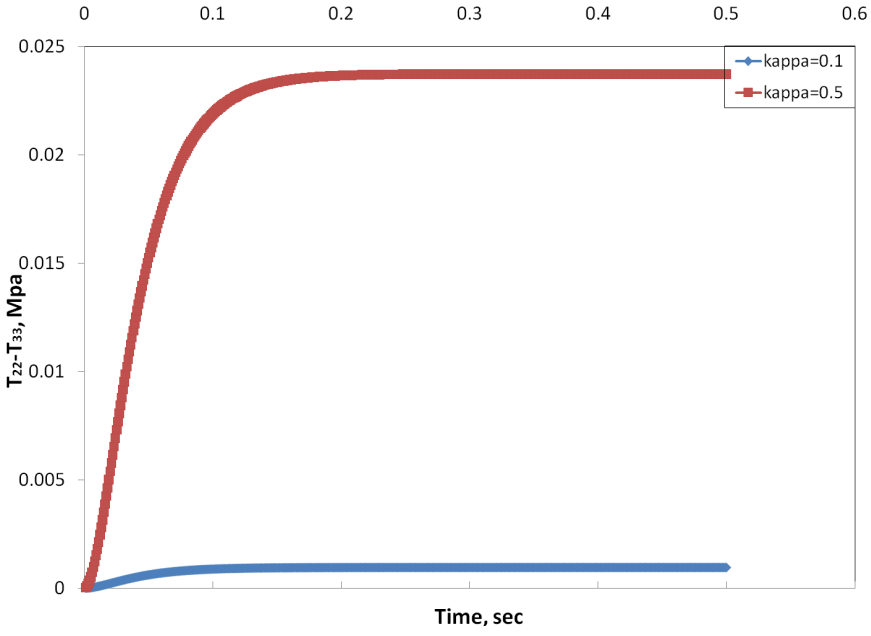

Fig. 18.: Comparison of the second normal stress ($T_{22} - T_{33}$) response to constant shear rate loading

CHAPTER V

SIMULATING COMPACTION IN A SUPERPAVE GYRATORY COMPACTOR

A. Relationships of Model Input Parameters to Material Properties

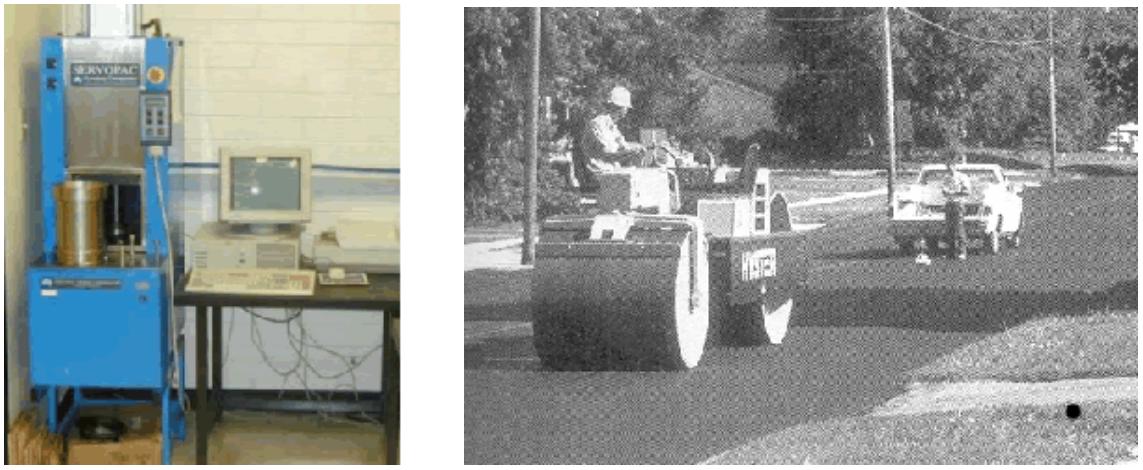

Fig. 19.: Compaction equipment: a) SUPERPAVE gyrator [2], b) Static steel roller

In the laboratory the compaction process (Figure 19) takes place at high temperatures. Some of the phenomena and parameters that are necessary for the model only occur or are relevant at higher temperatures. This fact makes it impossible to conduct conventional laboratory testing of specimens (e.g. triaxial testing) to obtain these parameters. This limitation will be overcome by implementing the mathematical model in finite elements and conducting simulations of the SGC compaction process and then fitting the finite element results to the available data in the form of SGC compaction curves to determine the model parameters. These parameters are then considered to include the information necessary to characterize material behavior under various conditions. Assuming that the material in the laboratory is representative of that in the field, the model parameters obtained from the SGC calibration can be used to simulate the field compaction (Figure 19), but under loading and boundary conditions

in the field. It is emphasized that this does not imply that the SGC process is to be assumed to be the same as the field compaction.

Once the model input parameters are identified, this work can be extended later to find correlations to material properties. It is expected that the model input parameters will be influenced by the following material properties:

- Aggregate gradation.
- Aggregate shape characteristics.
- Binder viscosity at compaction temperatures.
- Mixture temperature.

B. Model Verification and Calibration

Several studies that involved experimental characterization of the influence of different laboratory and field compaction procedures on the internal structure of asphalt mixtures and their mechanical properties have been previously conducted. From these studies, we have the following information and materials that can be used in verification and calibration:

- Pavement structure and layers.
- Equipment used in field compaction, (Screed, Dump truck, Roller): size, weight, pattern, sequence, number of passes etc.
- Number of passes of each compactor across the pavement width.
- Compaction data from the SGC.

- Mixture design and volumetrics.

Available data is used to determine the relationship between mixture properties, temperature and model parameters. The model parameters are determined by calibrating the finite element model to match the SGC compaction curves. This is followed by verification of the finite element implementation's prediction using a set of data that were not used in the model calibration. Field compaction measurements are used for further calibration and validation. Finite element models that simulate the loading and boundary conditions in the field are developed. The model parameters that were determined using the laboratory calibration will be used initially in the field finite element models. Then, any necessary calibration is introduced as needed to better simulate the field compaction. Such calibration is needed to account for the possible differences in materials between the laboratory and the field.

Thus, hereafter, the finite element implementation of the model developed is used to simulate the compaction processes and the simulated compactor response and changes in mixture stiffness at different stages of compaction are compared with the measured response and mixture stiffness[1].

The constitutive model developed is incorporated into two finite element programs (ABAQUS [8] and CAPA-3D). ABAQUS [8] is a commercial finite element package. The constitutive model was implemented in ABAQUS [8] through the UMAT material subroutine. The CAPA-3D general structure has been presented in detail by Scarpas ([56], [57]). For the implementation of the present model we are required to input into CAPA-3D two interface subroutines that provide the sys-

[1]Some of the results presented in this Chapter and in Chapter VII have been adopted from the paper [3] with kind permission from the Association of Asphalt Pavement Technologists (AAPT)

tem with the necessary model parameters and the algorithm for the required stress updates at each material point. The required equations are obtained through a numerical discretization of the material constitutive relations of the model to obtain a system of nonlinear algebraic equations at each material integration point, and from a choice of the solution technique for solving such a system. The computational sequences are then provided in the interface subroutines in the form of 'FORTRAN' code. Further details on the usage of the computational system are provided in the user manuals by Scarpas ([56], [57]).

The SGC is simulated through a lateral constraint along the boundary and a constant vertical stress of 600 kPa. In addition, sinusoidal vertical displacements that are 120° out-of-phase are applied at equidistant locations around the periphery of a plate supporting the mix from the bottom. This is done to simulate the applied angle of gyration in the SGC, which is responsible for inducing shear in the mix. The frequency of the applied gyrations is 30 gyrations per minute. The bottom support plate is modeled as a nearly rigid material. Also, a constant friction factor of 0.4 is introduced between the mixtures and the surrounding plates and mold.

The compaction curves obtained from the simulations are plotted as the normalized height of the specimen versus time of compaction. The normalized height is defined as the height of the specimen at any time divided by the initial height of the mixture in the SGC. Figure 20 shows an example of the finite element mesh of SGC.

C. Parametric Analysis of Model Parameters

A comprehensive parametric analysis was conducted in order to determine the sensitivity of the mixture compaction to the various model's parameters. The parameters that were used in this analysis are shown in Table II. All the SGC simulations were

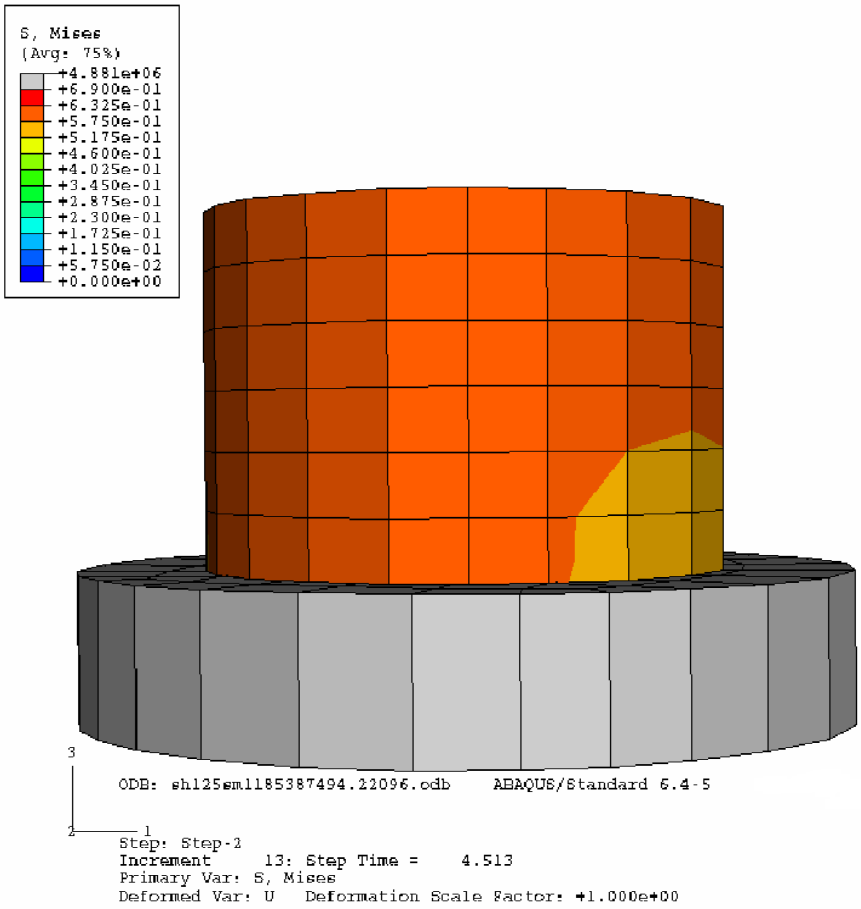

Fig. 20.: The finite element mesh used in modeling SGC

conducted using an angle of 1.25 ° .

An example of the influence of $\hat{\mu}$ is shown in Figure 21 keeping all other parameters the same. As expected, more compaction is achieved at a given time as $\hat{\mu}$ decreases. It is noted that the effect of this parameter on the compaction process becomes more important at longer compaction times when the mixture becomes more or less a highly viscous fluid. The analysis of parameter n_1 (Figure 22) showed that μ is significantly affected by the n_1 value, which controls the maximum compaction (change in height) of a mixture.

Analysis of the λ_1 parameter revealed that mixture compaction is affected very little, if any, by this parameter within the range of 0.2 and 0.3. This specific range for λ_1 is significant to obtain the initial viscous dissipation during the deformation. Therefore, it was decided to treat λ_1 as a constant, chosen to lie within this range, in the model in order to simplify obtaining the remaining model's parameters. Another parameter that was found to have very small effect on the compaction process is q_1 . Therefore, this parameter was also treated as a constant in the model.

Figure 23 shows that the parameter $\hat{\eta}$ controls the point at which the material behavior starts to change from a very low viscosity fluid-like behavior (rapid compaction) to solid a highly viscous fluid behavior (slow compaction). In Figure 23, the material with $\hat{\eta} = 1600$ MPa.s experiences change in the compaction rate prior to the other two materials. The parameter, λ_2 , presented in Figure 24, is directly related to the initial slope of the compaction curve (initial viscosity of the mixture). As shown in Figure 25, the model parameter q_2 contributes to the nonlinear change of viscosity from the start of the compaction process when the mixture exhibits low viscosity fluid-like behavior. The overall compaction of the mixture is higher at lower (more negative) values of q_2 . The parametric analysis showed that n_1 has almost no effect on the compaction curve, when it lies between 2 and 4 . Consequently, n_1 is

Table II.: Model parameters used in the parametric study

Set #	$\hat{\mu}$, (MPa)	λ_1	n_1	q_1	$\hat{\eta}$, (MPa.s)	λ_2	n_2	q_2
1	1700	0.22	4	-24	1400	0.25	3	-30
2	1900	0.22	4	-24	1400	0.25	3	-30
3	1500	0.22	4	-24	1400	0.25	3	-30
4	1700	0.25	4	-24	1400	0.25	3	-30
5	1700	0.20	4	-24	1400	0.25	3	-30
6	1700	0.22	5	-24	1400	0.25	3	-30
7	1700	0.22	3	-24	1400	0.25	3	-30
8	1700	0.22	4	-26	1400	0.25	3	-30
9	1700	0.22	4	-21	1400	0.25	3	-30
10	1700	0.22	4	-24	1600	0.25	3	-30
11	1700	0.22	4	-24	1300	0.25	3	-30
12	1700	0.22	4	-24	1400	0.26	3	-30
13	1700	0.22	4	-24	1400	0.22	3	-30
14	1700	0.22	4	-24	1400	0.25	4	-30
15	1700	0.22	4	-24	1400	0.25	2.5	-30
16	1700	0.22	4	-24	1400	0.25	3	-26
17	1700	0.22	4	-24	1400	0.25	3	-34

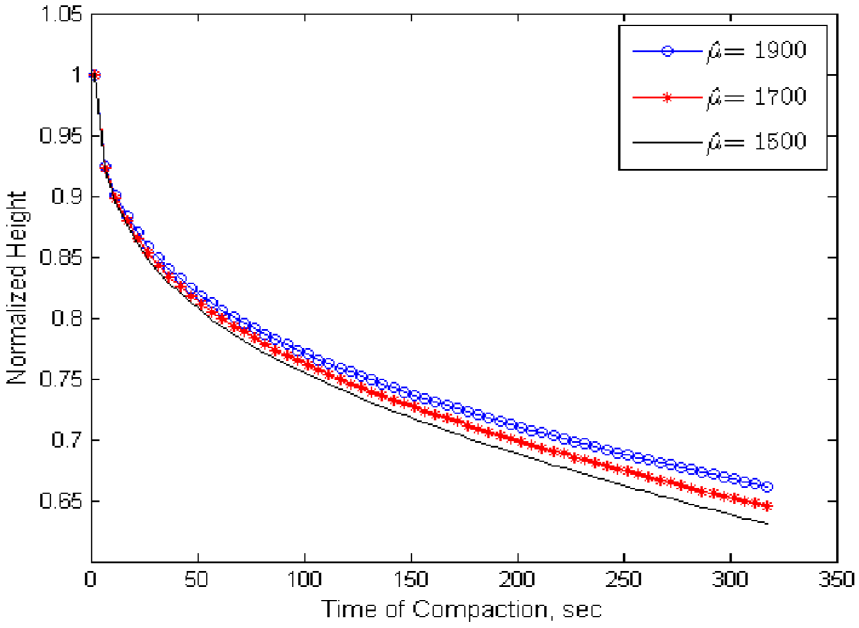

Fig. 21.: Analysis of the sensitivity of compaction to $\hat{\mu}$

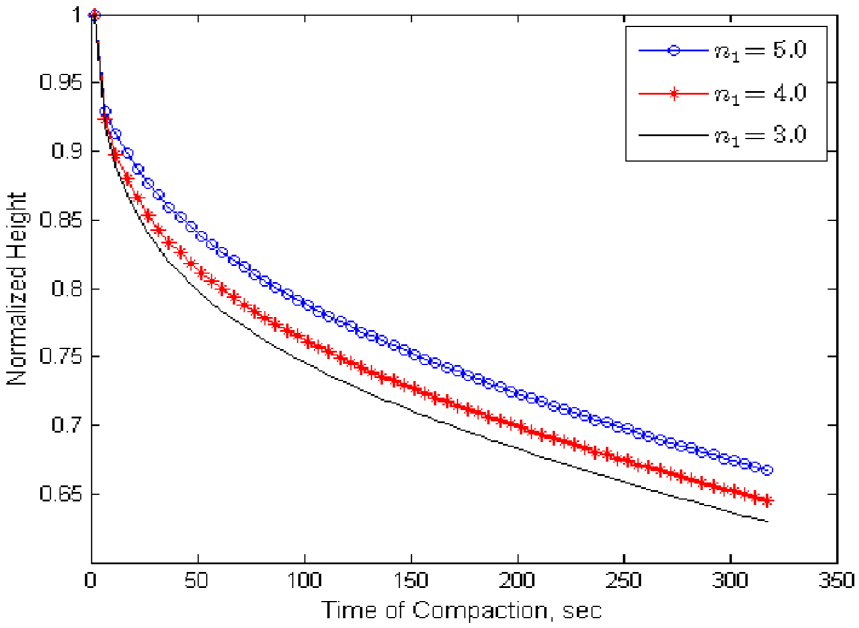

Fig. 22.: Analysis of the sensitivity of compaction to n_1

assumed to be a constant within this range, for SGC simulations presented in this chapter.

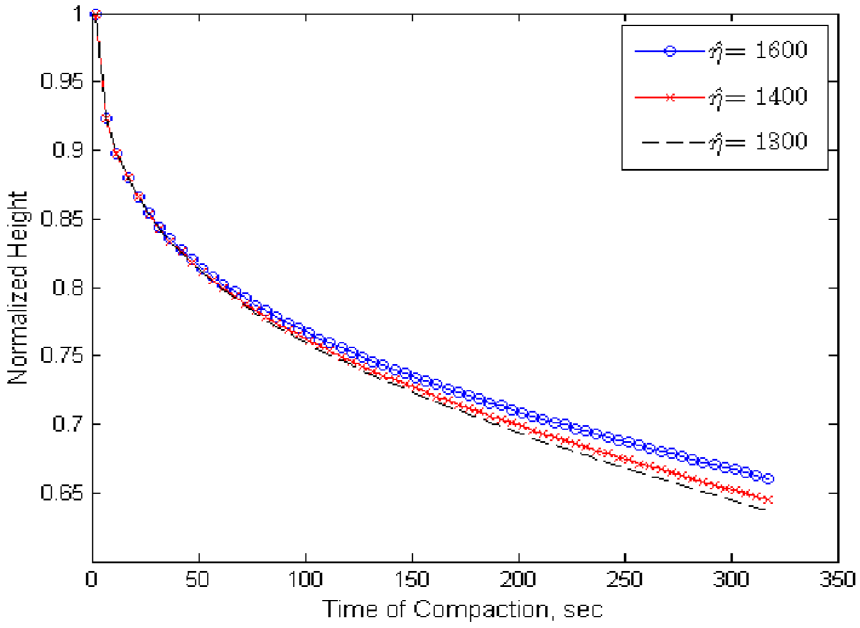

Fig. 23.: Analysis of the sensitivity of compaction to $\hat{\eta}$

The equations for shear modulus-like function μ and viscosity-like function η are represented as in equations (C.1) and (C.2), respectively, after assigning constant values to λ_1 , q_1 , and n_2 .

$$\mu = \hat{\mu}(1 + 0.25(III_G)^{2n_1})^{-25} \tag{C.1}$$

$$\eta = \hat{\eta}(1 + \lambda_2(III_G)^5)^{q_2} \tag{C.2}$$

The viscosity function primarily controls the initial compaction when the material behaves like a fluid with very low viscosity. The change in viscosity during compaction is associated with changes in the reduction in asphalt film thickness leading to an increase in the overall viscosity of the mixture. On the other hand, the

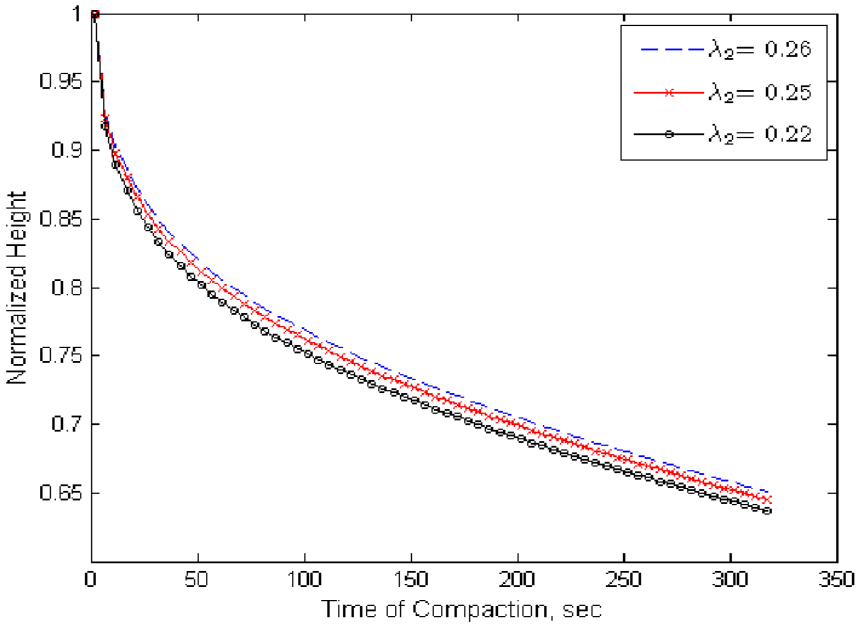

Fig. 24.: Analysis of the sensitivity of compaction to λ_2

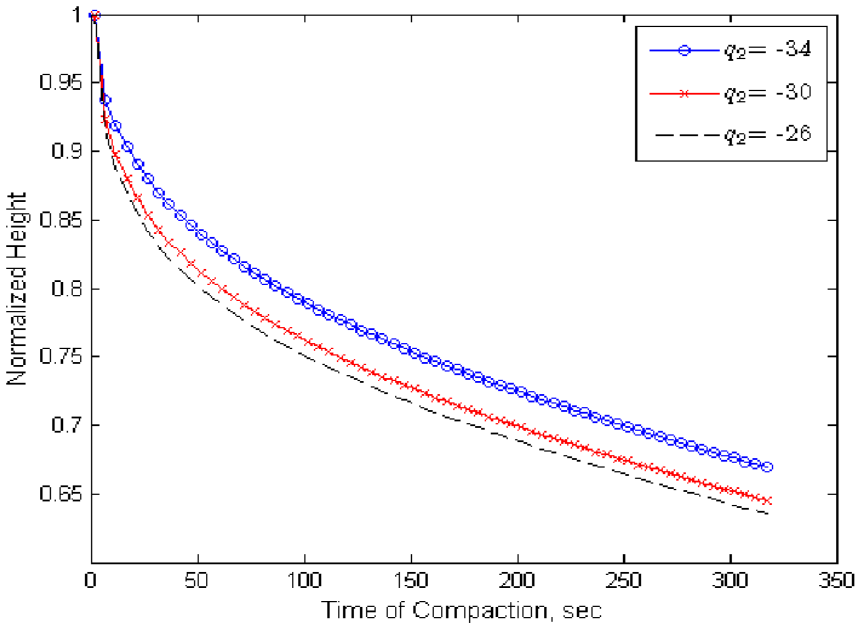

Fig. 25.: Analysis of the sensitivity of compaction to q_2

shear modulus function primarily controls the compaction process after some time of compaction when the material starts to behave like a highly viscous fluid. The increase in the shear modulus is associated with changes in the aggregate structure due to the development of more contacts and interlocking.

Based on the parametric analysis and the physical significance of the model's parameters, we present here a summary of these parameters:

1. $\hat{\mu}$: shear modulus parameter, marks the point at which the mixture starts to behave as a highly viscous fluid and the shear modulus dominate the compaction process.

2. n_1 : shear modulus parameter, affects the rate of compaction after the mixture starts to behave as a high viscosity fluid.

3. $\hat{\eta}$: viscosity parameter, controls the point at which the material behavior starts to change from a low viscosity fluid behavior (rapid compaction) to a highly viscous fluid behavior (slow compaction).

4. λ_2 : viscosity parameter, controls the initial slope of the compaction curve (initial viscosity of the mixture).

5. q_2 : viscosity parameter, contributes to the nonlinear change of viscosity.

The relationship between the model's parameters and the compaction process is illustrated in Figure 26.

1. Sensitivity of Compaction to Angle of Gyration

Figure 27 presents the results of finite element simulations of the SGC at different angles of gyrations. It is clear that the model captures the influence of the angle on

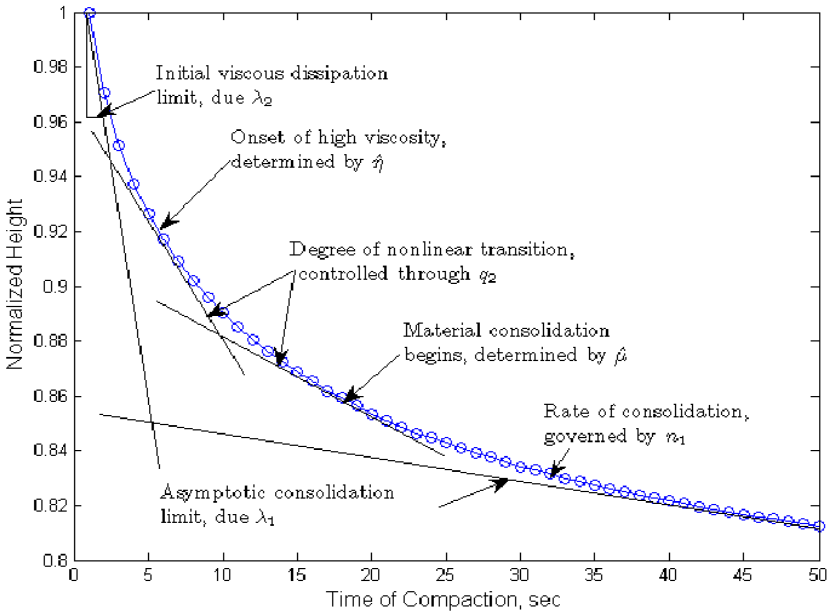

Fig. 26.: Illustration of the relationship of the model's parameters to the compaction process

the change in compaction. It is also to be noted that the compaction behavior does not change in a linear manner with the change in angle.

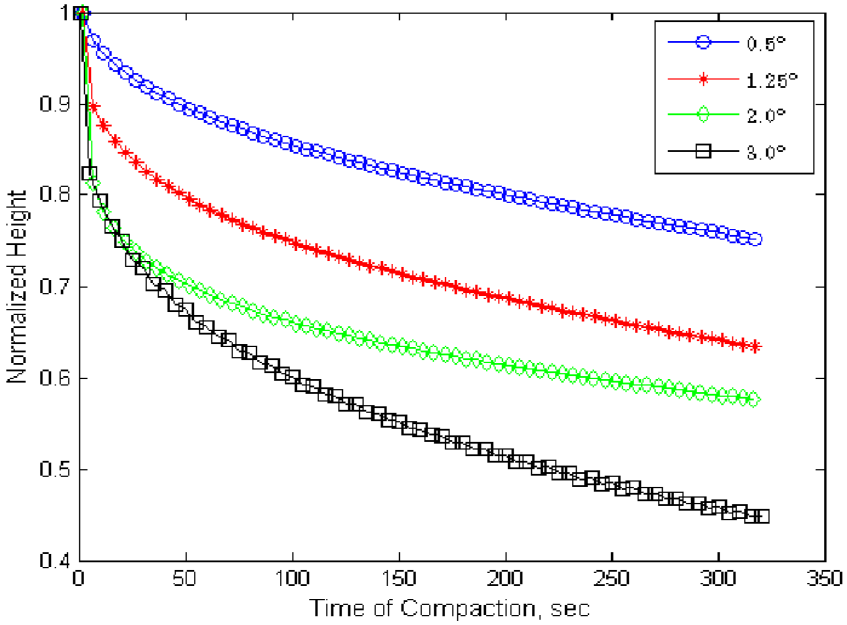

Fig. 27.: Influence of angle of gyration on the compaction curve

The finite element model was used to determine the maximum shear stresses at the top of the specimens for angles of gyration of 1.25° and 2.0° (Figure 28 , and Figure 29). The analysis was conducted using the model's parameters determined for SH36 mixture presented later in this paper. Initially, the shear stress decreases rapidly when the material behaves as a compressible fluid, and then starts to increase gradually as the mixture starts to behave as alike a highly viscous fluid. It is observed that the shear stresses are higher for higher angles of compaction. This is attributed to the fact that an increase in angle of gyration is associated with an increase in the applied shear stresses. It is also noted that the point at which shear stress starts to increase occurs earlier at 2.0° angle than at 1.25° angle. This can be explained by the fact that the mixture compacts and gains strength faster at 2 ° angle of gyration.

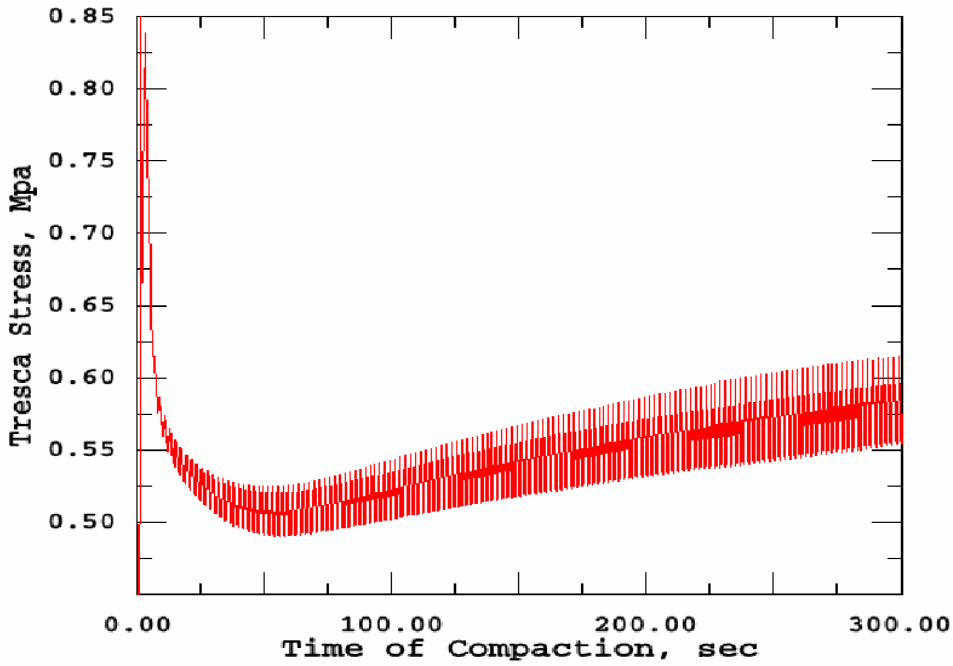

Fig. 28.: Maximum shear stress at the top of the specimen for a gyration angle of 1.25°

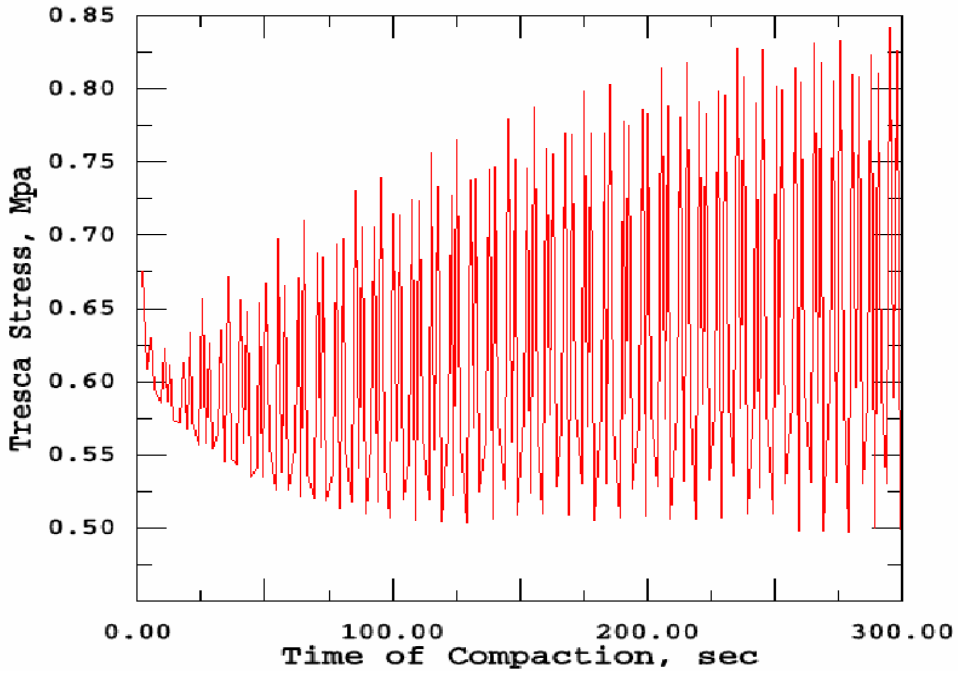

Fig. 29.: Maximum shear stress at the top of the specimen for a gyration angle of 2.0°

D. Model Calibration and Verification

Mixtures from various projects where compacted using two angles of gyration of 1.25 ° and 2.0 ° , noted to correspond most to the field compaction and hence these angles of gyration interest us. The compaction curves at an angle of 1.25 ° were used to determine the model's parameters, while the curves for an angle of 2.0 ° were used to verify the ability of the model to fit experimental measurements different than those used to determine the parameters. Each of the compaction curves was divided into three parts: time of compaction less than 15 seconds, time of compaction between 15 and 30 seconds, and time of compaction higher than 30 seconds. The first part was used to estimate the parameters λ_2 and $\hat{\eta}$ of the viscosity function, the second part was used to estimate q_2 , while the third part was used to determine the parameters $\hat{\mu}$ and n_1 of the modulus function. The initial estimates from these parts were then slightly adjusted to minimize the difference between the model's results and the data of the whole compaction curve. The final simulation results using the parameters in Table III are shown in Figures 30 to 34 for an angle of 1.25 ° and in Figures 35 to 39 for an angle of 2.0 ° . The results show that the model has reasonable representation of the compaction curves at both angles. The non-smooth response characteristics of the simulation, as can be observed from the plot, are a natural consequence of the boundary conditions and the fact that the calculations are made at an integration point in the material mesh that is at a slight eccentric position from the axis of symmetry of the model.

The comparison between the parameters in Table III and mixture characteristics did not reveal clear and simple relationships. This could be attributed to the fact that each of the parameters, whether part of the modulus or viscosity functions, is related to combinations of the mixture characteristics. The determinations of these

relationships require the analysis of parameters of more mixtures in order to develop regression equations between model's parameters and mixture characteristics. Nevertheless, there are some trends supporting that relationships exist between material properties and model parameters. For example, the lowest values of $\hat{\eta}$ and $\hat{\mu}$ are found to be for the SMA (stone matrix asphalt) mixture in IH35. These low values suggest better compactability which could be attributed to the high asphalt content of this mixture. For completeness we note here that the model results for very low angles of compaction do not agree well with what can be observed in the laboratory at such angles. This is owing to the high compressibility built into the model to simulate the large deformations generally observed during compaction, which necessarily is not exhibited by actual mixes at very low angles of gyration.

Table III.: Model parameters obtained from compaction data

Mix Projects	$\hat{\mu}$, MPa	n_1	$\hat{\eta}$, MPa.s	λ_2	q_2
IH35	2000	5	1400	0.25	-27
SH36	2400	4	1800	0.22	-28
US87	2600	5	2100	0.26	-27
US259	2400	5	1700	0.21	-28
SH21	2500	4	2000	0.22	-30

E. Summary

The parametric analysis conducted in this study showed that the compaction process is insensitive to changes in some of the model's parameters. Therefore, it was decided to use constant values for these parameters during all the finite element simulations in order to simplify the process of finding the values of the remaining parameters. The

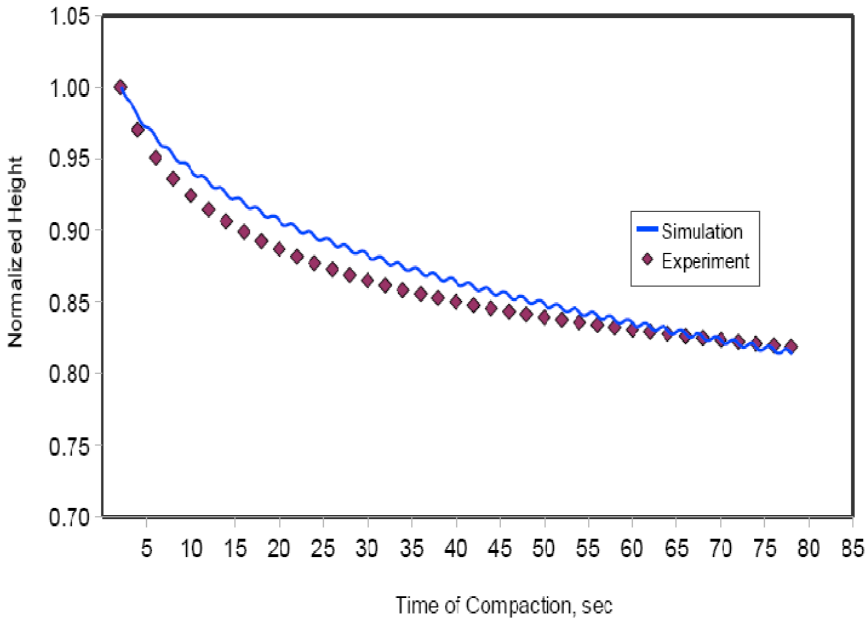

Fig. 30.: Fitting of the compaction data at 1.25 ° for project IH35

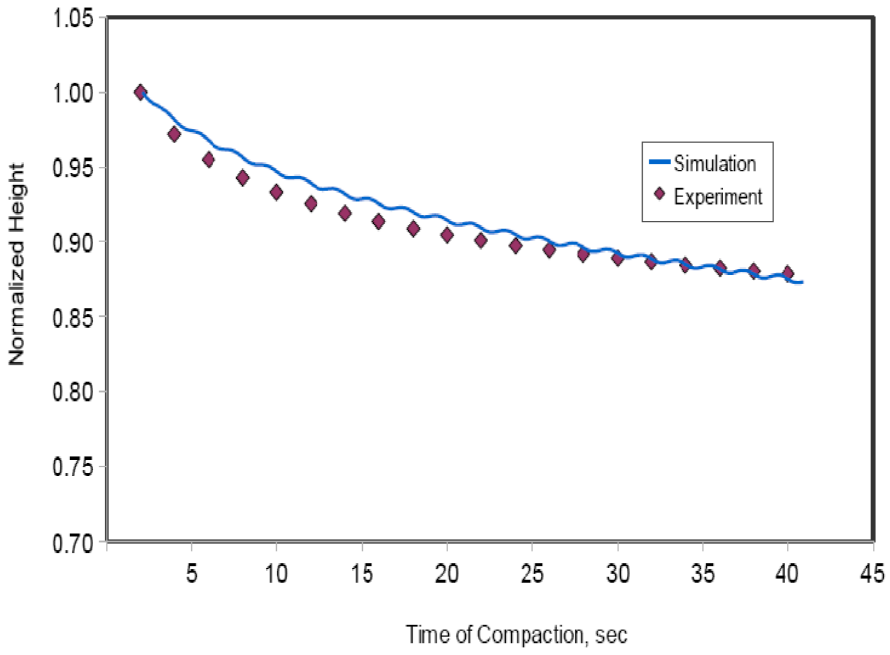

Fig. 31.: Fitting of the compaction data at 1.25 ° for project US259

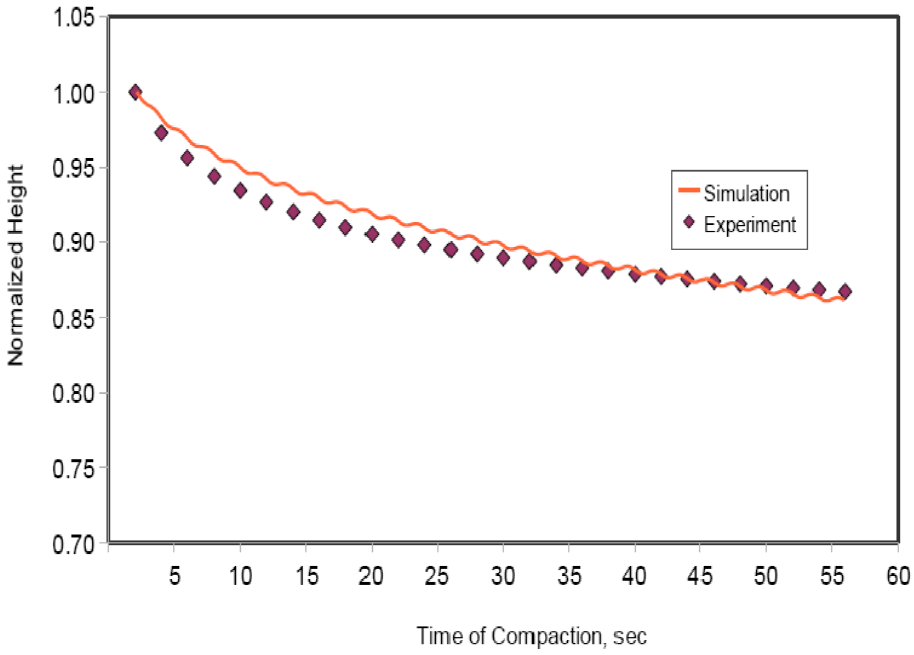

Fig. 32.: Fitting of the compaction data at 1.25 ° for project SH36

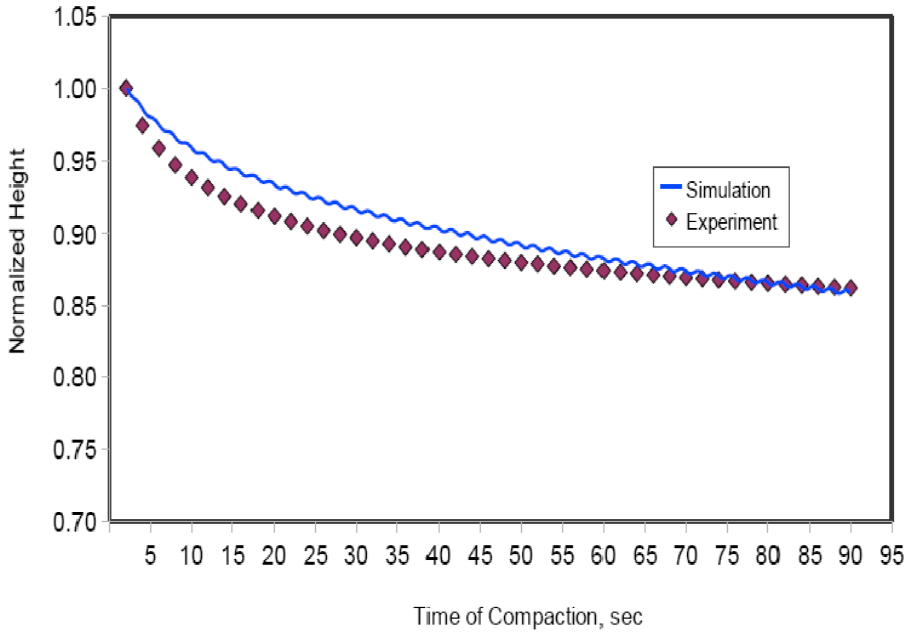

Fig. 33.: Fitting of the compaction data at 1.25 ° for project SH21

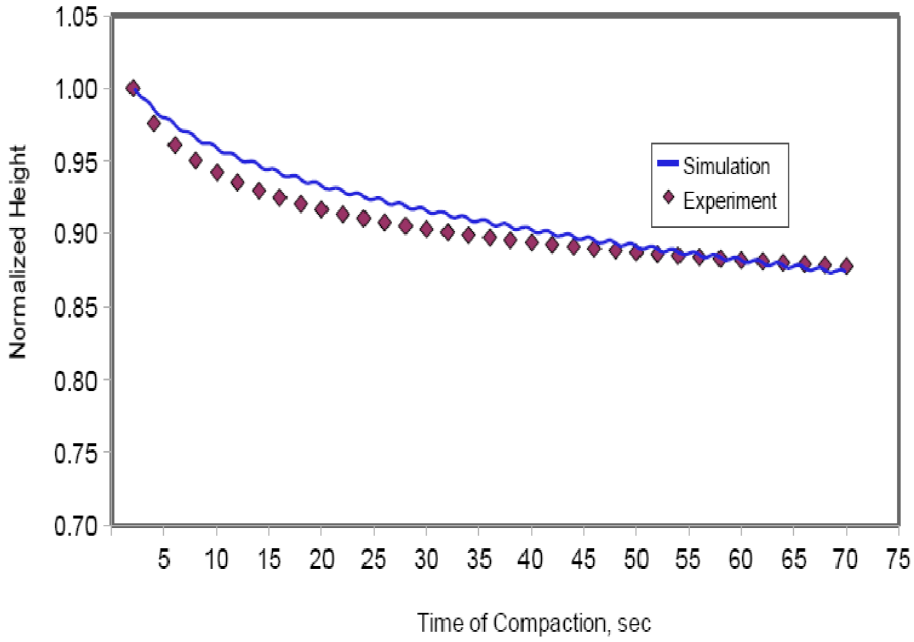

Fig. 34.: Fitting of the compaction data at 1.25 ° for project US87

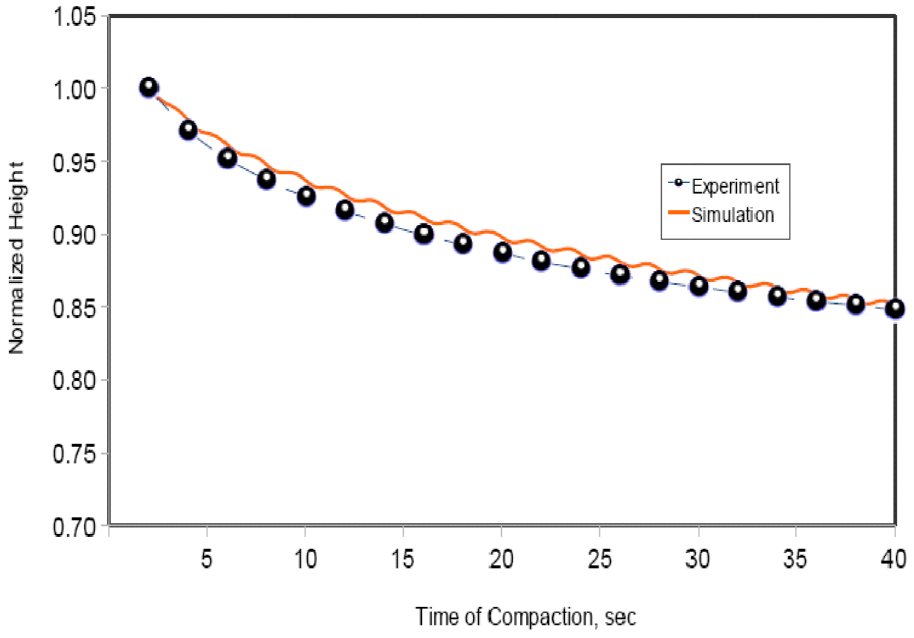

Fig. 35.: Prediction of the compaction data at 2.0 ° for project IH35

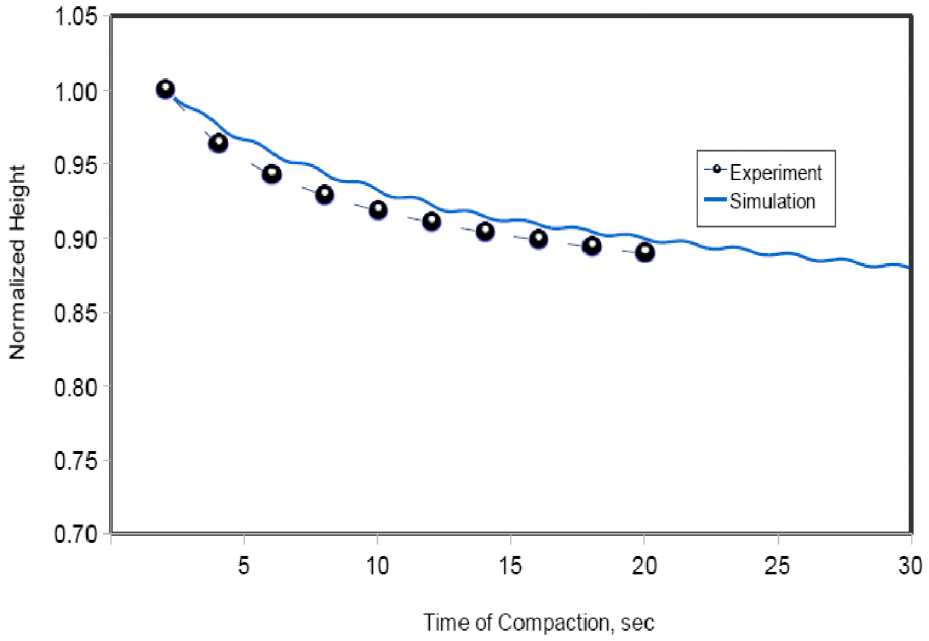

Fig. 36.: Prediction of the compaction data at 2.0 ° for project US259

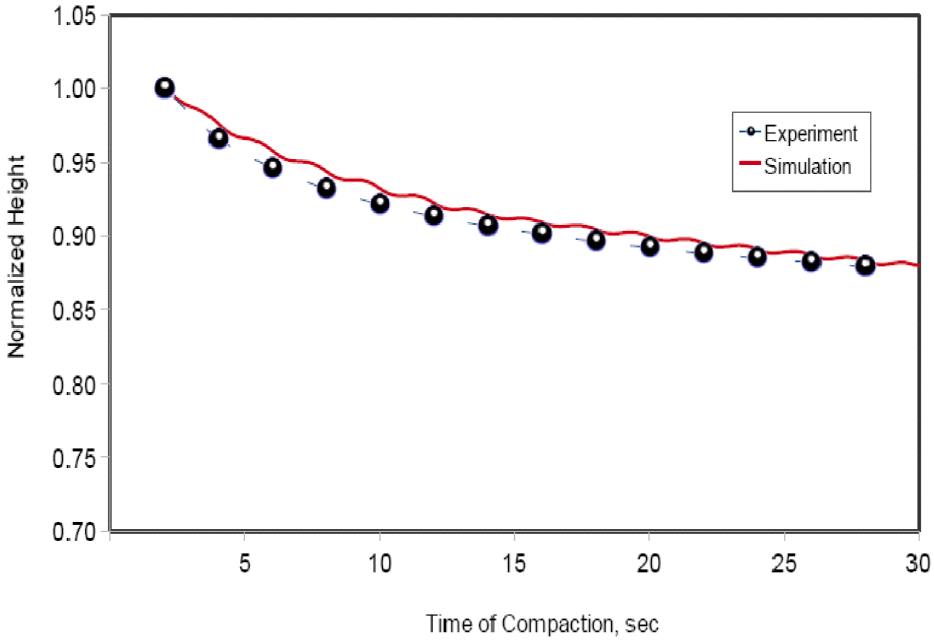

Fig. 37.: Prediction of the compaction data at 2.0 ° for project SH36

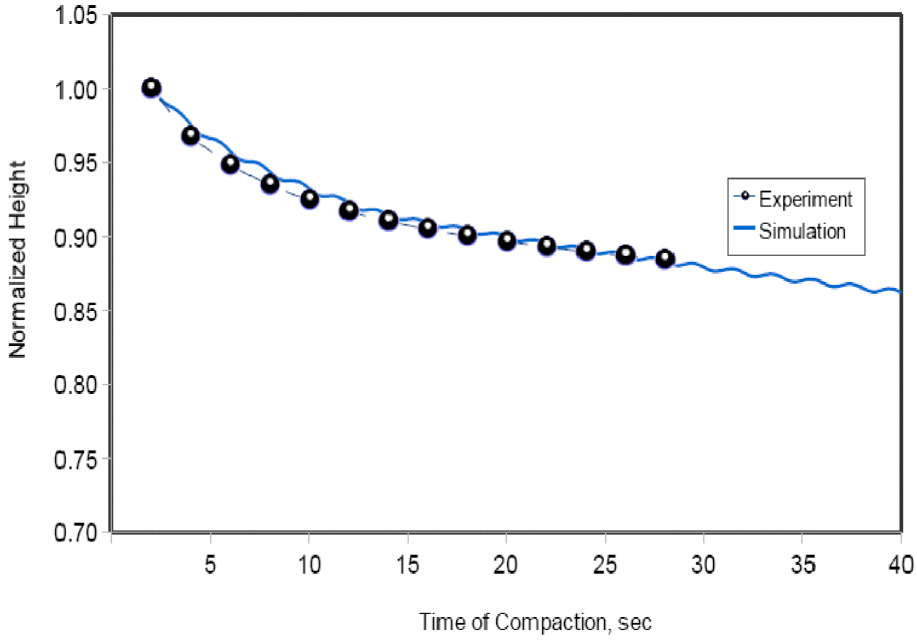

Fig. 38.: Prediction of the compaction data at 2.0 ° for project SH21

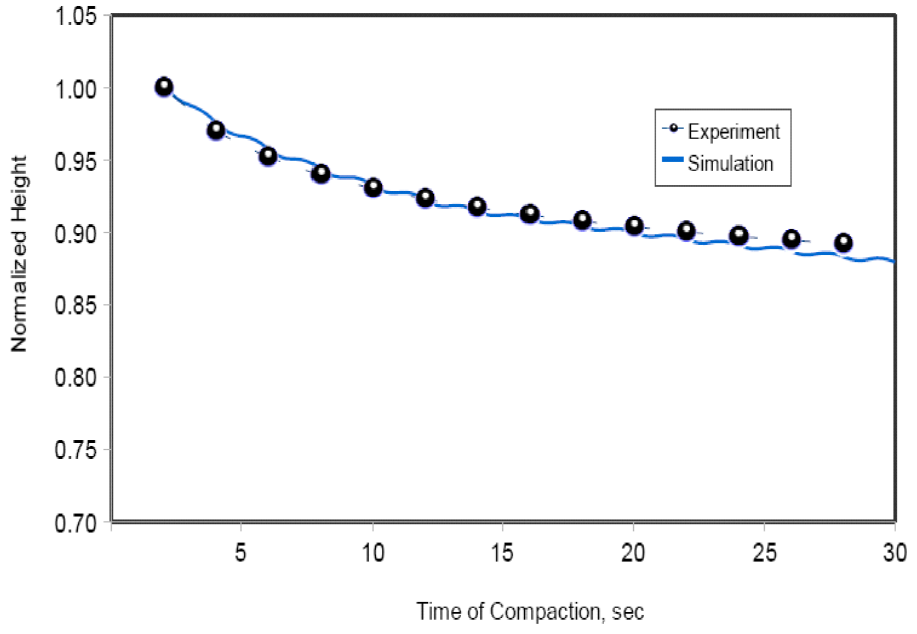

Fig. 39.: Prediction of the compaction data at 2.0 ° for project US87

parametric analysis demonstrated that some of the model's parameters are related mostly to the initial stage of compaction when the material exhibits low viscosity fluid-like behavior, while some parameters are related to the behavior of the mixture after it starts to exhibit a highly viscous fluid behavior and compaction rate decreases. A systematic method was developed to determine the model's parameters from the Superpave gyratory compaction curves. It was necessary to develop this method owing to the difficulty of conducting conventional tests (e.g. triaxial or shear tests) to determine the model's parameters given the high compaction temperatures. The finite element simulations demonstrated the capability of the constitutive model to simulate the Superpave gyratory compaction process at different compaction angles.

CHAPTER VI

FINITE ELEMENT MODEL FOR FIELD COMPACTION

A. Introduction

Development of a useful simulation environment to study field compaction of hot mix asphalt (HMA) provides a unique challenge owing to the complex physical interactions involved. For this purpose a framework is chosen comprising of a nonlinear material model coupled with an advanced numerical simulation environment (CAPA-3D). The theoretical material model employed for the finite element model development has been presented earlier Chapter III. This model is subsequently utilized for the simulation of the compaction mechanism of the SUPERPAVE Gyratory Compactor (SGC). The results of such a study have been documented in Chapter V. Herein the chosen numerical framework is used to extend the work presented in Chapters III, IV and V to specifically study the material model's behavior when subject to the conditions pertinent to field compaction of HMA.

The simulation of the rolling compaction process includes many challenges in terms of representing the complex physical interactions in a numerical model. Some of the chief factors that influence the simulation of the field compaction simulation are as follows:

1. Development of an algorithm for determining contact area between rolling drum and pavement surface. This feature will be useful in determining the effective area of a given finite element mesh that needs to be in contact with a roller applying compacting load on the material. As the material model chosen (Chapter III) is a compressible viscoelastic material, one needs to be careful in devising an algorithm for contact owing to the large deformations that re-

sult. The exact mechanics to establish a rolling-type contact between the roller and the nonlinear pavement material require in-depth exploration of the field of nonlinear contact mechanics and is out of scope of this study.

2. Owing to the large variation in the properties of the material for the different layers of a pavement structure, specialized techniques are required to model the interactions among the layers. For this purpose we employ specialized interfacial finite elements for resolving the interfacial contact issues.

3. Dampening of dynamic effects due to the moving load. Due to the application of a load that is translated over the surface in field compaction, special care, if necessary, should be taken to avoid wave reflections from boundary and interfaces. Such interference waves produced within the material can affect the solution in a numerical experiment such as that currently undertaken. A standard technique to effectively deal with such detrimental effects in numerical simulations is the use of 'impedance layers' in finite element meshes (see Sluys [58] for further details on the utility and development of such elements).

4. Effect of the stiffness of substructure layers needs to be studied, as the 'structural' response of the pavement material is, in general, influenced by the substructural material.

5. A study of the sensitivity of compaction to model parameters provides us with an understanding of the behavior of the model in a structural setting. The change in behavior of the finite element model with changes in parameter values provides an estimation of the model behavior to the input conditions. Due to the physical interactions involved and lack of detailed experimental data, such a study provides insight to enable drawing correlations between laboratory and

field compaction activities.

B. Finite Element Model for Field Compaction

A typical pavement structure that is to be employed for simulating field compaction is represented by Figure 40. It consists of three layers: a base layer consisting of aggregate and/or soil, of approximately 18 in. thickness; an overlay on top of the base layer consisting of old HMA, approximately 2 in. thick and a top layer of 3 in. of a new HMA layer that is to be compacted by rolling.

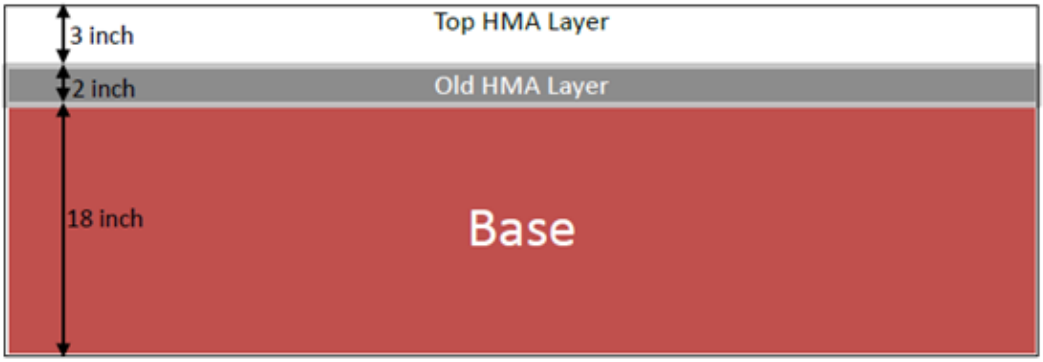

Fig. 40.: Pavement structure that is typical employed for studying field compaction

The general structure of finite element computational system, CAPA-3D, facilitates quick and flexible testing of material models and has been presented in detail in Scarpas [56] and Scarpas [57]. For the implementation of the chosen material model two interface subroutines defining material behavior are input into CAPA-3D. The necessary model parameters, boundary conditions and the algorithmic logic necessary for the required stress updates at each material point are provided to CAPA-3D through user interface files for each type of necessary data. The required stress update subroutine has been devised from the equations obtained through a numerical discretization of the constitutive relations of the material model. The stress update

subroutine consists of a system of nonlinear algebraic equations that are to be iteratively integrated at each material integration point and for each step in the time domain. The computational sequences thus devised are then provided as 'FORTRAN' instructions that can be embedded directly into the CAPA-3D interface. Details on the usage of the computational system are provided in Scarpas [56].

Some of the important characteristics of the finite element mesh (Figure 41) used for simulating compaction are:

1. Representative mesh for materials in the three primary layers along with the material already compacted by the roller. The mesh is a half sectional view due to symmetry of boundary conditions which allows for the half mesh to be employed instead of the full mesh.

2. The typical geometry of the mesh is given the typical thicknesses in Figure 40, a lane width of 12 ft and the total length of the top layer in the direction of rolling being 44 inch. The top layer consists of a newly laid mix and a previous compacted mix each of length 22 inch in the direction of rolling.

3. The typical material properties to be used for the three layers are given in Table IV.

4. All the finite elements used for the structural layers are 20-noded, solid, three dimensional continuum elements. Details of other choices and options with regard to the elements available for use in CAPA-3D are available in Scarpas [56].

5. The interfacial contact between a pair of layers among the un-compacted HMA, the old HMA layer underneath and the previously compacted layer on top is resolved through use of a special interface element available in CAPA-3D

(Scarpas [56]). Use of this layer is to strictly preserve the contact between the layers and hence these special elements do not have any structural utility.

6. Impedance layers, surrounding the base layer and other such elements surrounding the top hot mix asphalt (HMA) and old HMA layers (as shown in Figure 41). These elements minimize the dynamic effects discussed earlier.

7. The analyses are performed by fixing the time increment at 0.05 sec. This value is arrived at based on the actual velocity of the roller and taking into account a need for consistent numerical stability of the algorithm. The time increments are calculated by first determining the total time per pass by dividing the total distance of travel (22 inch) by the speed of travel of the roller (initially set to 4.4 inch/sec). And then multiplying by the total number of time steps desired per pass (assumed 100 here).

Table IV.: Typical material properties of pavement structural layers

Layer	Model	Thickness	Properties
New compacted asphalt layer	Compressible non-linear viscoelastic	Initial = 3 inches; Changes during compaction	Presented as parameter sets later in this chapter
Old asphalt mix layer	Elastic	2 inches	E = 300 ksi; ν= 0.35
Base layer	Elastic	18 inches	E = 145 ksi; ν= 0.20

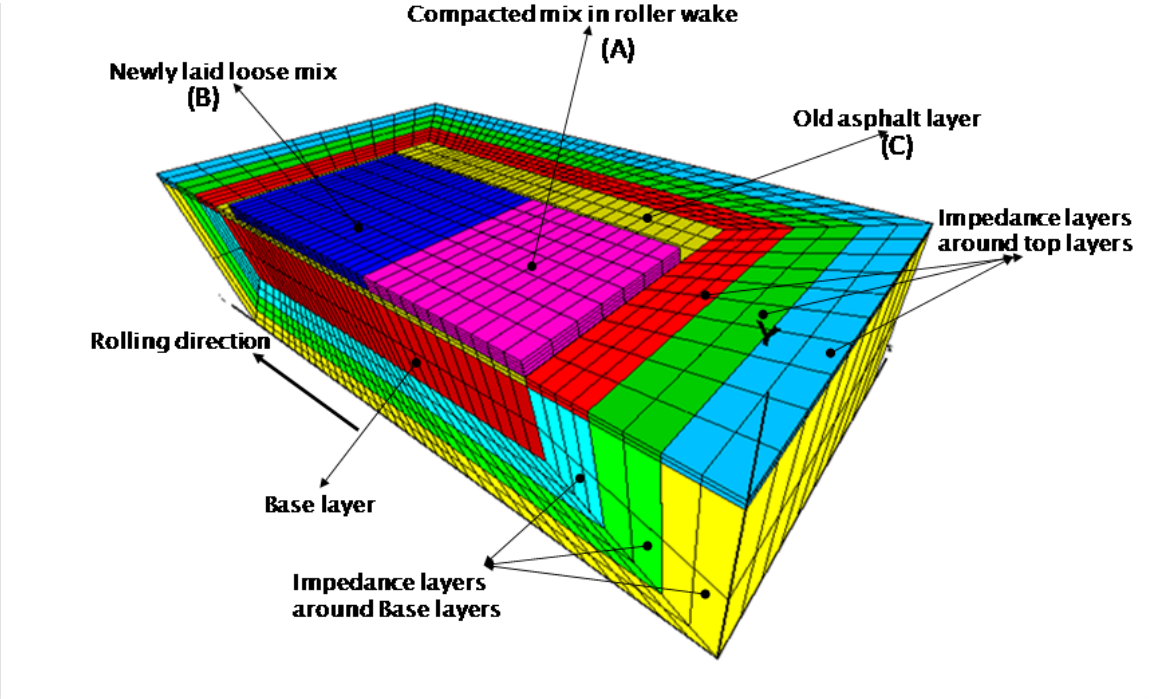

Fig. 41.: Sectional view of the finite element mesh used for setting up field compaction simulations

1. Boundary Conditions for Simulating Field Compaction

The boundary conditions most frequently utilized are diagrammatically presented in Figure 42. The schematic illustrates that the fixed edge corresponds with the inner edge of the pavement lane while the free edge corresponds with the outer edge of the lane. The displacement on the fixed edge are thereby constrained in the lateral direction (Z coordinate direction for the given mesh orientation) and the free edge is unconstrained and a traction free boundary condition is employed.

In the case when the middle lane of a highway is to be simulated one can simplify further by assuming symmetry in boundary conditions and employ a half mesh along the direction of rolling. In that case the half sectional mesh represented in Figure 41 is sufficient for the simulation.

2. Response to Moving Load

We now proceed to demonstrate typical response of the material to a moving load in field compaction. The simulations presented in this section are performed with material parameters that correspond to those in Table V.

The typical response curve obtained from the simulations employing the previously described mesh subject to the specified boundary conditions is given by Figure 43. The response curve represents the compaction experienced at a point in the roller path, as the roller passes over it and returns for a second pass from the opposite direction. The annotating arrows used signify the forward motion in the first pass and the reverse direction motion in the second pass. Finally the load is removed and material allowed to relax, as much as possible. Thereafter, the material finally exhibits its state of permanent deformation, as seen in Figure 43. A diagram to illustrate the correlation of the roller position with the deflection experience by a point P near the

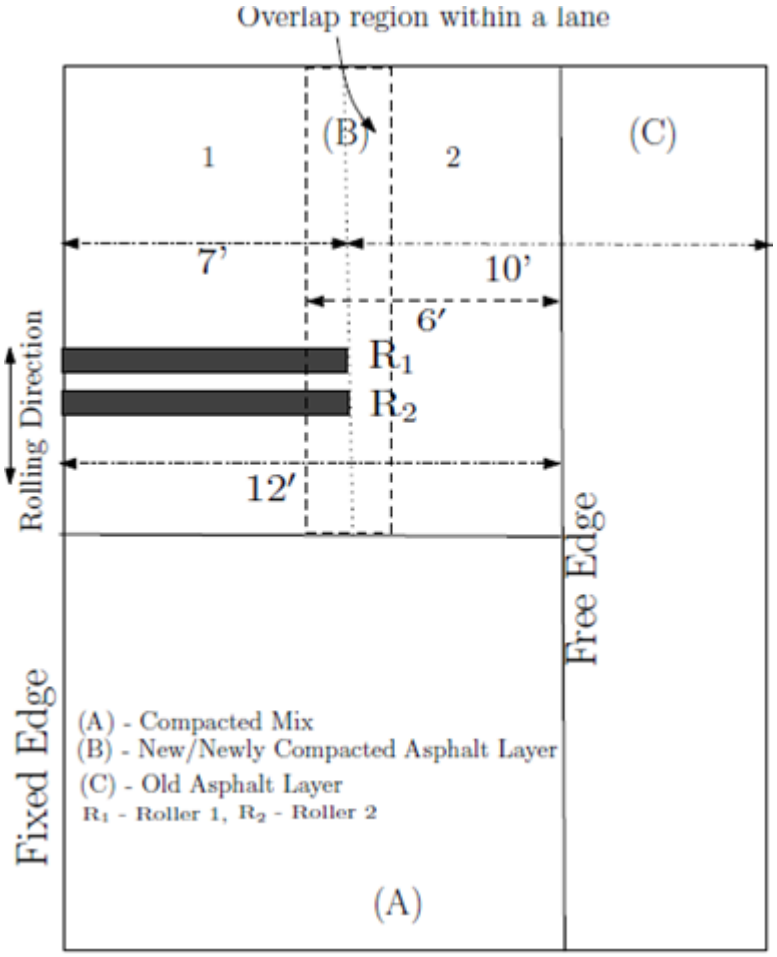

Fig. 42.: A schematic diagram illustrating the edges of the lane that correspond to fixed and free edges in the mesh in Figure 41

surface of the pavement is presented in Figure 44. The diagram indicates that the roller travels from position A towards position B in the first pass and then in the 'reverse' direction from point B to point A in the second pass and so on. As the roller moves toward, passes over and continues to move away from a point of observation, the deflection of the point is noted. The markers signifying the roller position and the deflection of point P have been indicated with coordinated colors at different time steps during the motion (Figure 44). In the plots presented in this section the arrows going from left to right indicate a forward motion of the roller and the arrows going right to left indicate a reversal of roller direction (as in Figure 43).

The deflection observed in the mesh at a point of interest as the load is applied and then removed is represented in Figure 45. As the roller passes over the point and moves further away the material relaxes and is then subjected to further deformation from this relaxed state during the following pass. The deformation therefore builds up incremental with each pass, as can be seen from Figure 46. The increments reduce in magnitude as the number of passes increase owing to material densification.

Table V.: Parameters used to study the typical material response during field compaction

Highway Project	$\hat{\mu}$, (MPa)	n_1	λ_1	q_1	$\hat{\eta}$, (MPa.s)	n_2	λ_2	q_2
SH21	620	4	0.25	-15	1400	2.5	0.25	-20

3. Implementing a Contact Area Algorithm

The loading algorithm used initially in this project was based upon translating a uniformly distributed load across the pavement. Such an approach presents an ideal-

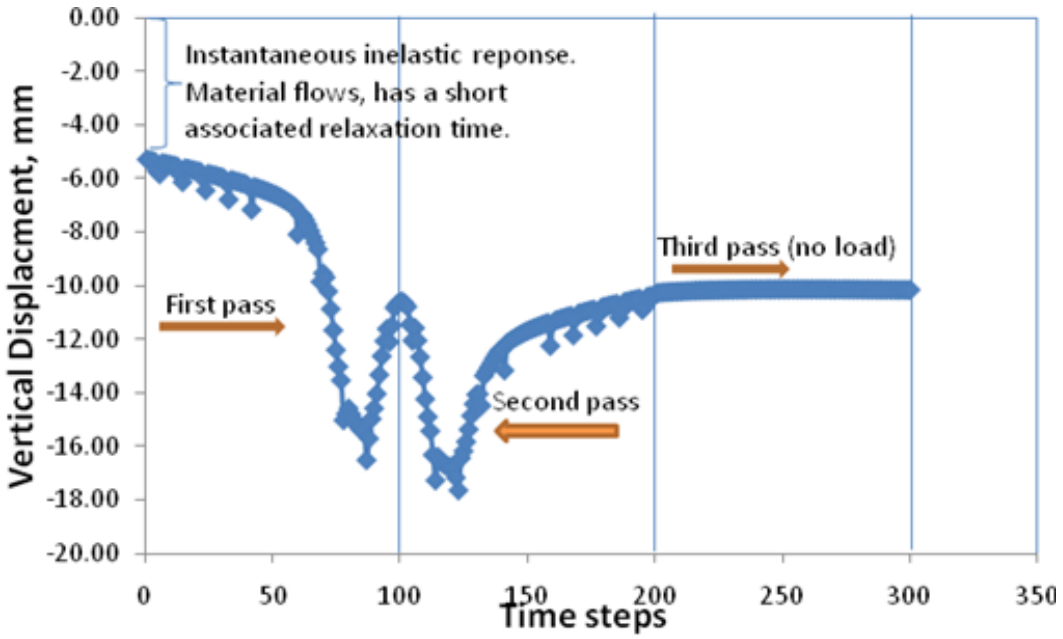

Fig. 43.: Typical displacement curve for a node under the cylindrical load for a cycle with forward and return passes followed by response after load removal (for the node experiencing the maximum deflection)

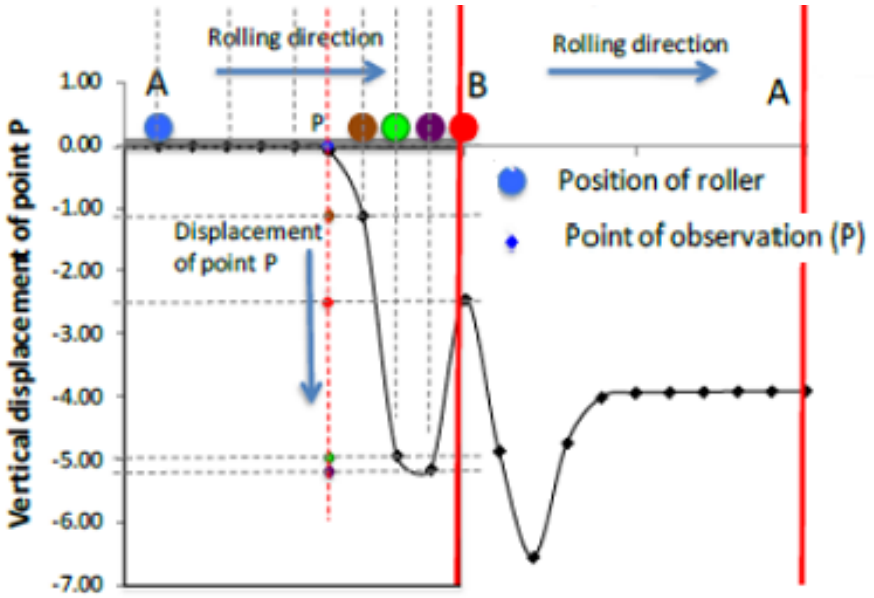

Fig. 44.: Compaction observed at a point P, near the surface, on the path of the roller. As the roller passes over P, the vertical deflection of P keeps increasing as shown

ization of the contact profile between the drum and pavement surface. This section discusses the development of a more accurate method of applying a rolling load on a flexible pavement.

The load is applied in the form of a grid of patches over the elements of the mesh surface, with the pressure uniform over each such patch. We then apply a suitable pattern of the loading by specifying the number of patches to be used over each element surface. The applied static patch loads are translated along the surface of the pavement to simulate the roller moving along. It is noted that the load to be applied per representative area of the mesh, i.e. an element, can be applied by choosing one load patch per element or by selecting representation of the load through multiple load patches per element. The implementation of the loading algorithm therefore allows us a certain freedom in choosing load application schemes and is adequately

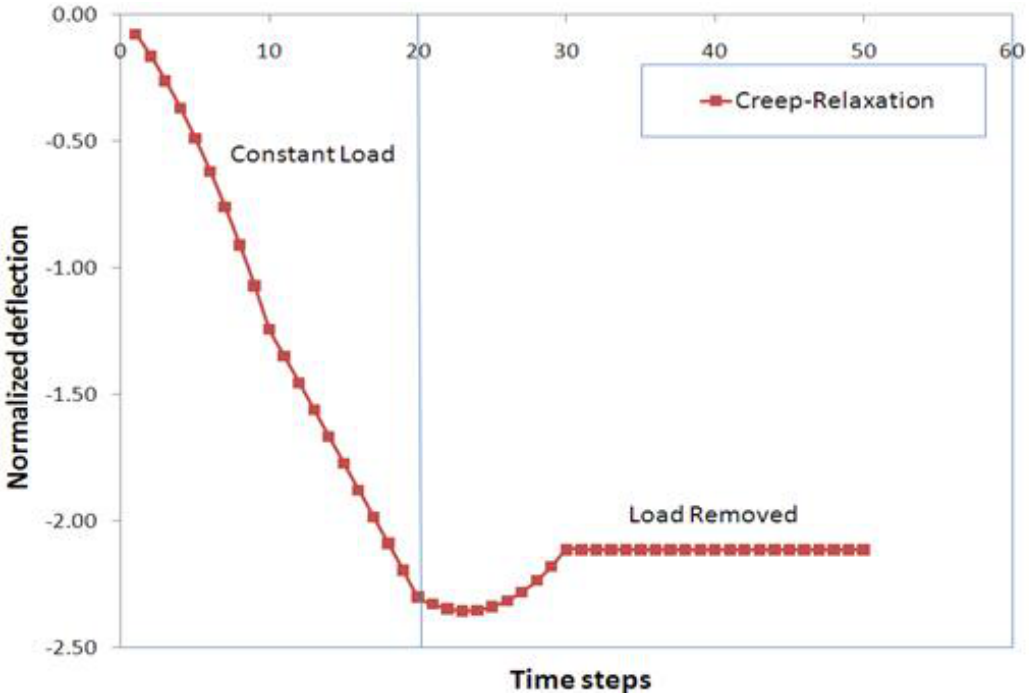

Fig. 45.: Deflection at the node of interest when load is applied for a short duration and then removed. Permanent set obtained even for short term loading

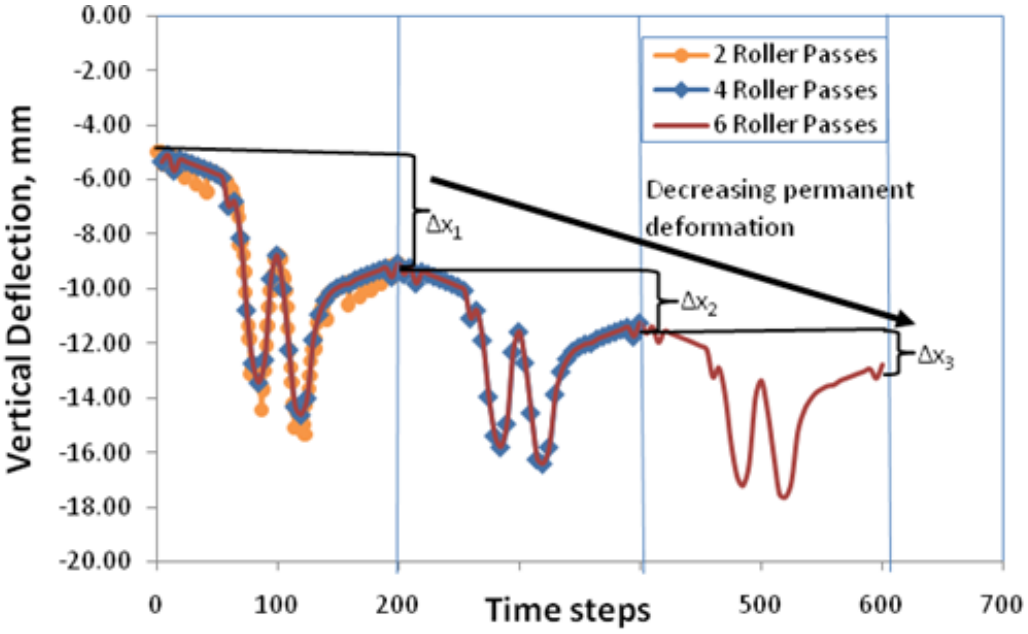

Fig. 46.: Permanent deformation prediction of the model in multiple pass loading, deformation per pass decreases as material gets compacted ($\Delta x_1 > \Delta x_2 > \Delta x_3$)

functional for the purpose at hand.

a. Determination of Nodal Loads

A process for determining the appropriate nodal loads balancing the dead load of the roller is developed. The process involves examining the distributed forces in the elements in contact during a static indentation (Figure 47 and Figure 48) mimicking the cylindrical profile of the roller. The nodal forces thus obtained are then compared against the theoretically predicted distribution of forces for such a finite element. Such a comparison is made within our numerical loading setup by examining the nodal forces arising in a typical element under a distributed surface load. The maximum number of elements that exhibit a force distribution in accordance with the theoretical force distribution for a similar finite element represents the total contact area we require to use for the problem.

The plots presented in Figure 49 represent the nodal reaction forces in the elements in response to applied dead load of the roller, as the contact area (represented by the number of elements in contact) is changed. Here, A1 and A2 represent the edge and middle nodal forces of same orientation in an element when we consider six elements in contact between the roller and the mat. Similarly, B1 and B2 are nodal forces at the edge and middle nodes of an element when four elements are chosen in contact and C1 and C2 when two elements are chosen in contact.

The appropriate (maximum) area of contact is decided based on the sign of the reaction forces of two consecutive middle nodes being the same, as this indicates conformity of force distribution within the element to the prediction based on theory. The theory for a quadratic finite element requires the nodal force distribution over an element subject to a distributed force be so that the force at middle node of the element to be of an opposing sign to the forces at the edge nodes (see Bathe [59]). This principle is violated when 6 elements are considered in contact but is not when four or fewer elements are in contact. Since the nature of the material is such that it will flow around the roller when indentation occurs, the maximum possible area of contact that does not violate the mechanics governing the behavior of the finite elements needs to be considered as the true area of contact. Hence we choose four elements in contact in the loading algorithm employed to simulate a roller contact.

Once the indentation load required to approximate the roller profile is determined, the load is then translated over the pavement. This serves to provide a loading effect similar to sliding a roller over pavement.

For the purposes of the analysis presented in this section, the travel speed for the roller is assumed to be 3.0 miles/hr. This speed is selected so as to enable the researchers to simulate the effect of initial/breakdown passes (Table VI) of the rolling compaction process. These initial passes have been documented in literature to be

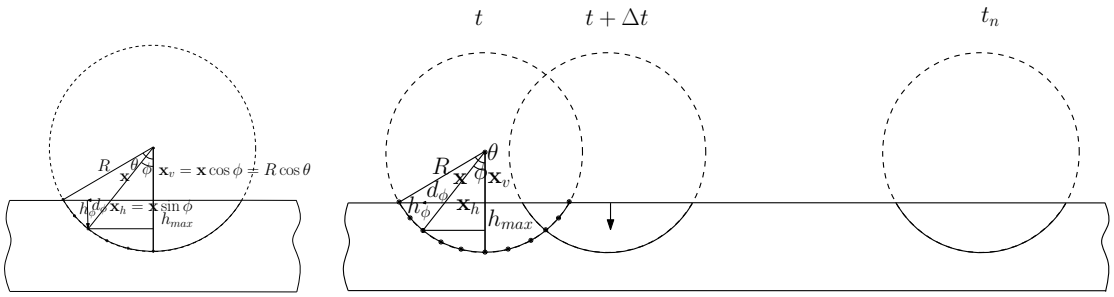

(a) Static indentation (b) Indentation during motion

Fig. 47.: Roller contact geometry for static indentation and during motion

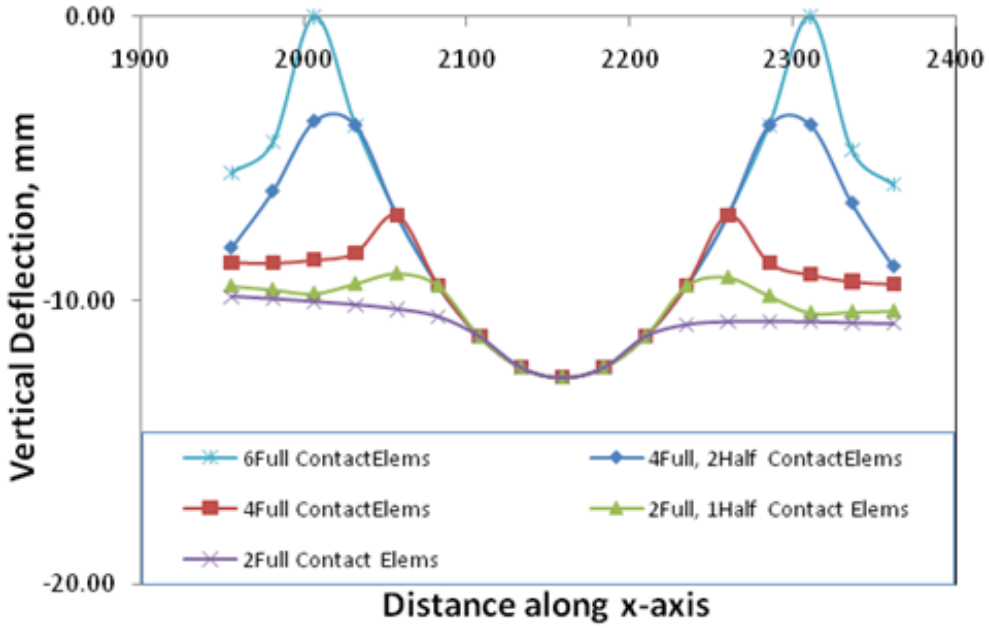

Fig. 48.: Indentation of a cylindrical roller into pavement. Different number of elements maintained in contact to balance the dead-weight of the roller. (Note: y-axis is disproportionate in comparison with the x-axis scale)

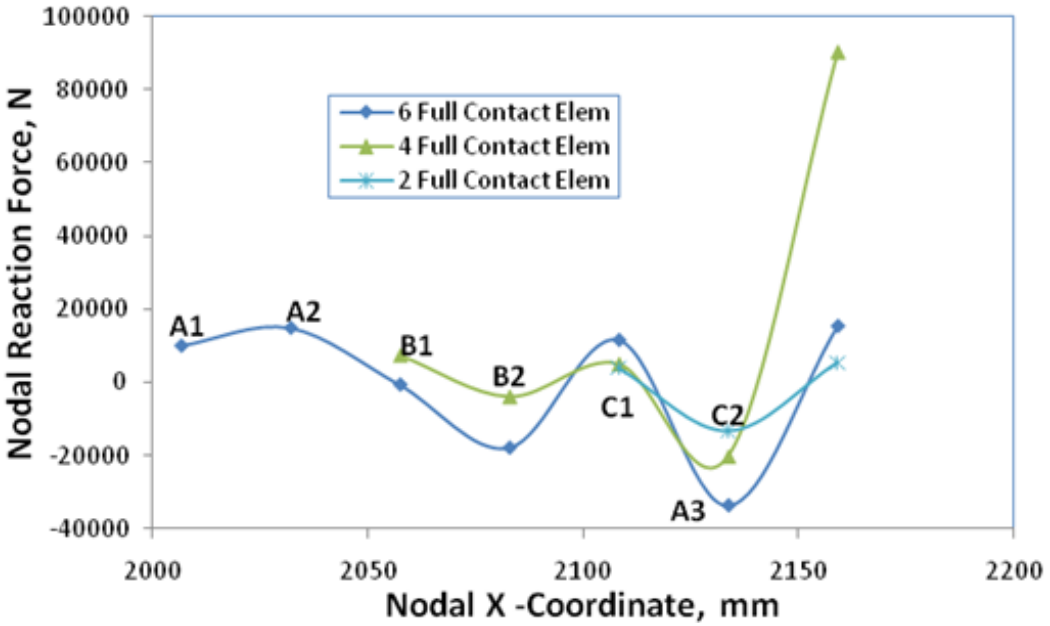

Fig. 49.: Change in nodal reaction forces as the load is applied over a smaller area (i.e. 2, 4 elements in contact as against 6 elements in contact)

important for the purposes of providing a uniform air-void distribution.

The plots in Figure 50, Figure 51 and Figure 52 are indicative of the differences observed in the displacement and stress response in an element in the direct path of the traversing load, using the currently developed contact area algorithm and the previously available loading algorithm in CAPA-3D, wherein the load is applied uniformly over all the finite elements in contact with the roller. The plots shown are representative of the response of the material at a node directly under the load (experiencing maximum normal distress) at the beginning of the simulation. The stress response of the pavement while the new cylinder indentation algorithm (non-uniform pressure) is employed is characteristic of the non-uniform stress reactions obtained in a 20-noded element, whereas the algorithm in use earlier strictly enforces uniform pressure at all nodes under a loaded area at a given instant of time. This, therefore, validates the choice of the use of the cylinder indentation algorithm to better

Table VI.: Typical roller speed ranges (from TRB publication [1])

Type of Roller	Breakdown	Intermediate	Finish
Static Steel Wheel	3.2 – 5.6 km/h; (2.0 – 3.5 mph)	4.0 – 6.5 km/h; (2.5 – 4.0 mph)	4.8 – 8.0 km/h; (3.0 – 5.0 mph)
Pneumatic	3.2 – 5.6 km/h; (2.0 – 3.5 mph)	4.0 – 6.5 km/h; (2.5 – 4.0 mph)	6.4 – 11.2 km/h; (4.0 – 7.0 mph)
Vibratory Steel Wheel	3.2 – 4.8 km/h; (2.0 – 3.0 mph)	4.0 – 5.6km/h; (2.5 – 3.5 mph)	not used

represent the physical contact situation between the roller and the pavement. The simulation results presented in this section utilize the material parameters presented in Table VII.

Table VII.: Material parameters used to investigate Contact algorithm

Highway Project	$\hat{\mu}$, (MPa)	n_1	λ_1	q_1	$\hat{\eta}$, (MPa.s)	n_2	λ_2	q_2
SH21	2500	4	0.25	-25	2000	5	0.22	-30

4. Normal Stresses Predicted by Model

Now, the solution of a cylinder indented into an elastic medium (semi-infinite half space) is compared with the solution in the case of our material model by balancing the self-weight of the roller with the normal reaction from the material. Then the mean contact pressure to be used for the elastic solution is calculated using the expression,

$$p_m = \frac{P}{\pi a^2} \tag{B.1}$$

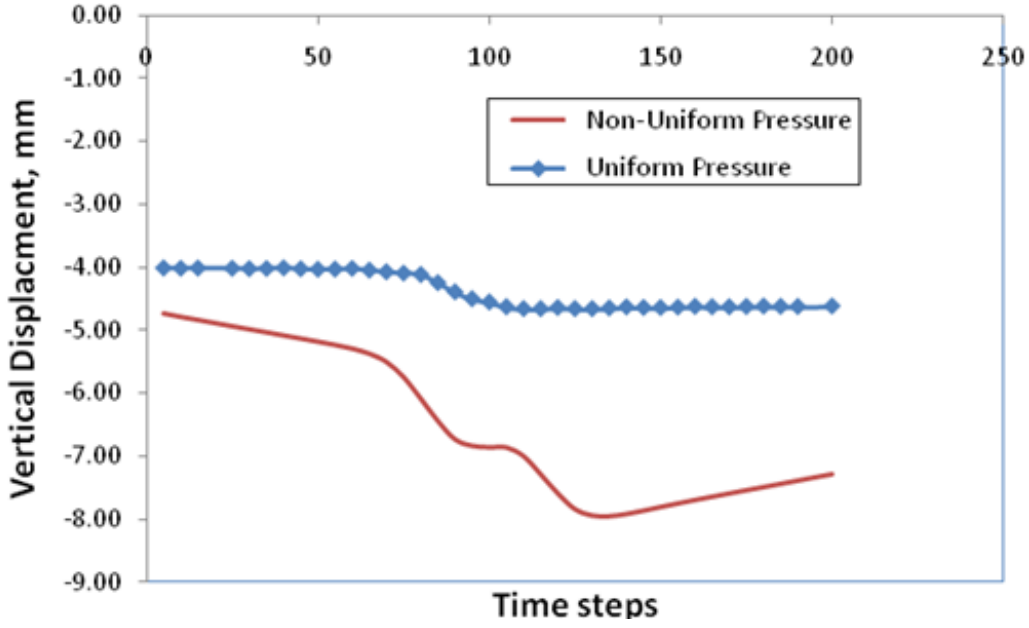

Fig. 50.: Comparison of vertical displacement for the two different patterns of loading

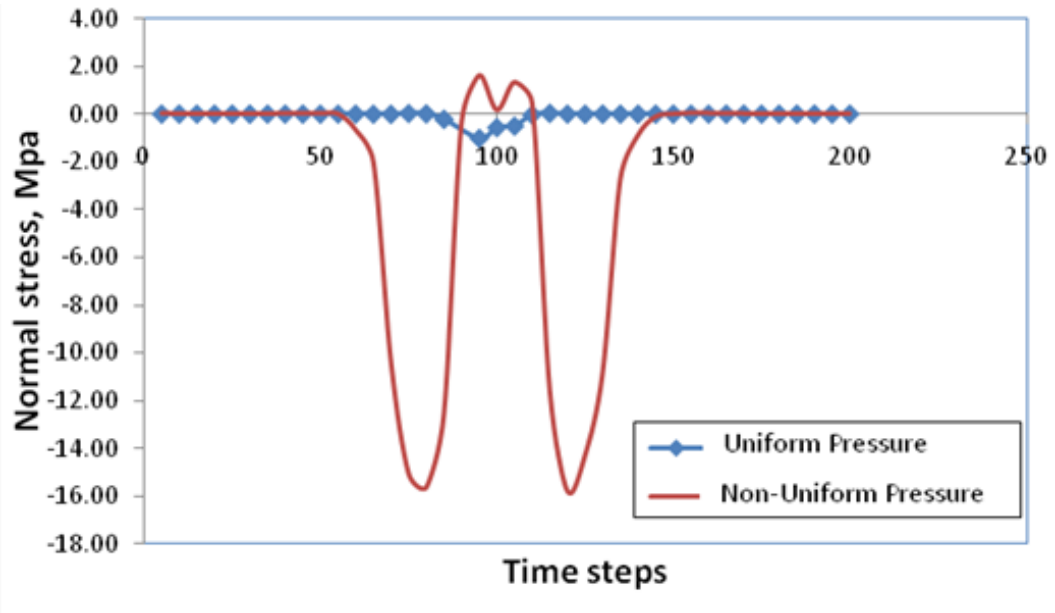

Fig. 51.: Comparison of the normal stress distribution at the pavement top surface due to different loading patterns

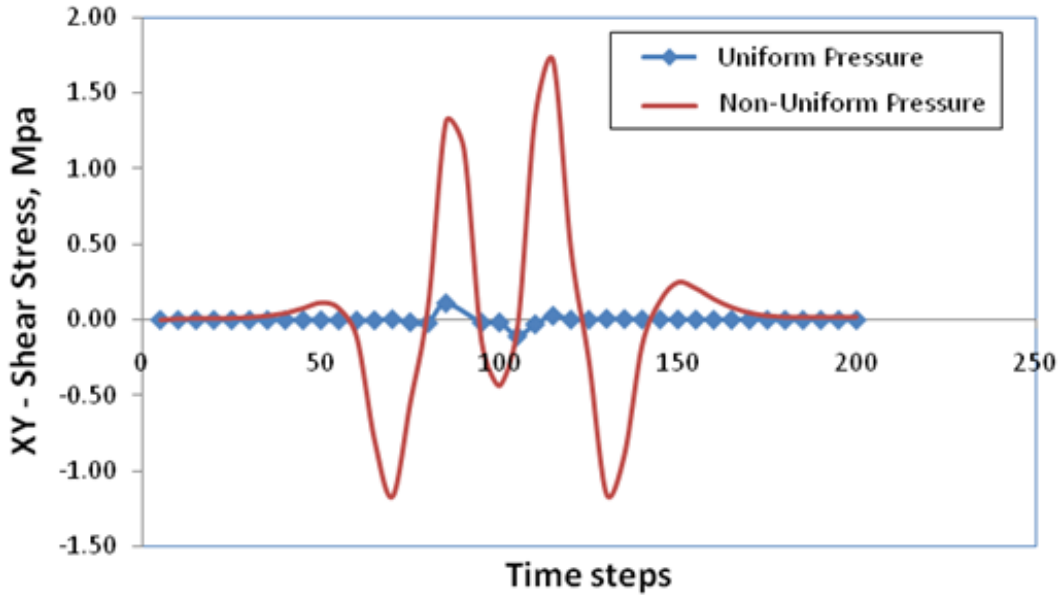

Fig. 52.: Comparison of the shear (XY) stress distribution of the pavement top surface to the different loading patterns (on plane of symmetry)

where, 'P' is the load per unit thickness in the z-direction and 'a' is the radius of contact. We use the self-weight per unit pavement width as 'P'. The normal stress in the elastic medium is then given by the expression

$$\frac{\sigma_z}{p_m} = -\frac{4}{\pi}\left(1 - \frac{x^2}{a^2}\right)^{1/2} \tag{B.2}$$

The above representation of the solution indicates that the normal stress is expressed solely as a function of the position 'x' and the mean contact pressure 'p_m'. This relationship is graphically illustrated (Figure 53) in comparison with the instantaneous normal stress produced in the HMA material used in the compaction simulations, with the same mean normal pressure applied. The comparatively higher stresses in the elastic medium at a given mean contact pressure is due to the lack of any dissipative mechanism in the elastic material. The model we employ for representing the HMA develops dissipative responses in a nonlinear manner and hence the instanta-

neous response shows less stress. Also, the low level of stress in the HMA shows the low viscosity fluid like pre-compaction behavior of the model.

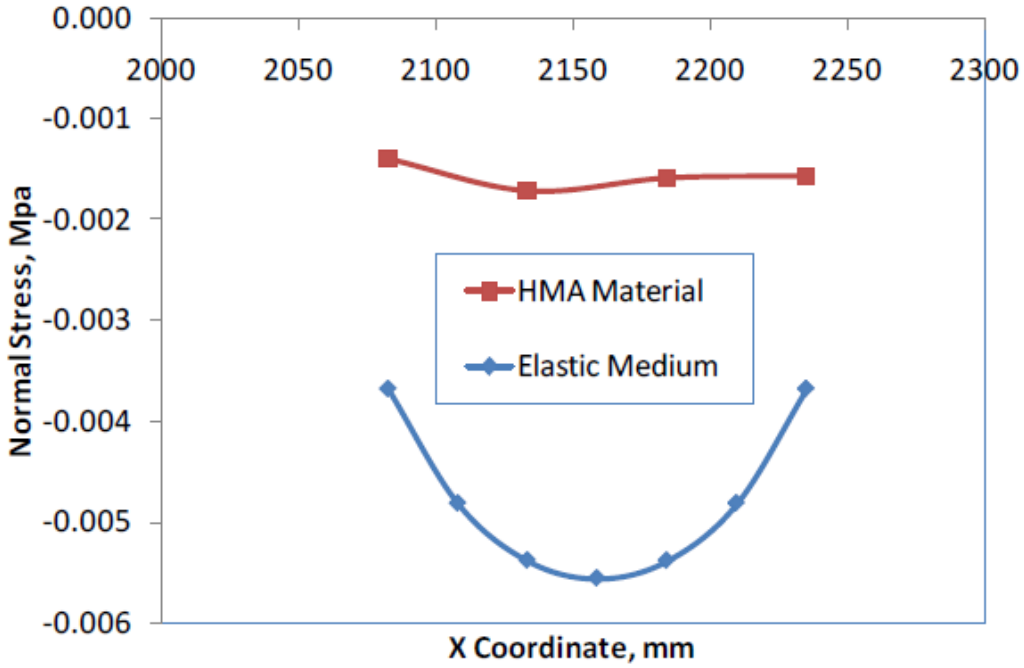

Fig. 53.: Comparison of the normal stress predicted by the model with the normal stress predicted for an elastic medium (for the same 'mean contact pressure, p_m')

5. Interface Elements

The finite element analysis is dependent on the use of an interface element layer between the top asphalt layer and the previously compacted layer of asphalt as well as between the top newly laid asphalt and the old asphalt sub-layer. This is due to the differences in properties of the loose mix and the stiff old asphalt layer it comes in contact with. Hence, the specialized interface elements are employed to resolve the contact issues arising due to the large variation in properties of material on either side of the interface. With the establishment/implementation of a useful contact area algorithm in CAPA-3D, we perform analysis to obtain insight into the effect of the

interface elements. The use of interface elements provides a numerically stable and converging simulation. These interface elements do not contribute to the structural properties of the whole structure and their applicability has been documented (for details see Scarpas [56]) elsewhere. The interface elements to be used require the specification of two shear and one normal stiffness moduli. These stiffness values are used by the numerical algorithm to ensure the contact in maintained between the layers by artificially attaching the corresponding nodes of the layers through a mathematical expression that governs their relative motion. The shear stiffness's are used to govern the relative sliding of the layers where as the normal stiffness is used in preventing the mesh penetration of the finite elements of a stiffer material into a those of a soft material. The results of finite element analysis using the interface layer are presented in Figure 54, Figure 55, Figure 56 and Figure 57. Here the 2 shear and 1 normal stiffness properties are varied and the resulting structural behavior of the HMA material is observed. The shear moduli are individually made stiffer and comparison is drawn against a reference set of interface element stiffness's. The same comparison is made after normal stress is made less stiff. It can be observed from the plots representing pavement response to various interface element stiffness's, that the use of interface elements does not adversely affect the normal and in plane displacement response of the model (Figure 54, Figure 55, Figure 56 and Figure 57). The slight deviation observed in the case when z-direction shear is stiffened is attributed to the structure of the mesh. The mesh used is longer in the z-direction and hence the effects of free boundaries are more pronounced. The situation is rectified by using higher stiffness value, as beyond such a value the interface exhibits similar behavior as in the case of the x-direction.

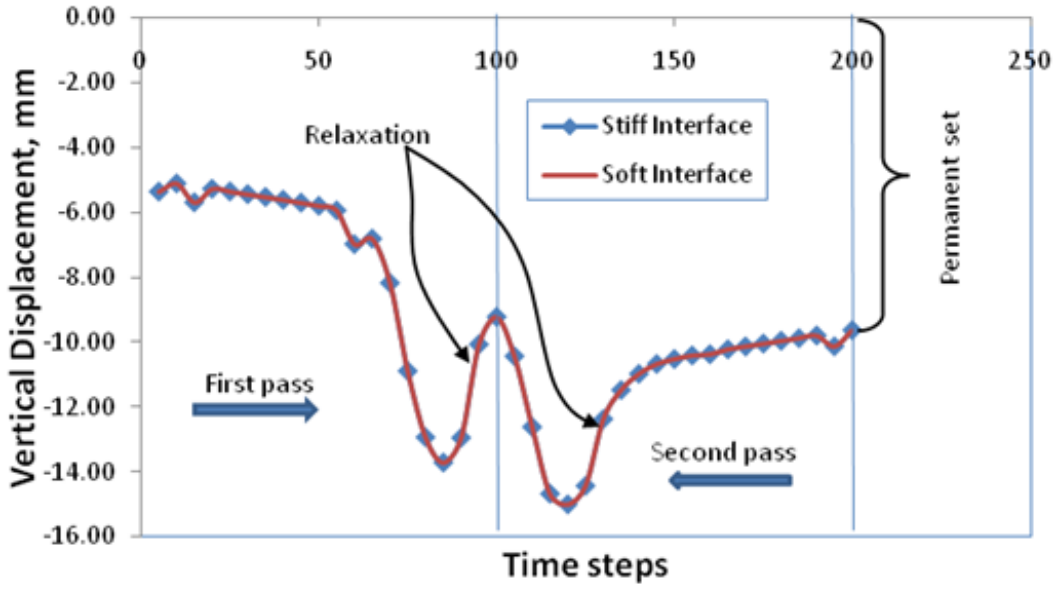

Fig. 54.: Comparison of pavement vertical response as the normal stiffness of the interface elements is lowered by an order of magnitude from 10000 MPa to 1000 MPa

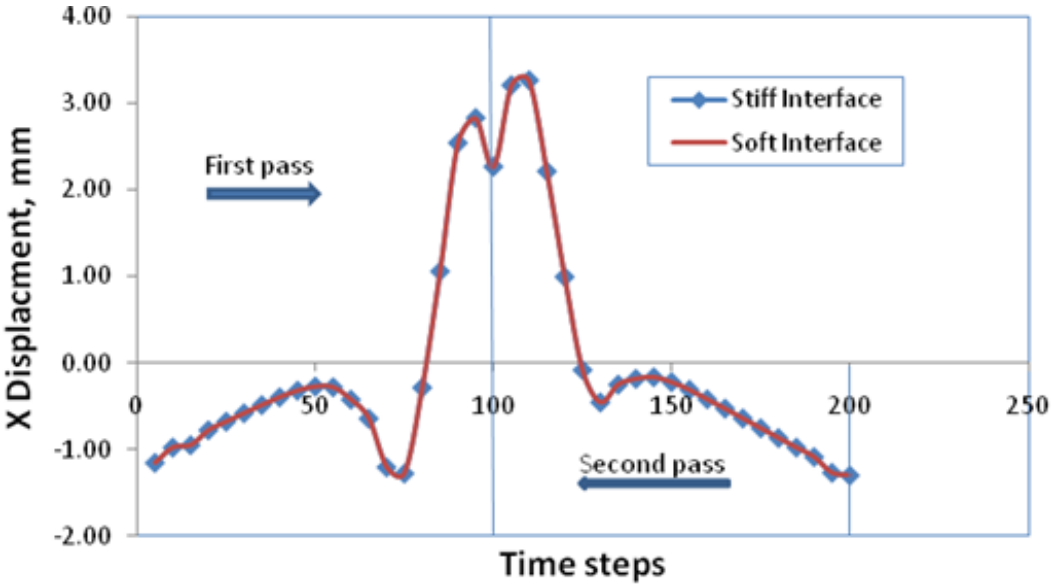

Fig. 55.: Comparison of pavement response in the rolling direction, as the normal stiffness of the interface elements is lowered by an order of magnitude from 10000 MPa to 1000 MPa

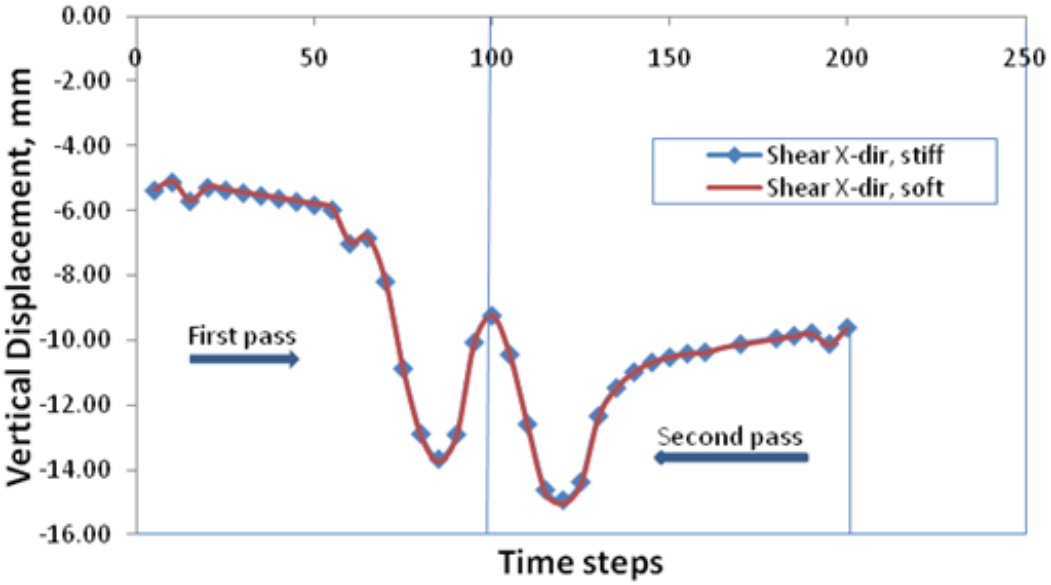

Fig. 56.: Comparison of pavement response to increasing the shear stiffness in the X-direction

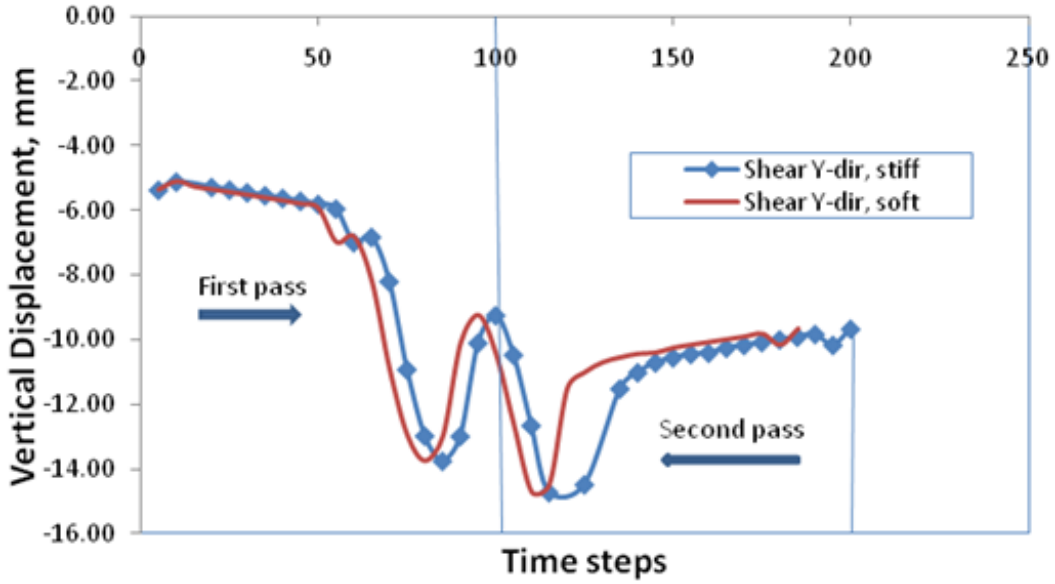

Fig. 57.: Comparison of pavement response to increasing the shear stiffness in the Z-direction

6. Use of Impedance Layers

The impedance layers built into the finite element mesh at this stage are not exploited for the current analyses, as an essentially non-dynamic loading is studied. However, their impact on a the finite element model is recorded thorough some simple examples for the sake of completeness. These elements were included as part of the plan to study the effects of a true dynamic loads on the asphalt pavement structure. The use of impedance layers is necessitated by the need to dampen out the wave reflections caused at the interface between layers when the pavement is subject to dynamic loads. The techniques used to overcome the ill-posedness of the initial value problem, owing to which we obtain wave reflections at interfaces in highly viscous and elastic media, involve progressively dampening the displacement waves propagating the medium through use of numerically cheap impedance layers. These layers are primarily composed of elastic material with each enclosing layer proportionally less stiff in comparison to the inner one it is in contact with. This proportion, the 'acoustic impedance', is maintained so as to keep an interface between different materials from reflecting waves that can interfere with the solution. Further details of the uses and applications of such special finite element layers has been documented in Sluys [58].

The 'acoustic impedance' is given by $Z = A\sqrt{E\rho}$, where

$$A = \text{ Crossectional area of the layer,}$$

$$E = \text{ Stiffness of the layer, and}$$

$$\rho = \text{the density of the medium}$$

In the mesh employed three impedance layers are used to encase the pavement structure, each of 25.4 mm. The maximum value of the inner most layer is finally

set at 5000MPa and the densities are calculated such that (the cross-sectional area is fixed by the thickness of the layers) the ratio of moduli between consecutive layers is kept at 10. These values eliminate the wave reflections in the asphalt mix and hence are used for further analysis for all impedance layers.

The response plots shown that have impedance layers around the top fresh mix, old asphalt and base (Figure 58, Figure 59) are useful in reducing the vertical and horizontal reflections significantly to the point that they are completely eliminated as indicated in Figure 60 and Figure 61. Due to this observation a high enough impedance is sought when use of such layers is warranted, keeping the thickness of layers and the density of the material of the layers fixed.

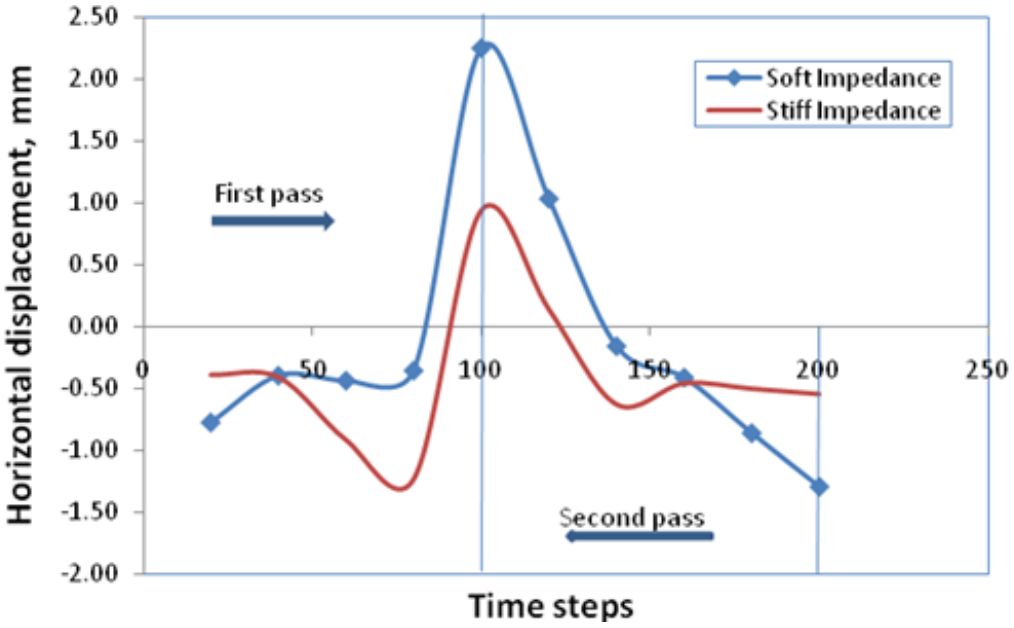

Fig. 58.: Comparison of the dampening effect provided by impedance layers, surrounding the structure laterally, in the X-dir

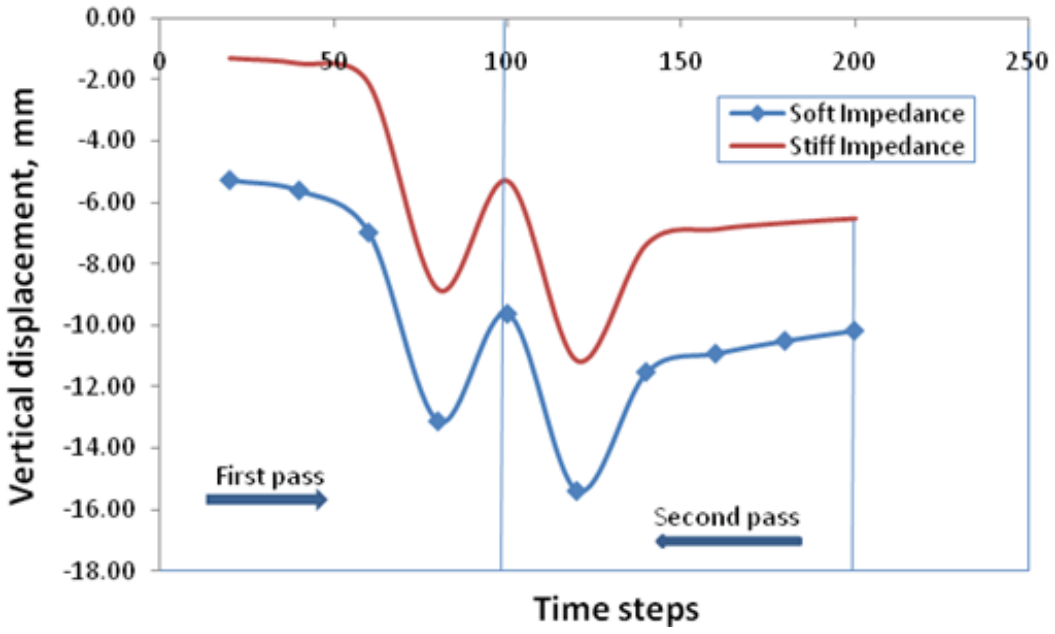

Fig. 59.: Comparison of the dampening effect provided by impedance layers, surrounding the structure laterally, in the Y-dir

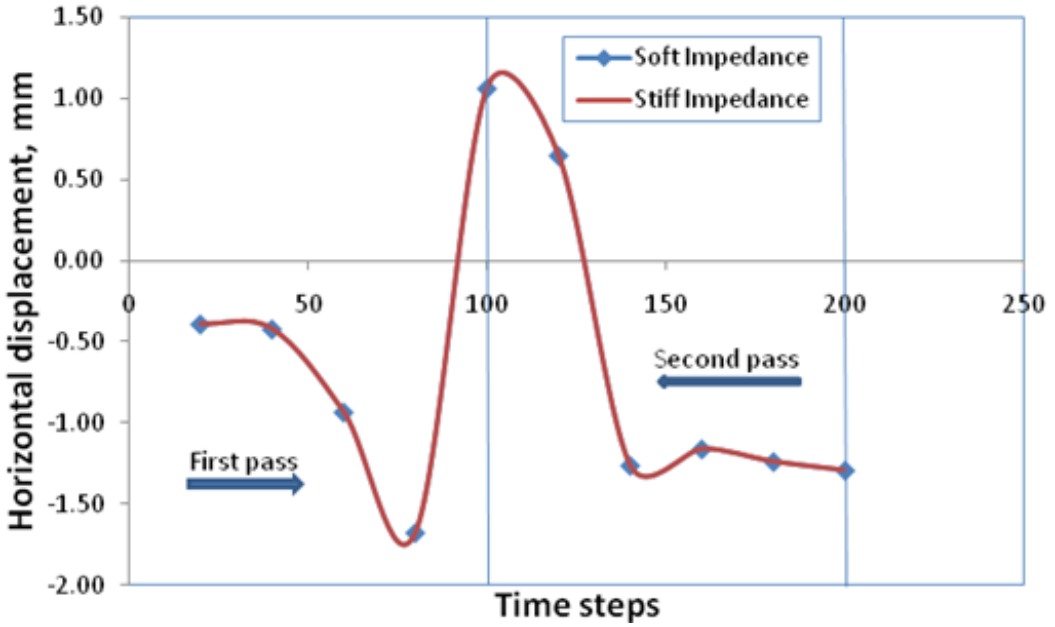

Fig. 60.: Comparison of the dampening effect provided by impedance layers, surrounding the top layer (pavement and old asphalt) laterally, in the X-dir

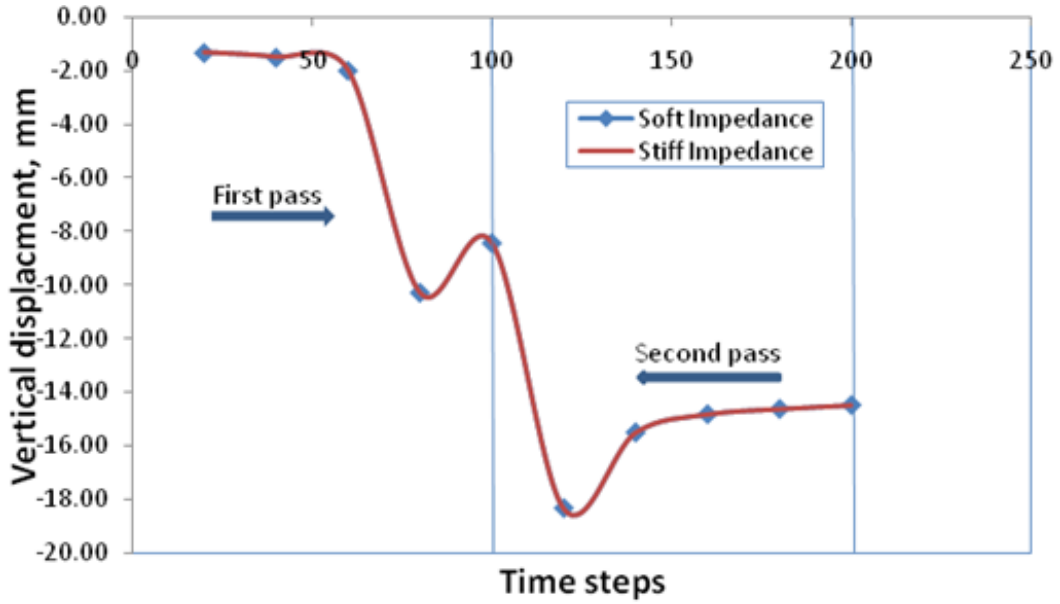

Fig. 61.: Comparison of the dampening effect provided by impedance layers, surrounding the top layer laterally, in the Y-dir

7. Effect of Base Stiffness

Finite element analyses are performed by assigning properties for the base material in order to study the effect of having a single base layer underneath the pavement layers (as in Figure 40 and Figure 41). The results indicate that with the material response does not seem effected much when the material properties of the single base layer are varied over a wide range with a minimum base stiffness value of 500 MPa and a maximum stiffness value of 2000 MPa.

The plots of the volumetric response (Figure 64, Figure 66) indicate that the material response is not very sensitive to changes in stiffness of the base when the response is viewed in an averaged sense. The volumetric response is examined through the evolution of the volumetric component of the viscous deformation gradient, (see Koneru et. al. [52] and Masad et. al. [3]). However the finite element model is

responsive to a drastic increase in base modulus (Figure 62, Figure 63 and Figure 65), due to increasing rigidity in the base structure leading to interference waves (as result of the structural rigidity and not due to any other dynamic characteristic) being reflected internally. This is in contrast with what is observed in the field wherein in mix designs with stiff base materials produce more compaction in the pavement layer owing to the compressive reaction acting on the HMA layer from below. As a result, for further finite element analysis a value intermediate between the two extremes (i.e. between the minimum base stiffness value of 500 MPa and a maximum stiffness value of 2000 MPa, say, 1000MPa) is chosen to conduct parametric and sensitivity analysis presented later.

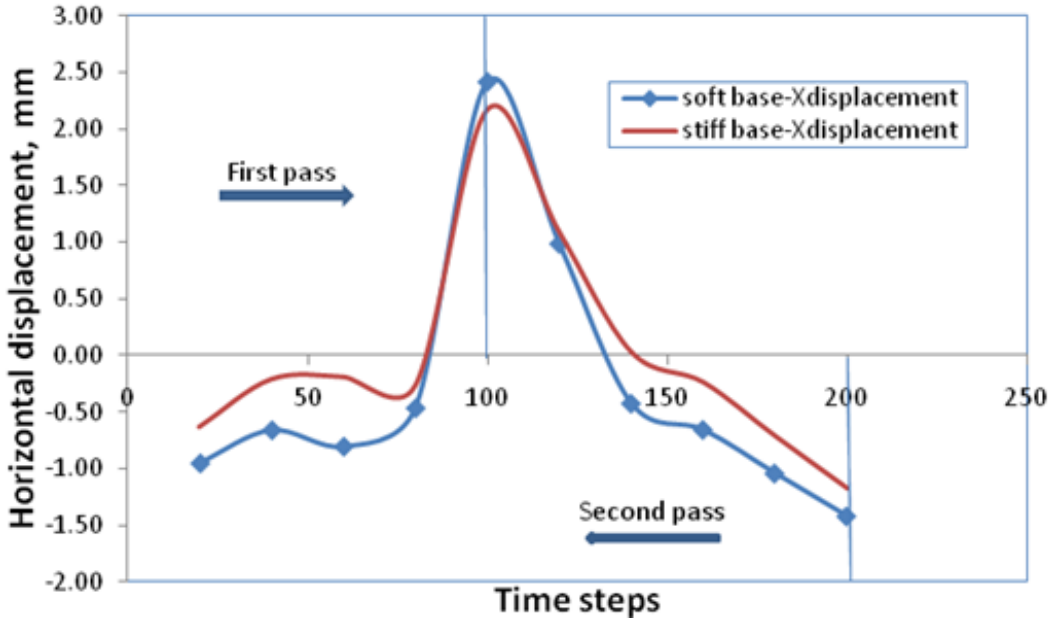

Fig. 62.: Comparison of the effect on the X-displacement of a node in the roller path as the base stiffness is varied from 500MPa (soft base) to 2000MPa (stiff base)

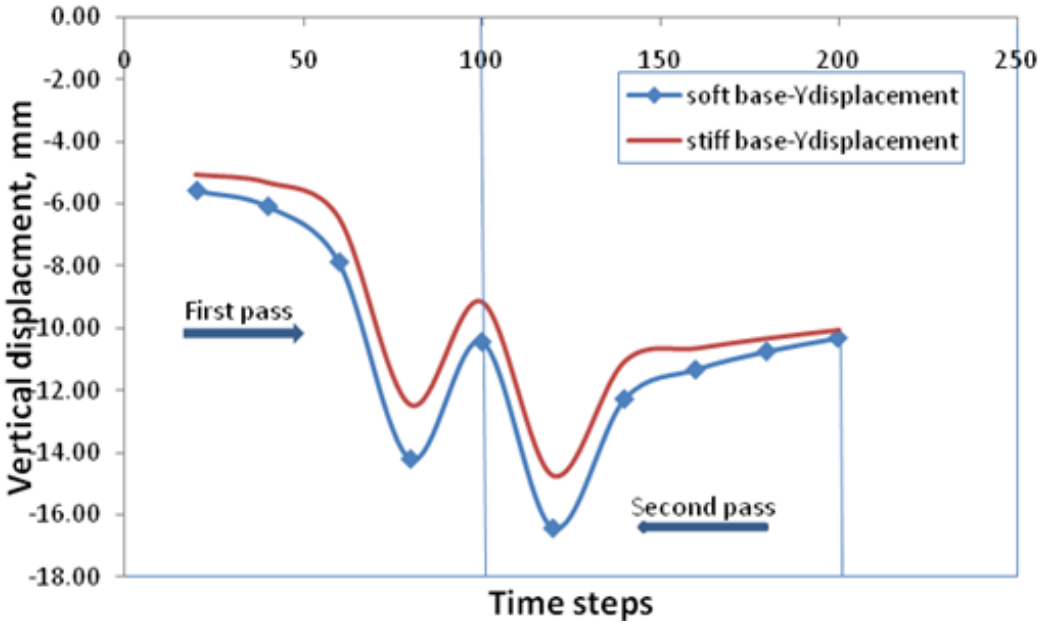

Fig. 63.: Comparison of the effect on the Y-displacement of a node in the roller path as the base stiffness is varied from 500MPa (soft base) to 2000MPa (stiff base)

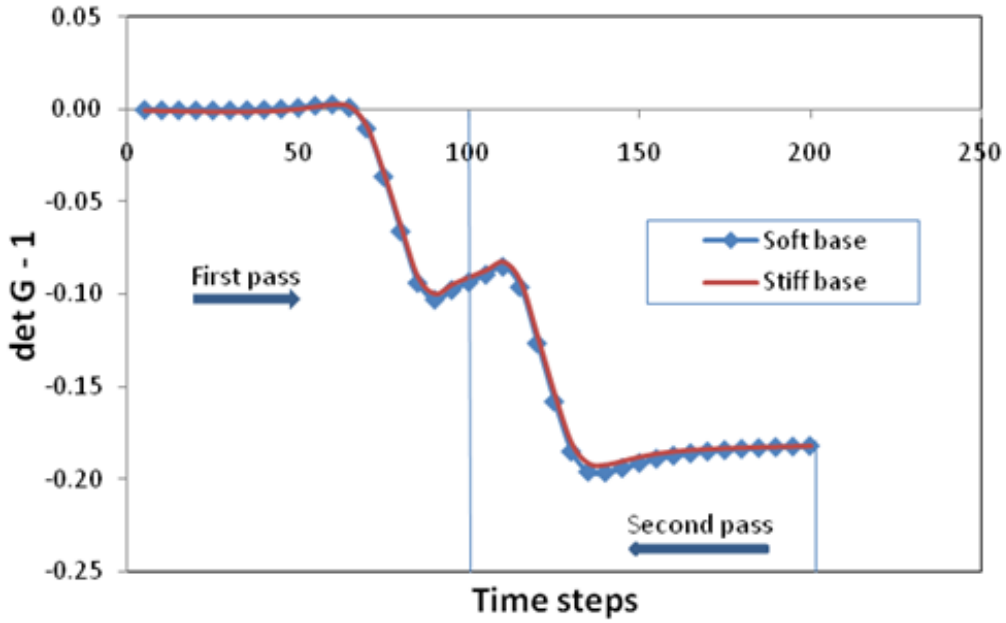

Fig. 64.: Comparison of the volumetric component of the viscous evolution gradient for soft (500MPa) versus stiff (2000MPa) bases

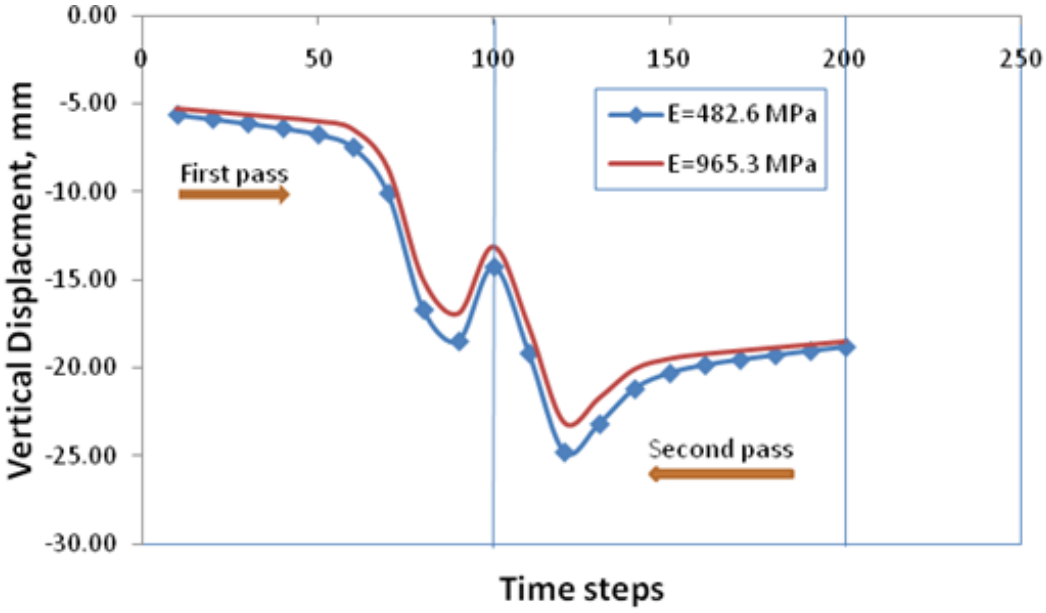

Fig. 65.: Comparison of the deflection for two base stiffness moduli of interest

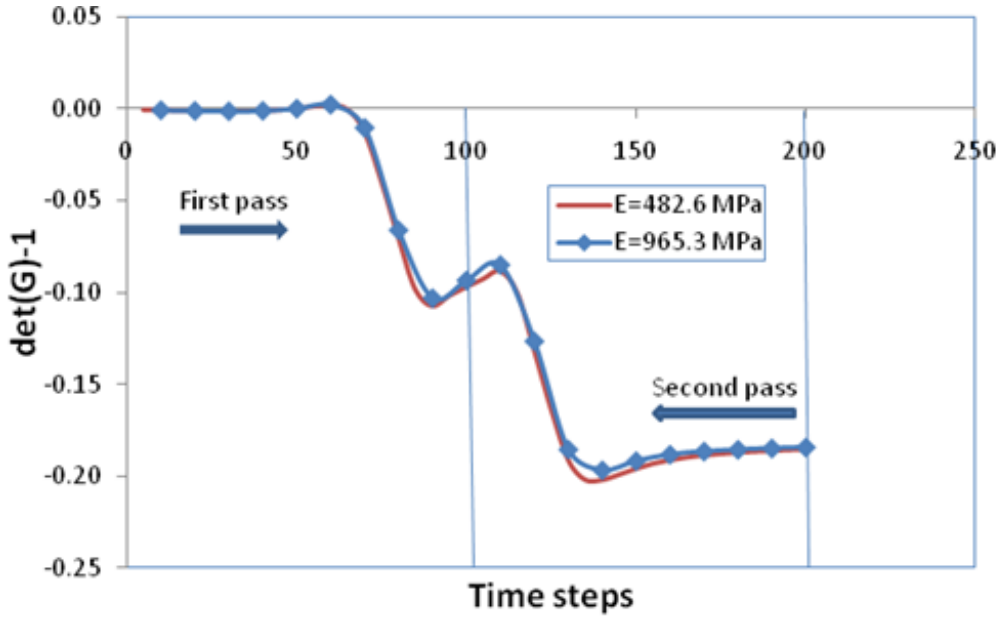

Fig. 66.: Comparison of the volumetric component of the viscous evolution gradient at two base stiffness moduli of interest

8. Compaction Equipment Characteristics

As a further development to the simulation model a vibratory loading algorithm has been developed for use in CAPA specifically for the compaction project. The vibratory loads take into account the effect of displacement amplitude and frequency specifications of the machine used for rolling in a field project by calculating the equivalent load to be used to achieve the same level of compaction. Analytical expressions for calculating the contact forces for cylinder indentation into an elastic pavement material are adapted from Johnson [60]. Thereafter, one calculates the equivalent loads for different amplitudes of indentation as necessary. Then the force necessary for the vibrations is calculated using these analytical expressions at an instant of time and the pressure is redistributed over the contact area. The vibratory load is added on to the dead weight as the initial state, with a half-sine curve providing the vibratory effect. The amplitude of the loading half-sine curve is determined using the centrifugal force data from a roller's vibratory system specifications. For the case of a variation in the vibratory frequencies we simply change the time taken per each load cycle to match the loading frequency.

The effect a dynamic load vibrating at a certain angular frequency 'ω' has on the deformation induced on the material model of our choice, with a certain relaxation time 'λ' associated with it (Figure 70), is also studied.

Simulations are setup on a mesh representative of a 12 feet wide pavement lane with a roller weighing 27000 lbs, a diameter of 51 inches and a width of 7 feet. The results of the simulations (Figure 67, Figure 68, Figure 69 and Figure 70) show the material responds according to the mechanics of the loading algorithm implemented. The results are presented at a point in the interior of the mat along the width (approximately 5 ft from the edge). In the results that follow we use the term 'compaction'

as a measure to represent the viscous evolution, (detG-1). The expression represents the volumetric change that takes place in the viscous evolution tensor **G**.

To summarize one can make the following observation regarding the response of the material:

- We also note that an increase in amplitude of the vibratory load leads to a increase in the amount of compaction achieved as observed in the field compaction (Figure 67).

- The increase in compaction as a result of the increase in amplitude is due to the roller indenting deeper into the mat thereby increasing the pressure on the surface.

- Referring to Figure 68 and Figure 70 we note that increasing the frequency of the vibratory or decreasing the material's viscous nature results in an increase in per cent compaction of the mat as is observed in the field.

- The response of the material to small steps of increase in load (keeping roller area of contact a constant) results in uniform increase in compaction level as indicated in Figure 69.

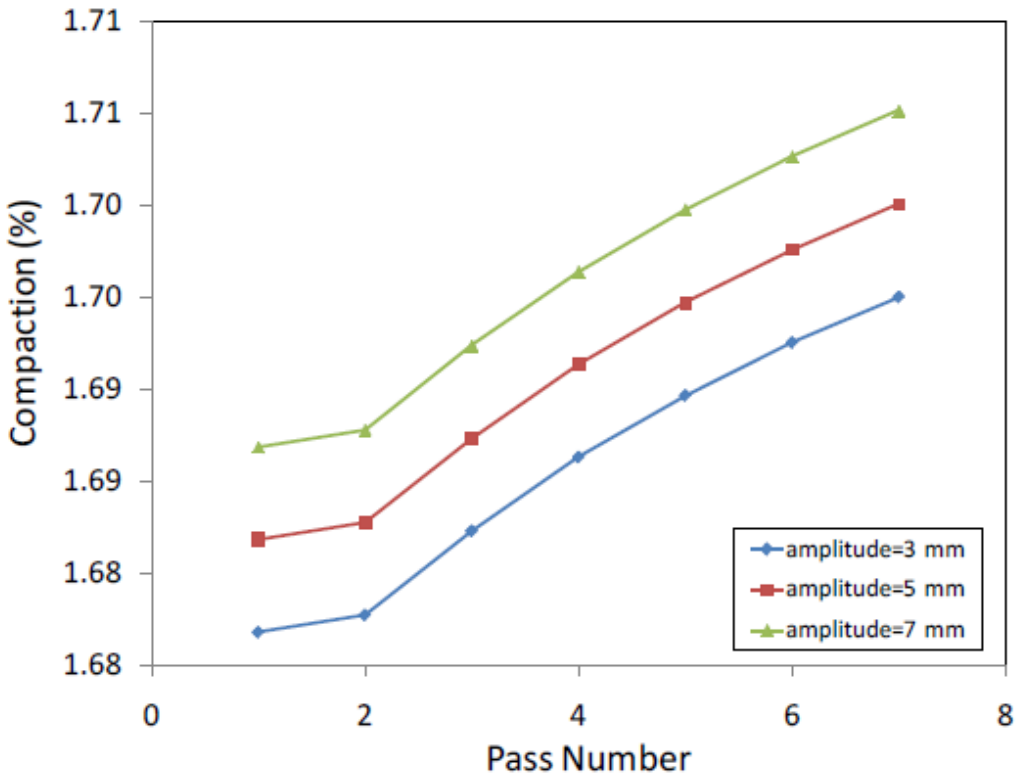

Fig. 67.: Compaction over a sequence of passes as the amplitude of vibration increases

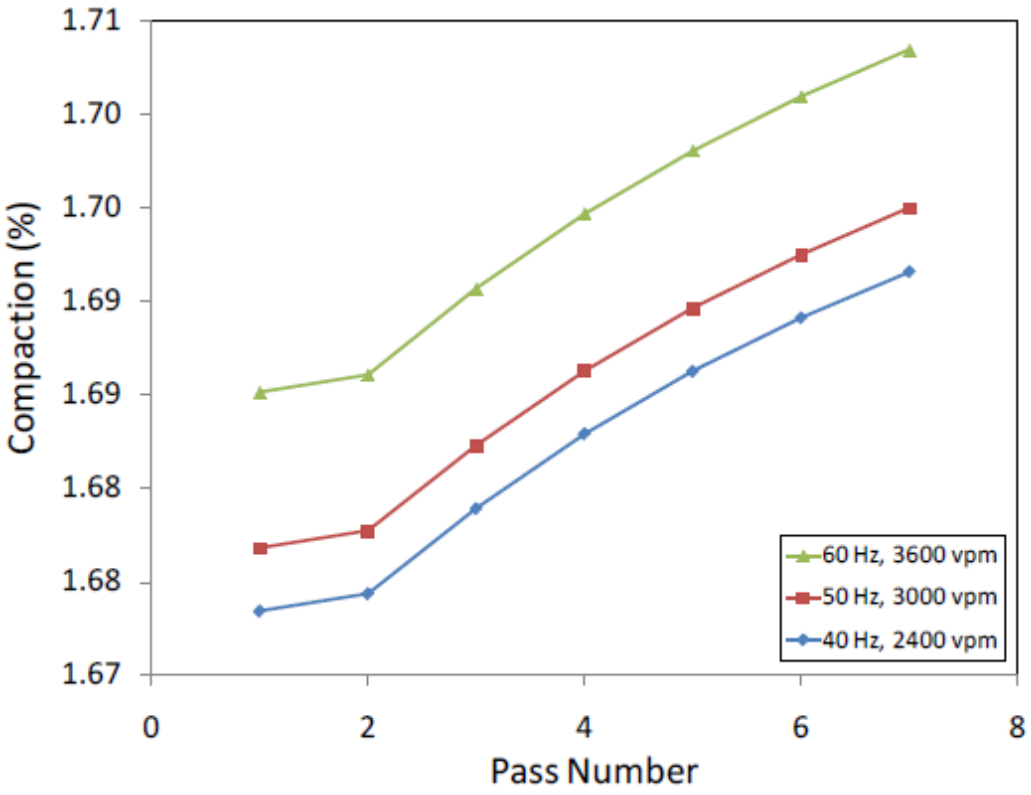

Fig. 68.: Compaction over a sequence of passes at different frequencies

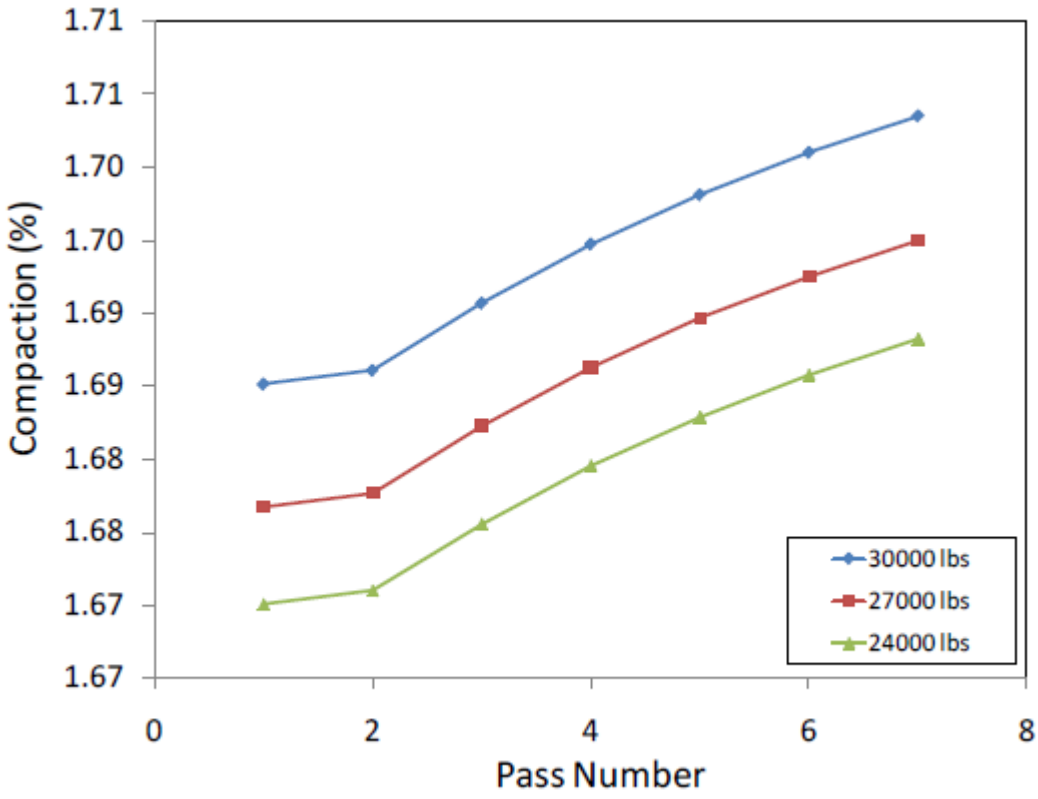

Fig. 69.: Material response to change in dead–load carried by each roller

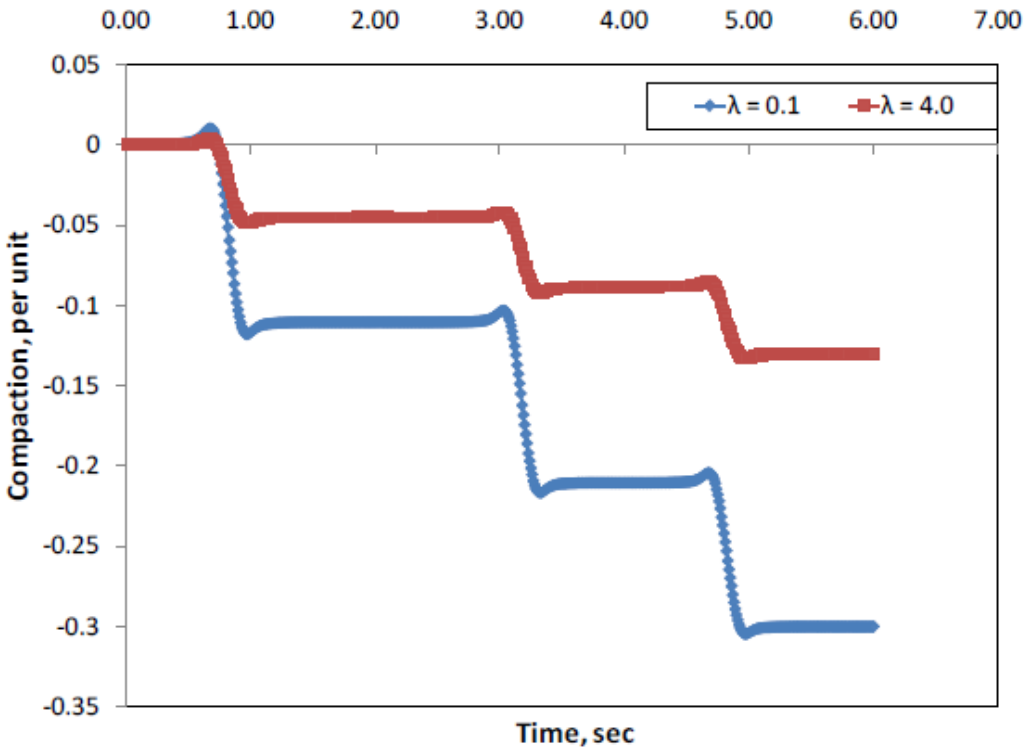

Fig. 70.: Field compaction response at a constant frequency ('ω') over multiple passes on a point. Model predicts more deformation for less viscous (smaller 'λ') material

CHAPTER VII

SIMULATING COMPACTION IN THE FIELD

A. Sensitivity Analysis

The purpose of a sensitivity analysis is to correlate various features of the output of the mathematical model to the different input factors and parameters of the model. The sensitivity analysis is constrained by a lack of experimental evidence/data of the mechanical response of HMA while compaction is being performed in the field. Therefore, to serve our investigations we need to establish a reference material response and hence we choose a reference parameter set to aid us in our sensitivity study. Since compaction of HMA manifests primarily in the volumetric changes that occur during the process we present here a study based on a volumetric measure that quantifies material response. A comparison of the general volumetric viscous evolution response (measured through the mathematical invariant (det(G)-1) as explained in Koneru et. al. [52] and Masad et. al. [3]) of the material with its response when using a reference set of material parameters is presented.

The sensitivity analysis presented here provides us with a general qualitative understanding of the trends of the material behavior in relation to the variation in parameters. The viscous evolution of the model as the different parameters are varied is presented in Figure 71 and Figure 72. The model parameters used to study sensitivity are presented in Table VIII.

1. Observations from Sensitivity Analysis

The response of the material is stiffer (Figure 71) as the viscosity parameter $\hat{\eta}$ is increased. This correlates to the response observed in the SGC simulations and is

Table VIII.: Parameters employed for the sensitivity study of the material

Mix parameter sets	$\hat{\mu}$, (MPa)	n_1	λ_1	q_1	$\hat{\eta}$, (MPa.s)	n_2	λ_2	q_2
Reference set	620	4.0	0.25	-15	1400	2.5	0.25	-20
Set 1 (Change $\hat{\eta}$)	620	4.0	0.25	-15	1700	2.5	0.25	-20
Set 2 (Change $\hat{\mu}$)	810	4.0	0.25	-15	1400	2.5	0.25	-20
Set 3 (Change λ_1)	620	4.0	0.20	-15	1400	2.5	0.25	-20
Set 4 (Change λ_2)	620	4.0	0.25	-15	1400	2.5	0.2	-20
Set 5 (Change n_1)	620	3.0	0.25	-15	1400	2.5	0.25	-20
Set 6 (Change n_2)	620	4.0	0.25	-15	1400	1.5	0.25	-20
Set 7 (Change q_1)	620	4.0	0.25	-10	1400	2.5	0.25	-20
Set 8 (Change q_2)	620	4.0	0.25	-15	1400	2.5	0.25	-15

understood to be due to the material become a more viscous fluid as the compaction progresses. The shear modulus parameter $\hat{\mu}$ causes a significant stiffening of the material response in the initial stages of compaction. This can be observed in the response of the material in the first 50 time steps of the simulation. The comparative increase in the elastic rebound experienced by the mix in the initial stages as $\hat{\mu}$ is increased model corresponds to our constitutive assumption that the stored energy in the material is dependent on the shear modulus function. Thus, the shear modulus also affects the material response as in the SGC simulations but the viscous nature of the material dominates the response as the load traverses the pavement surface. Decrease in the λ_1 and λ_2 values also serves to make the material behave stiffer. λ_1 has an effect on the model response only at the very beginning of compaction. Even at the initial stages the influence of λ_2 is just as significant thereby drawing attention towards observing their response through all compaction stages. Thereafter we observe the

response to change in λ_2 to be dominant as is the case in SGC compaction. Now referring to Figure 73 we notice the regions of parameter influence for the SGC. This observation is useful for us to draw generalized correlations between the material response expected in SGC compaction modelling and the field compaction using the present model. From Figure 71 it is observed that the increase in q_2 results in the pavement responding significantly differently than when q_1 is increased individually. This points towards q_2 being the control parameter in a nonlinear transition of the material from the initially loose mix in the forward pass to a stiffer mix in the return pass. The lesser the magnitude of q_2 the lesser the permanent compaction achieved. It is also interesting to note that the pavement exhibits relaxation mechanism as evidenced in Figure 71 and Figure 72. Note that the material is again compacted on the return pass, midway through the total number of time steps.

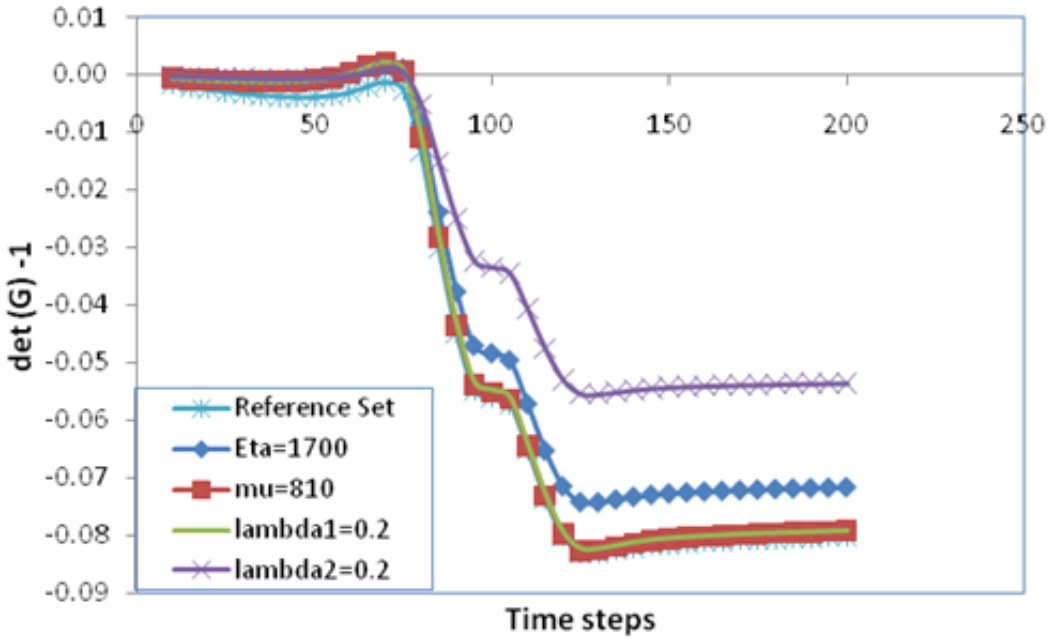

Fig. 71.: Evolution of the volumetric viscous gradient with change in values of individual parameters $\hat{\mu}$, $\hat{\eta}$, λ_1 and λ_2

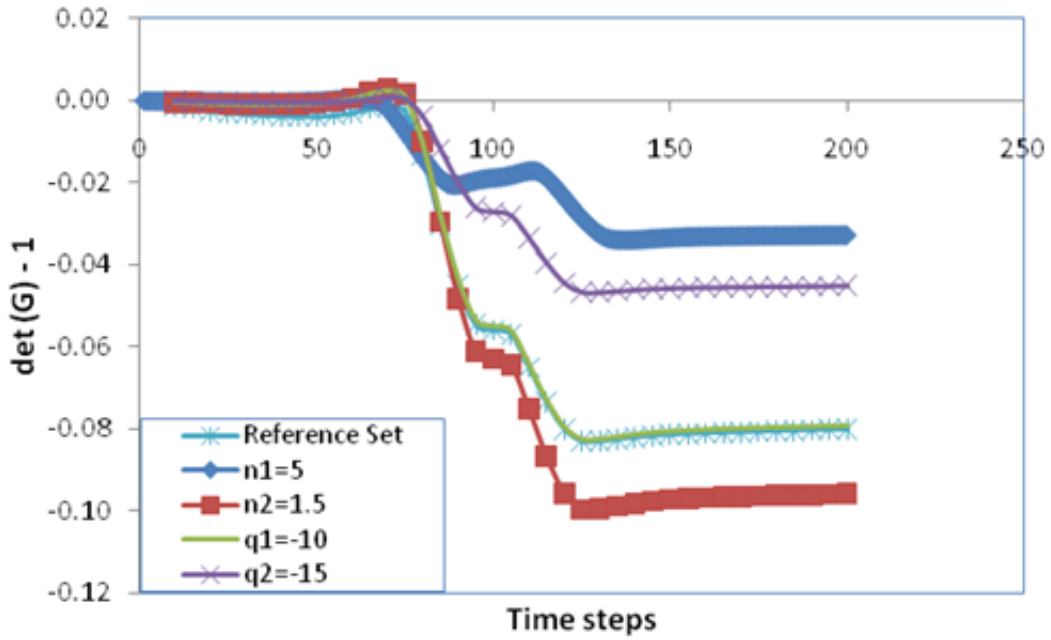

Fig. 72.: Evolution of the volumetric viscous gradient with change in values of individual parameters n_1, n_2, q_1 and q_2

2. Parametric Analysis

We first focus our efforts in determining the behavior of the parameters ascertained as insignificant during the SGC simulation. These parameters are: λ_1 , q_1 and n_2. A number of simulations were performed at different stiffness's (different and) wherein we vary each individual parameter of interest and study its effect on key material responses. These results are presented in Figure 74 through Figure 79. As before we select a reference parameter set (same as the one select for the sensitivity analysis) to compare model response against. We shall again focus on the evolution of the viscous deformation (det**G**-1).

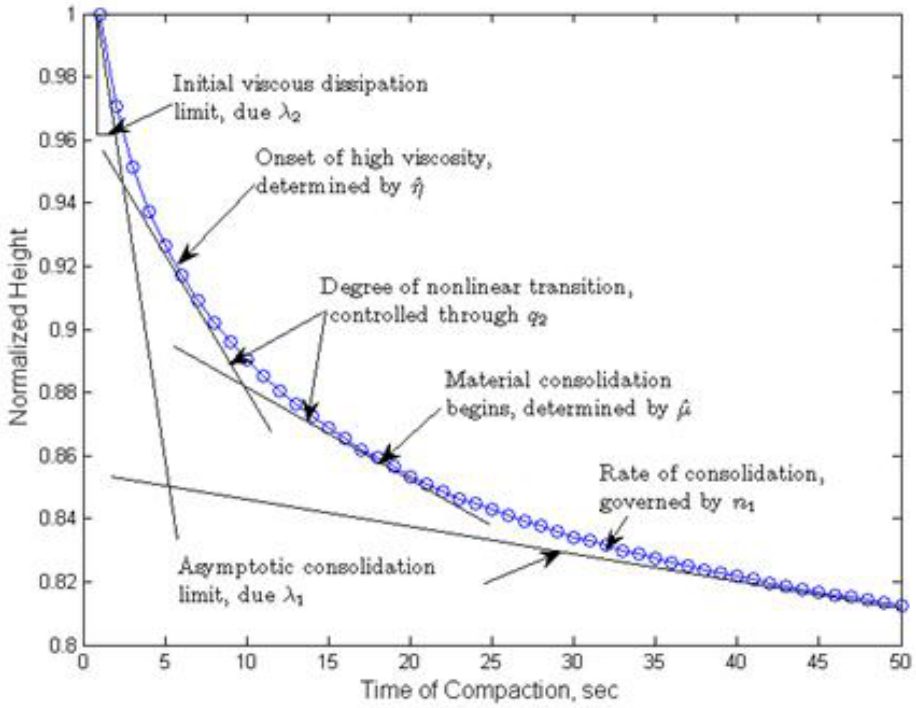

Fig. 73.: Regions of influence of model parameters in gyratory compaction (from Masad et. al. [3])

3. Correlation with Laboratory Compaction

We seek to draw correlations between the behavior of model parameters in the case of the SGC simulation and their behavior during the simulation of field compaction.

1. The profiles of the deflection and volumetric part of viscous evolution indicate that the model response is not sensitive to λ_1 (Figure 74) and hence we can treat the parameter to be a model constant.

2. We can therefore choose λ_1 to be the same constant as in the SGC simulations.

3. The response observed from varying q_1 indicates that the model is sensitive to this parameter as evidenced by Figure 72 and Figure 75. As can be observed, the volumetric part of the viscous evolution exhibits no sensitivity to q_1.

4. Owing to the response exhibited by the model to q_1, in terms of the thermodynamic quantity $\det\mathbf{G}$, we can now consider q_1 a model constant. We can therefore choose it to be the same constant as in the SGC simulations.

5. It is evident from Figure 72 and Figure 76 that the model exhibits considerable sensitivity to changes in n_2. This response of the model shows deviation from the response exhibited by the model during the simulation of the SGC.

6. n_2 is understood to be related to the model's initial rate of dissipation (at the low viscosity, loose mix stage of the compaction). The significance of n_2 for field compaction is attributed to the unbounded nature of the pavement being simulated. This causes the material, in the loose mix state, to be more sensitive to applied stresses as compared to the case of the material being in a confining mould in the SGC.

7. n_2 is to be calibrated from available field data.

8. Figure 77, Figure 78 and Figure 79 indicate that the significant parameters in the SGC simulation also are significant for Field compaction.

9. However, it is prudent to bring to notice the behavior of the parameter n_1. While $n_1 \leq 4.0$ the model does not exhibit any sensitivity to this parameter (Figure 79) whereas at a higher value of, say, 5.0 the model exhibits significantly higher stiffness as evidenced by Figure 72 and Figure 79.

10. Hence, we establish that a correlation exists in parametric behavior for both the compaction processes.

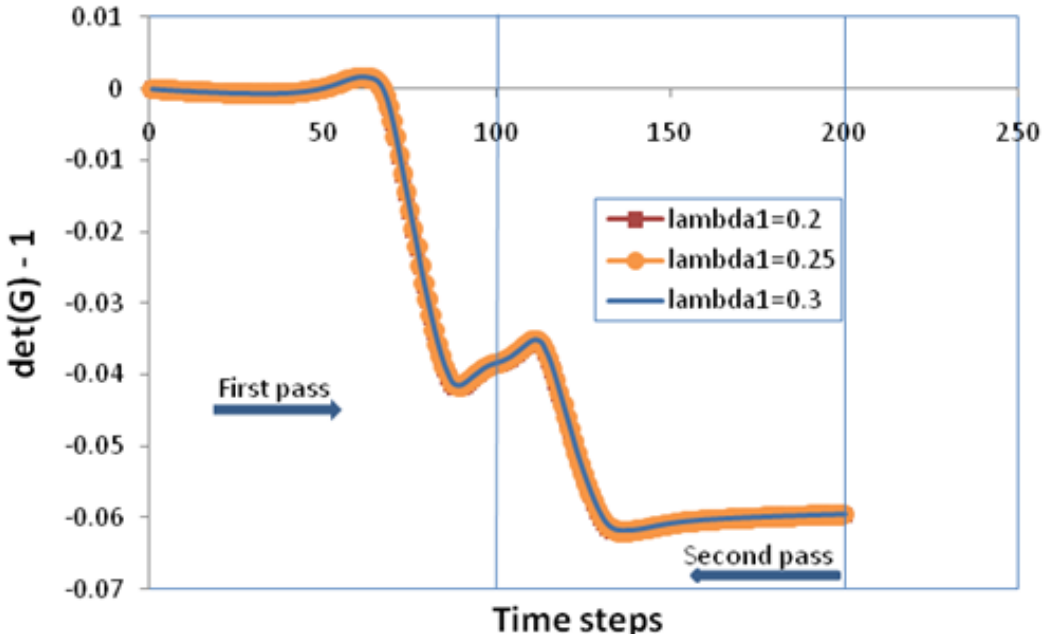

Fig. 74.: Evolution of the volumetric viscous gradient with change in λ_1

B. Analyzing Longitudinal Joints

It has been noted that asphalt pavement close to the longitudinal joint tends to be less compacted than toward the center of the pavement ([11]). This is understood to

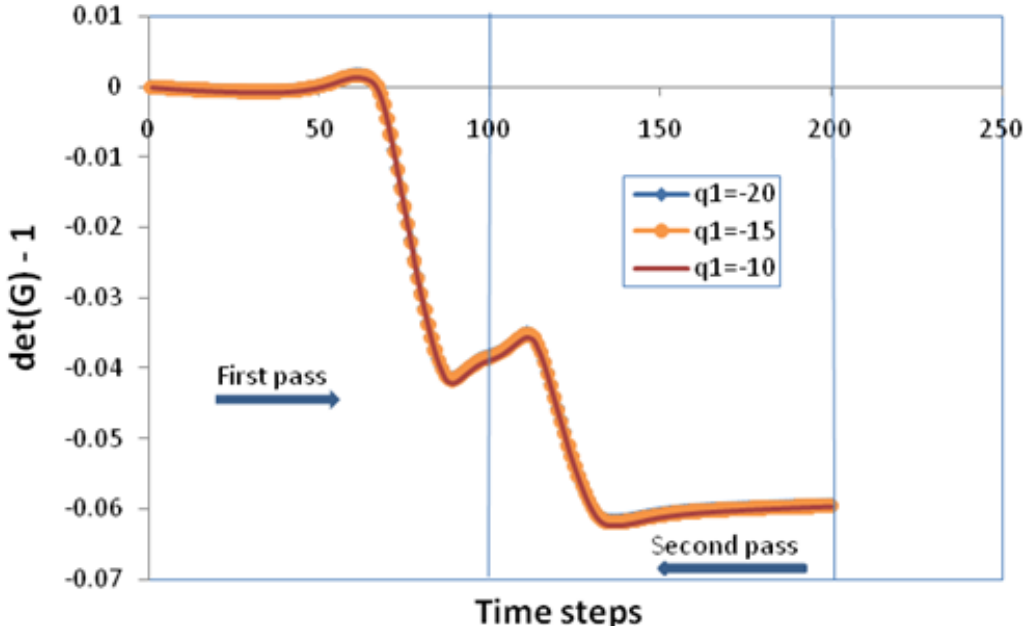

Fig. 75.: Evolution of the volumetric viscous gradient with change in q_1

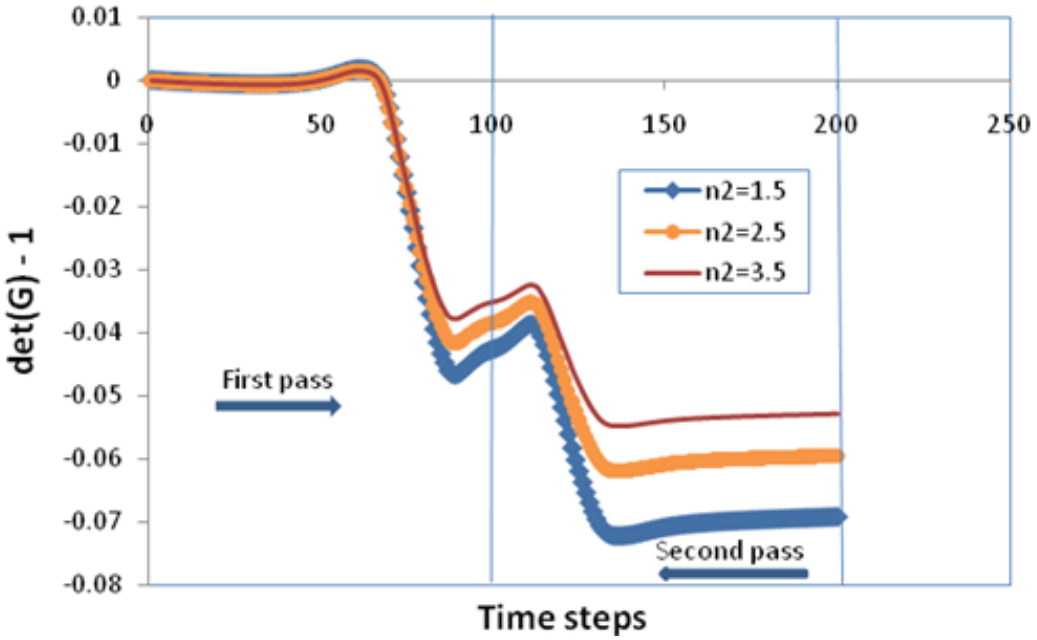

Fig. 76.: Evolution of the volumetric viscous gradient with change in n_2

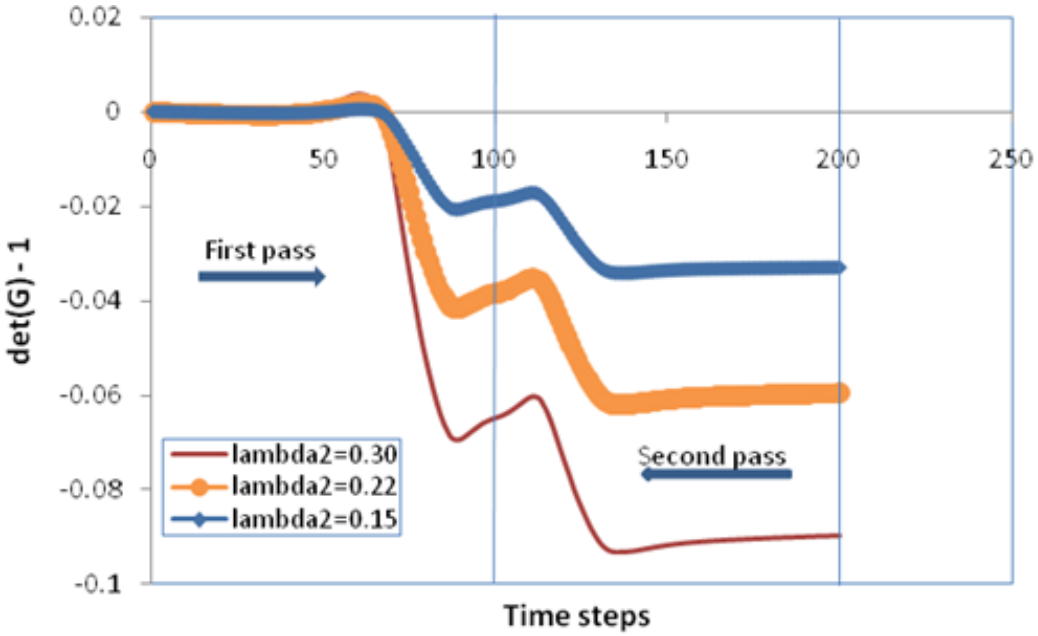

Fig. 77.: Evolution of the volumetric viscous gradient with change in λ_2

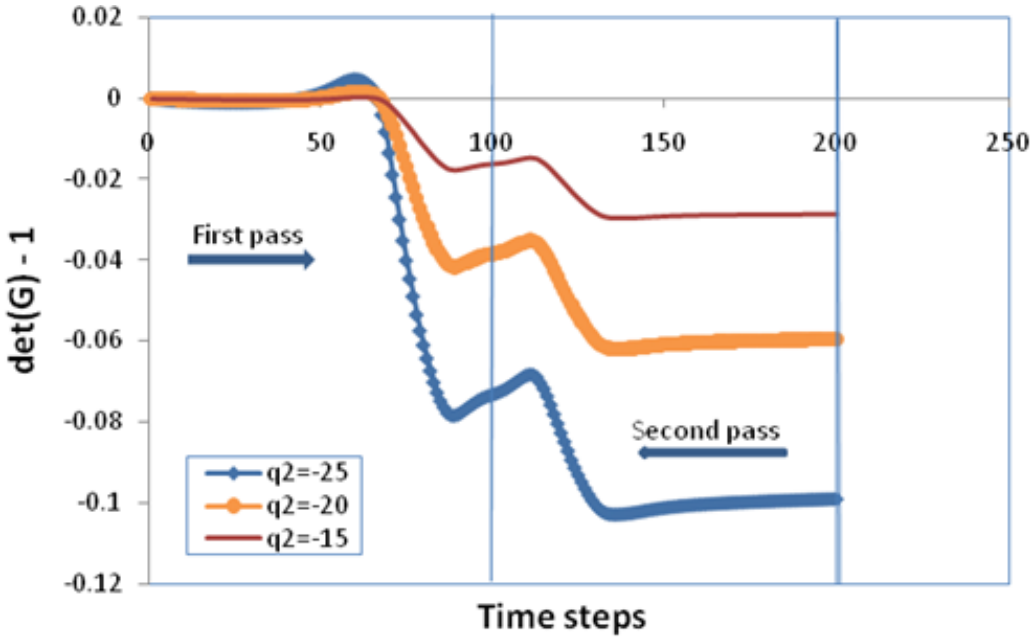

Fig. 78.: Evolution of the volumetric viscous gradient with change in q_2

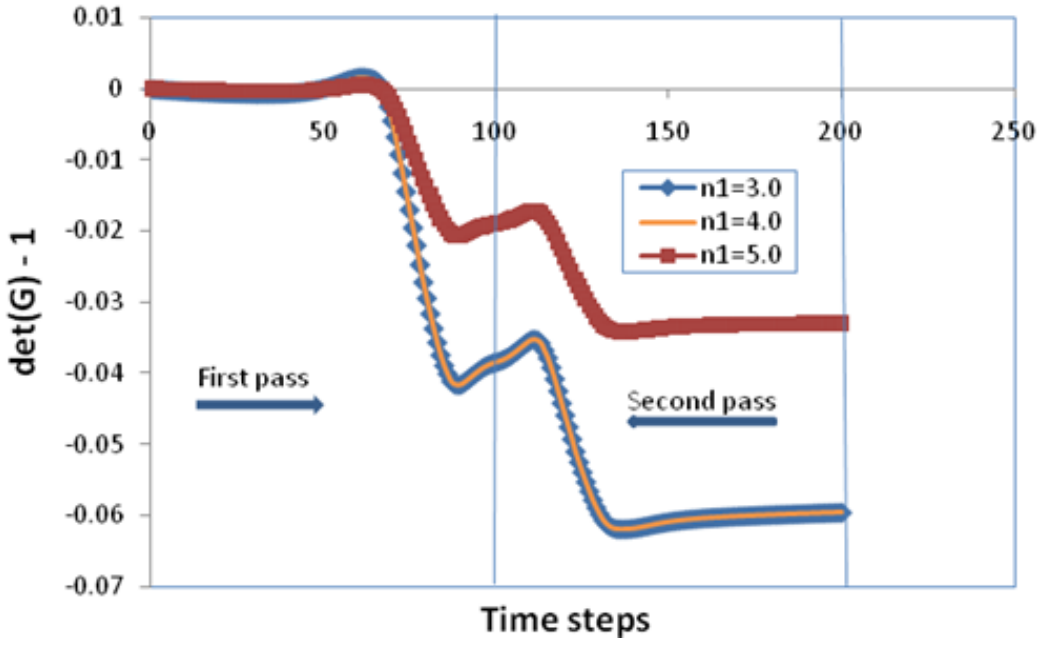

Fig. 79.: Evolution of the volumetric viscous gradient with change in n_1

be due to the tendency to apply fewer passes at the joints. The low confinement at some types of joints (unrestricted or unconfined joints) and the higher rate at which the mixture at the joint loses heat reduce the efficiency of compaction at the joint compared with the pavement center. Here, the compaction of longitudinal joints is studied by simulating the process using the model developed in finite elements. Finite element simulations were conducted to the study the effects of longitudinal joints on compactability. A schematic diagram showing the boundary conditions that are to be applied on the edges that have been fixed and the edges that have been unrestrained along with the longitudinal joints of the pavement has been presented in Figure 42. The restrained edges and unrestrained edges are chosen so as to simulate the response observed in the field as noted above. The fixed edges represent the inner edge of a lane while the unrestrained edge represents the outer free edge of the lane being compacted.

We note that the model predicts a higher level of compaction close (0.5 ft) to the fixed edge of a lane. The compaction predicted at the outer part of the lane, close to (0.5 ft) the unconfined/free edge, is significantly lower owing to the lack of a confining pressure close to the edge. The overlap zone between two roller passes contains the longitudinal joint where material shoving occurs to accommodate the compaction of the material. This kind of behavior is observed in the field as well and is depicted in the plot shown in Figure 80 of the simulation results.

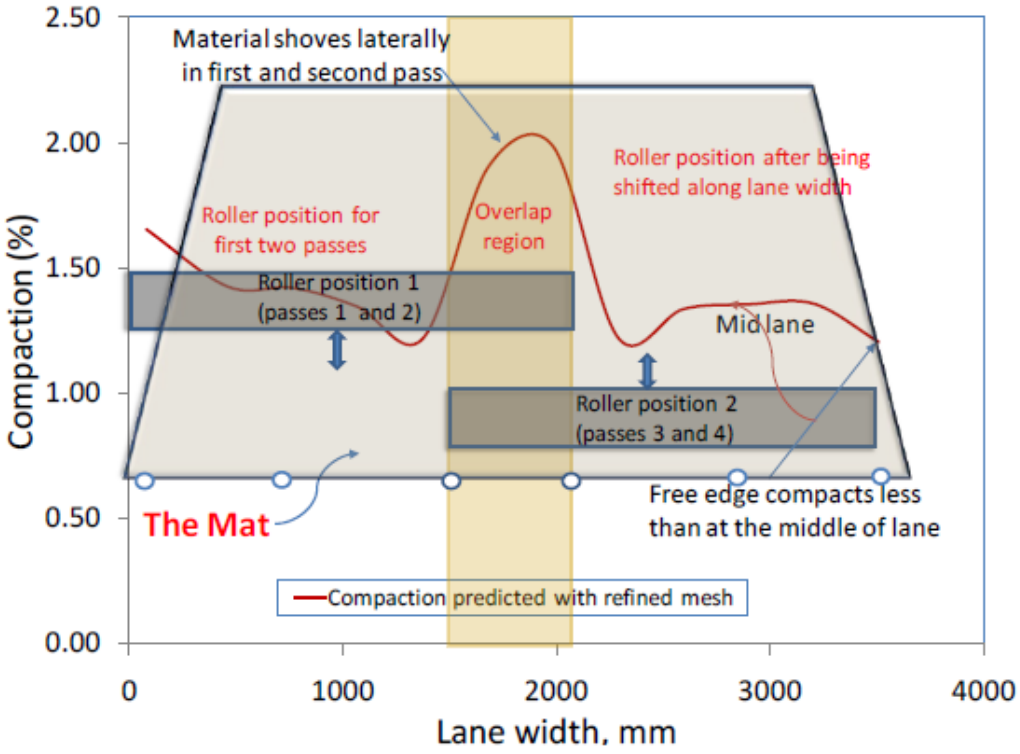

Fig. 80.: The plot represents the final compacted state of the material along the width of the pavement. Observe that the material compacts less at the free edge than at the mid-lane segments close the free edge, this agrees with the observations in the field

C. Model Verification

The model was used to simulate the field compaction of three projects.

1. SH 21

A section of SH 21 was compacted using a vibratory roller compactor to provide data for preliminary evaluation of the model developed in this study. The compactor had two steel drums with a width of 7 ft and a distance of 12 ft between the centers of the drums. The total weight of the roller was 27,783 lb; the front drum had a weight of 13,980 lb and the back drum had weight of 13,803 lb. The roller was operated in vibration mode with about 3000 vibrations per minute and at a speed between 2 to 3 miles per hour.

The finite element model is used to simulate field rolling compaction on a mat of width 12 ft with the roller centered on the mat as shown in Figure 81. The properties of the various layers in the finite element model are presented in Masad et.al. [3]. The measured percent air voids and therefore the change in percent air voids are represented in Figure 82 and Figure 83 respectively. A comparison of the typical simulated response (Figure 67, Figure 68 and Figure 69) in using the finite element model shows that that the model developed does predict a similar trend of compaction over multiple passes as those measured in the field.

In order to further examine the utility of the model in simulating field compaction trends we simulate field rolling compaction matching the rolling patterns in two highway projects, a US 87 paving job near Port Lavaca in Calhoun County, Texas in October 2006 and a section of US 259, located in Rusk County, Texas in February 2007 (see Kassem [11]). The simulation results are compared against the compaction data from the two field compaction projects. The specimens from both projects were

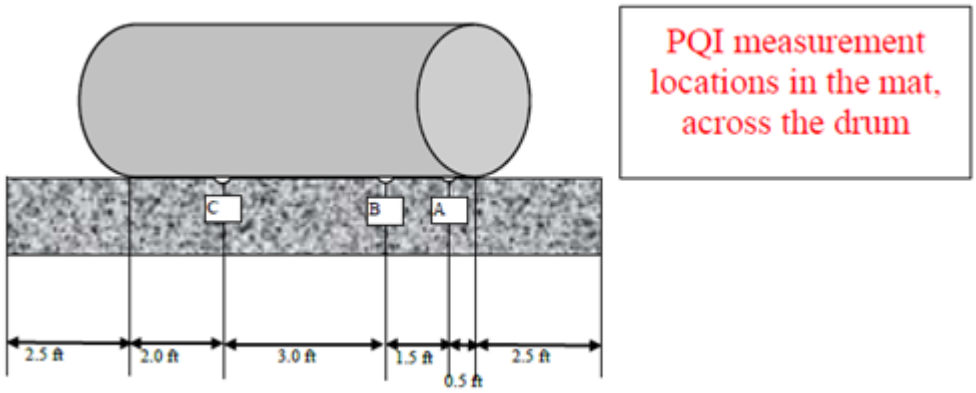

Fig. 81.: A schematic of a roller on a mat with 3 locations for PQI measurements annotated (taken from Masad et. al. [3])

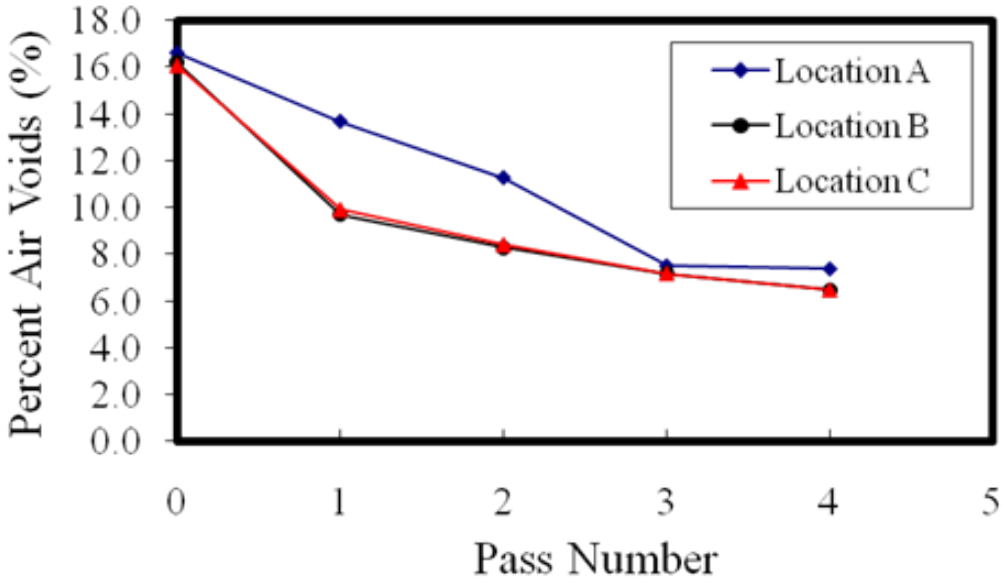

Fig. 82.: Measurements of percent air voids in a mat (as reported in Masad et. al. [3])

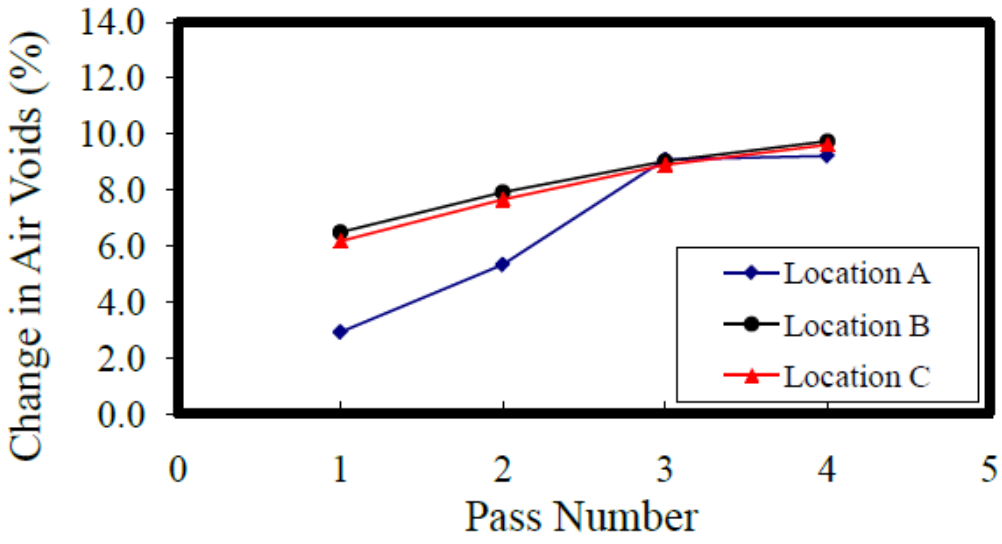

Fig. 83.: Measurements of change in percent air voids in a mat (as reported in Masad et. al. [3])

obtained from wheel path, between the wheel path, and the longitudinal joint (restrained and unrestrained). The asphalt mixtures and compaction data obtained are part of a study funded by the Texas Department of Transportation (TxDOT) in order to evaluate the influence of various field compaction methods on asphalt mixture properties. Table IX and Table X include further information about the asphalt mixture designs and material constituent properties. Aggregate characteristics (angularity, texture and sphericity) were measured using the Aggregate Imaging System (AIMS). Higher numbers reported in Table X for angularity and texture indices mean higher aggregate angularity and texture. Higher sphericity values indicate that particles are less flat and elongated (a sphere has a value of 1).

Table IX.: Summary of mixture designs. *Note*: AC = Asphalt content, Gmm = Maximum specific gravity, VMA = Voids in the mineral aggregate

Highway Project	Mixture Type	Aggregate Type	Binder Grade	AC (%)	G_{mm}	VMA	Design Air Voids,(%)
US 87	Type C	Siliceous River Gravel	PG 76-22S	4.3	2.439	13.8	4.0
US 259	Type C	Sandstone and Limestone	PG 70-22S	4.3	2.478	13.1	3.0

Table X.: Summary of properties of mixture constituents

Highway Project	Binder Viscosity, Pa.s (275°F)	Texture Index	Angularity Index	Aggregate Sphericity
US 87	2.258	112	3062	0.651
US 259	0.818	189	2791	0.618

2. US 87

US 87 is a four-lane divided highway. The test sections were located on northbound outside lane. The mixture was Type C (TxDOT 1993 Specification) designed with Fordyce Gravel and Colorado Materials limestone screening with 4.3 percent PG 76-22s binder. Type C mixture is similar to coarse graded SUPERPAVE mixture. The Type C mixture was laid on a Type B mat, which primarily included crushed river gravel. The thickness of the Type C layer was 2 inches (5 cm). The mixture was laid with a 16 ft (4.8 m) mat width with 1.5 ft (45 cm) on one side being tapered. The structure of the pavement for the US 87 pavement project is presented in Figure 84, the layer properties are given in Table XI and the width of the top layer mat is indicated in Figure 85. The general rolling pattern can be described as breakdown by steel wheel vibratory roller and pneumatic wheel roller for both intermediate and finish rolling. In addition, the rolling pattern consisted of progressively moving the vibratory steel wheel roller in transverse directions with the pneumatic wheel roller again acting as both intermediate and finish roller. The sequence and location of the roller is simulated approximately along with the boundary conditions representative of the restrained and unrestrained edges of the pavement. The sequence and location of rollers are indicated by the bars in the schematic in Figure 85. In the schematic the inner edge of a lane is indicated by the vertical dotted line passing through 0. The roller locations are represented with respect to this line as the datum to measure distance. The rolling pattern and the measured percent air voids (% AV) are presented in Table XII.

Some interesting observations can be made when studying the response of the material as the mat is subject to different roller passes. From Figure 86 (and knowing the roller patterns from Table XII) we can make the following observations for the

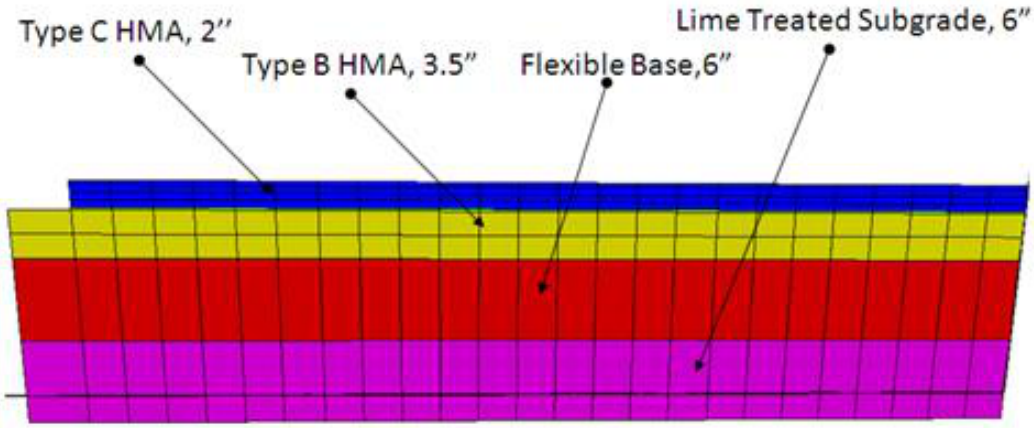

Fig. 84.: Pavement structure for US 87 project

Table XI.: Material properties used for the US 87 project

Layer	Modulus, **E** psi	Poisson Ratio, ν
2.0 inch Type C HMA	Refer Table XVII	–
3.5 inch Type B HMA	375,000	0.30
6.0 inch flexible base	30,000	0.35
6.0 inch lime treated subgrade (5% lime)	12,000	0.45

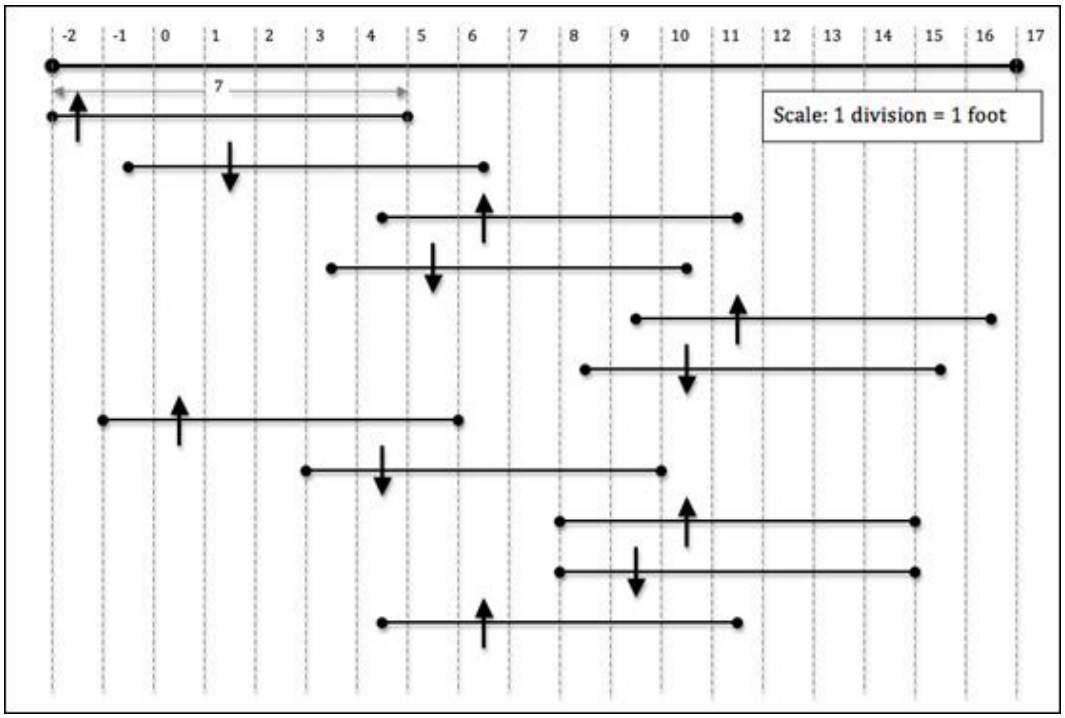

Fig. 85.: Schematic for the rolling patterns for US 87 project. The line segments represent rollers with their rolling directions. The arrows indicate the direction of rolling: upward arrow indicating forward rolling and downward arrow the reverse

Table XII.: Rolling pattern, % AV measured in the field for US 87 project. *Note*: The total number of passes of the compaction process involving the vibratory roller is 11, with 9 of them being in vibratory mode and 2 in static mode

Core Group	Distance from the edge, ft	Rolling Pattern		% AV
		Vibratory Roller		
		Vibratory mode	Static mode	
1	1	3	1	9.65
2	4	5	1	6.77
3	7	3	1	7.33
4	10	6	2	5.01

material behavior of US 87 pavement undergoing compaction:

- Core Group 4 receives more passes and accordingly undergoes most compaction.
- Core Groups 1 and 3 receive the same types of load and the same number of passes; however, Group 3 undergoes more compaction. This is attributed to the rolling pattern chosen for this project which subjects the material in this region to more 'overlapping loads' by virtue of its centralized location along the mat width.
- Core Group 2 undergoes compaction that is in between Group 4 and Groups 1 and 3.

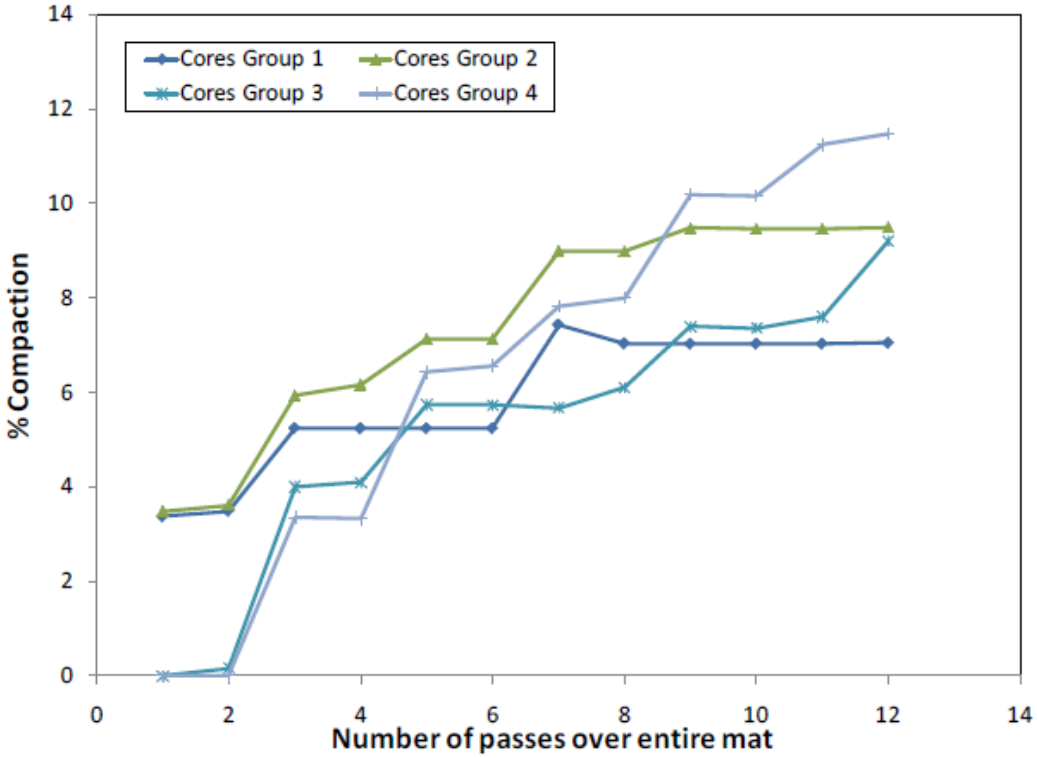

Fig. 86.: Prediction of % Compaction per roller pass across the mat (cores taken at 4 locations), for US 87

3. US 259

The overlay in the US 259 project used a Type C surface mixture compacted in 2 inch (5 cm) lift thickness. The coarse part of the aggregate used was sandstone while the intermediate and fine size particles were limestone. The mix had 11 percent field sand and 4.3 percent PG 70-22S binder. The test sections were in the southbound outside lane. Type C mix was laid on top of recently compacted Type D level-up course, where Type D mixture is similar to a SUPERPAVE fine graded mixture. The paving width was approximately 15 ft (4.57 m) (including shoulder) and a vertical longitudinal joint was maintained. The structure of the pavement for the US 259 pavement project is presented in Figure 87, the layer properties are given in Table XIII and the width of the top layer mat is indicated in Figure 88. The sequence and location of rollers are indicated by the bars in the schematic in Figure 88. In the schematic the inner edge of a lane is indicated by the vertical dotted line passing through 0. The roller locations are represented with respect to this line as the datum to measure distance. The rolling pattern and the measured percent air voids (% AV) are presented in Table XIV.

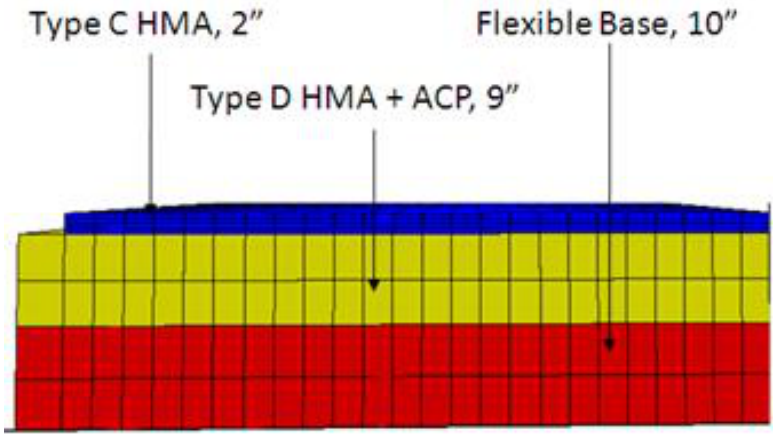

Fig. 87.: Pavement structure for US 259 project

Table XIII.: Material properties used for the US 259 project

Layer	Modulus, **E** psi	Poisson Ratio, ν
2.0 inch Type C HMA	Refer Table XVII	–
1.25 inch Type D level–up	450,000	0.30
1 layer seal coat treatment	–	–
7 to 8 inch ACP	400,000	0.30
10 inch flexible base	34,000	0.35

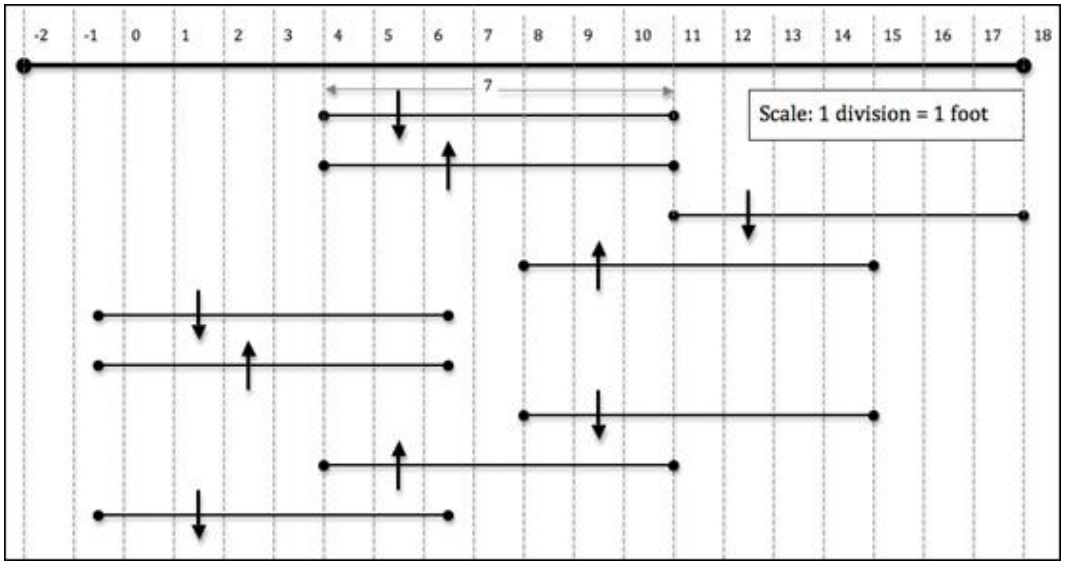

Fig. 88.: Schematic for the rolling patterns for US 259 project. The line segments represent rollers with their rolling directions

Table XIV.: Rolling pattern, % AV measured in the field for US 259 project. *Note*: The total number of passes of the compaction process involving the vibratory roller is 9, with 5 of them in vibratory mode and 4 in static mode

Core Group	Distance from the edge, ft	Rolling Pattern		% AV
		Vibratory Roller		
		Vibratory mode	Static mode	
1	1	1	2	11.26
2	5	3	3	7.7
3	8	3	2	8.12
4	11	2	2	10.78
5	14	2	1	9.27

From Figure 89, we make the following observations for the compaction response of the pavement material for US 259:

- Group 2 is subject to most vibratory and static load passes and is centrally located hence undergoes the most compaction.
- Group 1 is subject to rapid compaction when static rollers are brought on after it is subject to only 1 vibratory loading.
- Groups 4 and 5 are influenced by the same number of vibratory loads with Group 5 subject to less static loads. However, we observe that Group 5 achieves more compaction. This is in agreement with the field compaction as evidenced by the % AV for Groups 4 and 5 in Table XIV.
- Group 3 undergoes a uniform (in terms of the % compaction per pass) due to

the vibratory loads and less (compared to Group 2) static loads and also due to its central location in the mat.

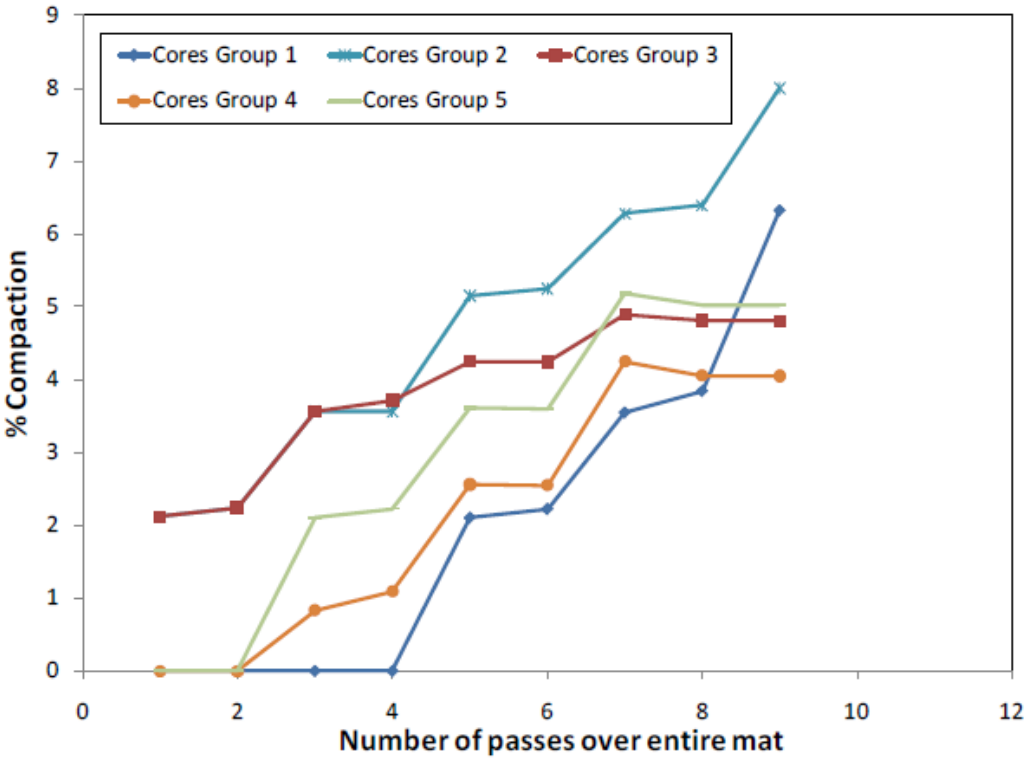

Fig. 89.: Prediction of % Compaction per roller pass across the mat (cores taken at 4 locations), for US 259

4. Observations from Field Compaction Simulations for US 87 and US 259

As in actual field compaction the initial Air Voids generally vary between 15-20 % of volume of the mix , the measured % AV are adjusted by using these two different initial AV values to calculate the 'change in measured % AV', which is more indicative of the compaction the material has experienced. These 'change in measured % AV' values are then compared directly against the % Compaction values predicted by the finite element model (see Table XV and Table XVI). A 'compaction zone' is enclosed

by the use of two initial % AV values as indicated in Figure 90 and Figure 91, wherein the measured and calculated % Compaction at different location across the mat are compared at the end of rolling pattern cycles.

The % Compaction values are calculated using parameters from SGC compaction of these two mixes as well as field adjusted parameters. The compaction predicted by the SGC parameters is outside the range of the change in % AV measured in the field (Figure 90 and Figure 91). Therefore, the parameters are adjusted so that the compaction obtained in simulations is contained within the range of measure % AV values. The parameters used for the simulation purposes are indicated in Table XVII. From Figure 90 and Figure 91 we can observe that within the 'compaction zone', the behavior of the mix in our simulations correlates well with the trends observed in the field. The type of compaction in each project (based on the combination of type of roller and the rolling pattern) correlates directly to the measured change in % AV for the corresponding 'Core Groups' (see Table XV and Table XVI). The more the measured change in % AV more is the compaction undergone at that location. This behavior is reflected in Figure 90 and Figure 91, for simulations of both projects and in that sense agree with reality.

The simulation model is capable of providing further insight into field compaction trends when using the measured % AV to gauge material response. As can be seen in Figure 92 (where we compare the response of two materials at the same location, relative to the edge of the mat) the simulations predict that US 87 material will undergo more compaction by the end of the whole process than the US 259 pavement. This is in direct correlation to the higher 'change in measured % AV' for the US 87 pavement (Table XV, Core Group 1) as compared to the 'change in measured % AV' for the US 259 pavement (Table XVI, Core Group 1).

Therefore, in conclusion we observe that the compaction observed across the

Table XV.: Change in measured % AV in the field and calculated % Compaction for US 87 project

Core Group	Change in % Air Voids		Compaction, using SGC parameters (%)	Compaction, using field parameters (%)
	15% Initial Air Voids (I.A)	20% Initial Air Voids (I.A)		
1	5.35	10.35	3.52	7.50
2	8.23	13.23	5.17	10.39
3	7.67	12.67	4.42	9.49
4	9.99	14.99	6.04	12.83

Table XVI.: Change in measured % AV in the field and calculated % Compaction for US 259 project

Core Group	Change in % Air Voids		Compaction, using SGC parameters (%)	Compaction, using field parameters (%)
	15% Initial Air Voids (I.A)	20% Initial Air Voids (I.A)		
1	3.74	8.74	4.02	7.48
2	7.30	12.30	5.92	10.95
3	6.88	11.88	3.36	7.25
4	4.22	9.22	2.64	5.28
5	5.73	10.73	3.26	7.22

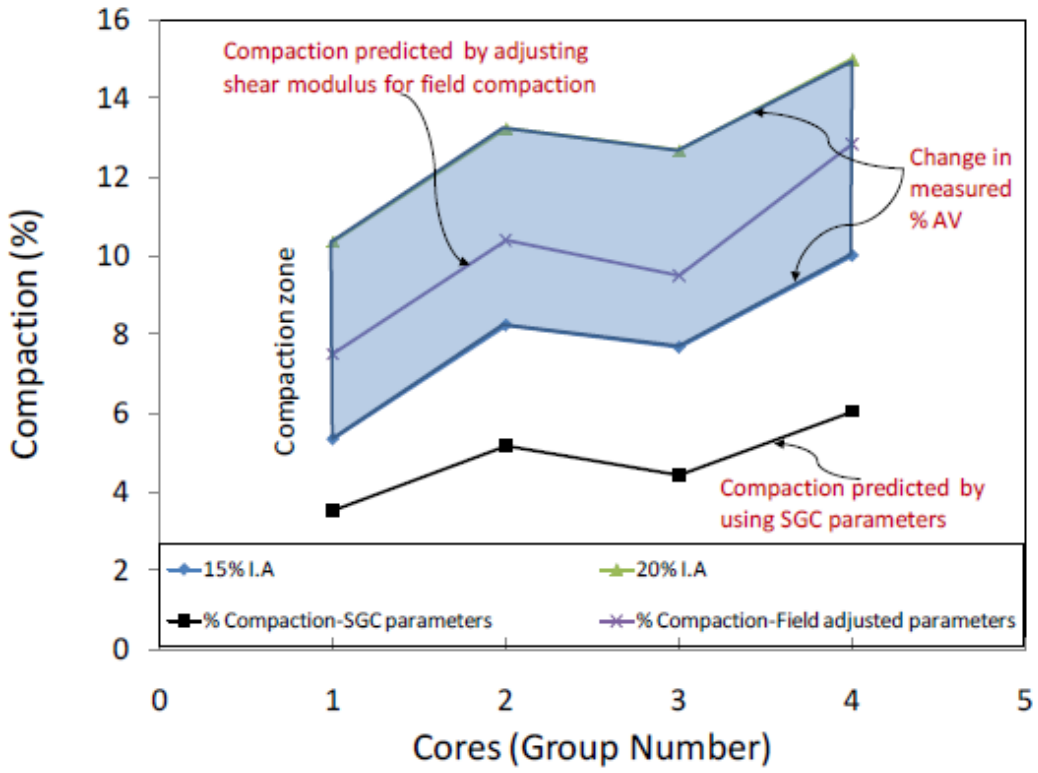

Fig. 90.: Comparison of the total % Compaction from simulations with the general trend of the % AV measured at the end of the field compaction process for US 87. The comparison is made per core group, which represents a different location across the mat relative to the edge (see Table XII and Table XV)

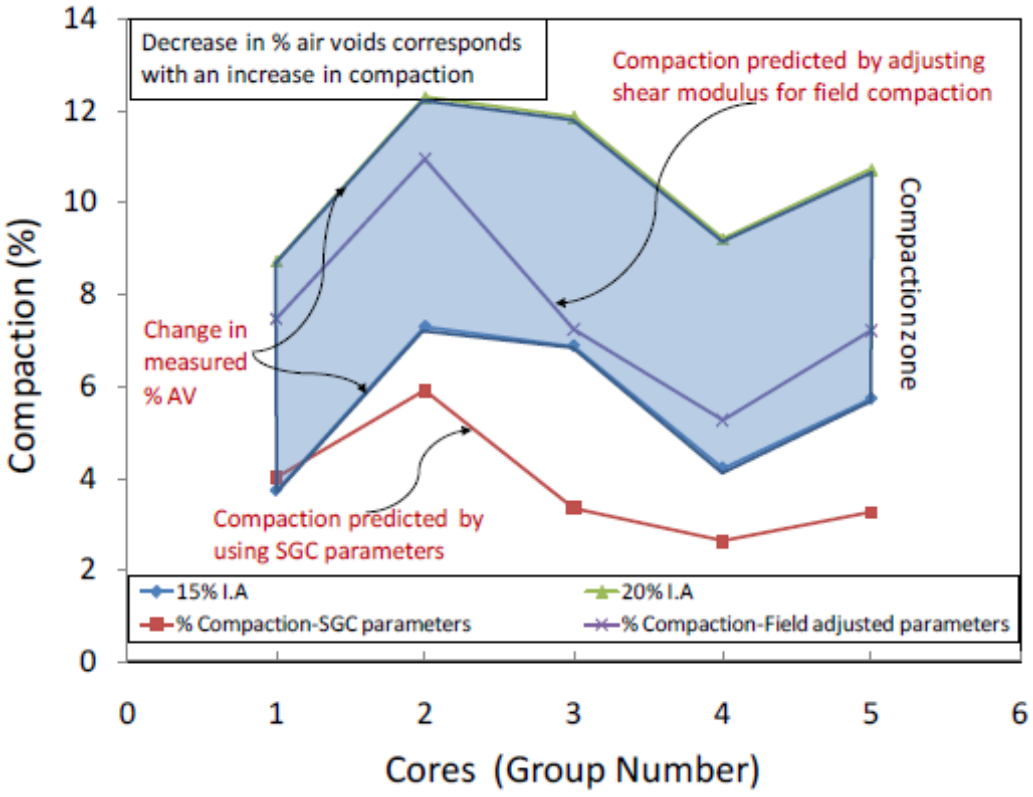

Fig. 91.: Total % Compaction from simulations compared with the general trend of the % AV measured at the end of the field compaction process for US 259. The comparison is made per core group, which represents a different location across the mat relative to the edge (see Table XIV and Table XVI)

Table XVII.: Model parameters used for the two projects, US 87 and US 259

Highway projects	Parameter sets	$\hat{\mu}$ (MPa)	n_1	λ_1	q_1	$\hat{\eta}$ (MPa.s)	n_2	λ_2	q_2
US 87	SGC	2600	5	0.25	-25	2100	2.5	0.26	-27
	Field adjusted	2300	5	0.25	-25	2100	2.5	0.26	-27
US 259	SGC	2400	5	0.25	-25	1700	2.5	0.21	-28
	Field adjusted	2150	5	0.25	-25	1700	2.5	0.21	-28

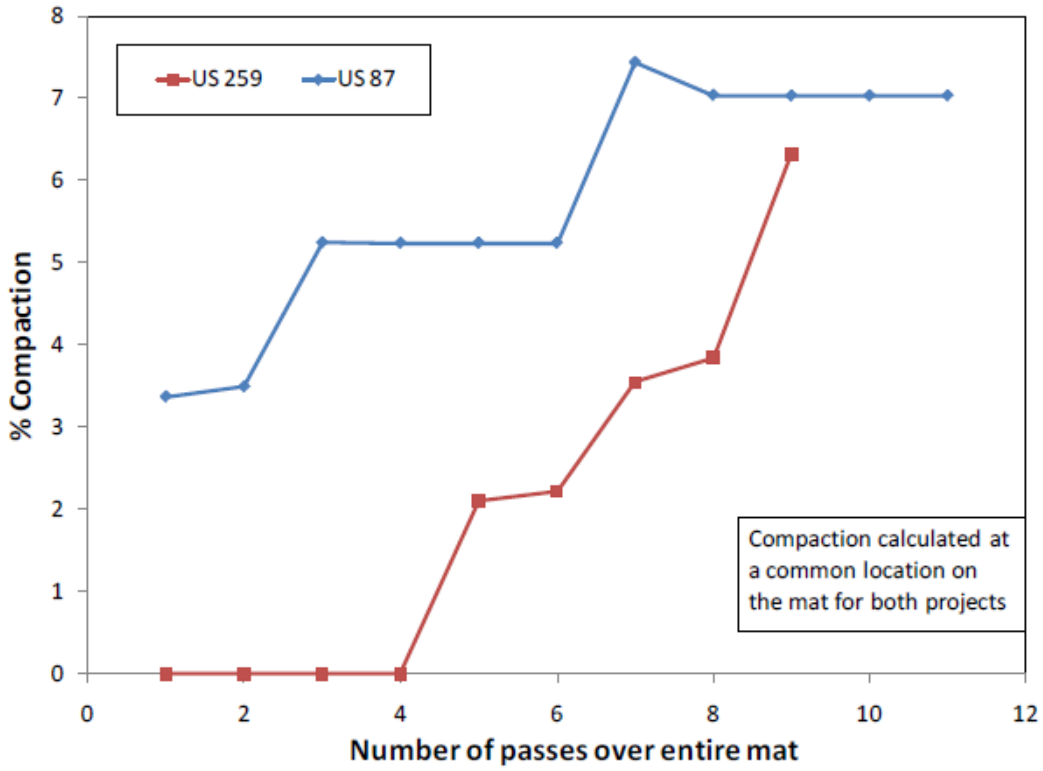

Fig. 92.: Comparison of prediction of % Compaction per roller pass, between US 87 and US 259. The calculations recorded here correspond to Core Group 1 in Table XV and Table XVI, i.e., taken at a distance of 1 foot from the edge

pavement over the different roller passes correlates with the compaction measured (through a change in percent air voids) in the field. The compaction simulation using model parameters from the gyratory compactor simulations is observed to be similar to the measured values. These parameters, with a simple shift in one of the parameter values ($\hat{\mu}$), can therefore be used to predict field compaction, thereby allowing for a correlation between laboratory and field compaction simulations. A 'compaction zone', characteristic of each mix type can thereby be predicted. Applying vibratory mode loads initially causes a more uniform (in terms of the % compaction per pass) compaction. It can be observed that the rolling patterns and load locations are of utmost importance in determining the amount and type of compaction (more uniform or less uniform), Figure 92, Figure 86 and Figure 89. The simulation model provides us with an opportunity to experiment with different rolling patterns to achieve a specific % Compaction or a certain trend in the uniformity of compaction from pass to pass. There is considerable variability in the compaction trends that one needs to be aware of. This has been evidenced here through the study of 2 projects. The variability in trends owing to loading patterns is a natural reflection of the non-linear nature of the materials employed. Only vibratory and static wheel loads have been considered in this study and the simulation of finish rolling through use of pneumatic rollers was not considered.

CHAPTER VIII

SUMMARY AND CONCLUSIONS

The main reasons for the selection of the thermodynamics based compressible viscoelastic model are as follows:

- The compaction process involves large strains which can be modeled using the thermodynamic framework adopted.
- The material goes through significant micro-structure changes during the compaction process. These changes include aggregate re-orientation, reduction in air voids and increase in aggregate contacts. The continuum model is formulated to account for these phenomena through the specification of appropriate evolution functions of the Helmholtz potential and rate of dissipation.
- A few parameters are used in calibrating the model. These parameters are the ones used in determining the evolutions of Helmholtz potential and rate of dissipation.
- The limited number of model parameters makes it possible to relate these parameters to mixture design and properties.
- Continuum models similar to the one that is developed in this study have been used successfully in modeling asphalt material behavior under complex loading and environmental conditions. It is known that asphalt mix temperature changes during compaction and this phenomenon needs to be accounted for in the model in further work.
- Model's response to applied constant stress and applied constant strain is reflective of what can be expected from a viscoelastic model. In addition, owing to

the compressibility built in, the model lends itself to be employed for modeling permanent deformation as observed during compaction.

A. Finite Element Implementation and Response

- The model is implemented in the finite element code CAPA-3D. The implementation is then validated by comparing the finite element solution for one-dimensional constant stress and constant strain loading with the corresponding solutions from analytical techniques (aid by calculations using MATLAB).

- The model is shown to exhibit nonlinear response in shear, through the exhibition of normal stress differences.

- The continuum model has been used for implementation in the finite element method in order to simulate the compaction process under various conditions. As such, it can be used to relate the laboratory compaction process to the field compaction process. It can also be used to understand the intelligent compaction process by constructing a three dimensional model of asphalt pavements subjected to rolling action.

- Some of the basic tools and techniques for the development of the continuum models are already available and have been exploited to refine the model and make it amenable for further study. Adapting numerical tools like the finite element method (CAPA-3D) to provide solutions to the complex model equations subject to varied boundary conditions presents a challenge. Such a challenge forms an integral part of this dissertation and an effort is made to simulate gyratory and field compaction precesses using the implementation developed thus far.

B. Gryatory Compaction

The finite element method was used to simulate the laboratory compaction of asphalt mixtures. The main findings of the simulation of the gyratory compaction study are as follows:

- The parametric analysis conducted in this study showed that the compaction process is insensitive to changes in some of the model's parameters. Therefore, it was decided to use constant values for these parameters during all the finite element simulations in order to simplify the process of finding the values of the remaining parameters. However, the model needs to be further examined for other processes in which these parameters might be of significance.

- The parametric analysis demonstrated that some of the model's parameters are related mostly to the initial stage of compaction when the material exhibits low viscosity fluid-like behavior, while some parameters are related to the behavior of the mixture after it starts to exhibit a high viscous fluid-like behavior and compaction rate decreases.

- A systematic method was developed to determine the model's parameters from the Superpave gyratory compaction curves. It was necessary to develop this method owing to the difficulty of conducting conventional tests (e.g. triaxial or shear tests) to determine the model's parameters given the high compaction temperatures.

- The finite element simulations demonstrated the capability of the constitutive model to simulate the Superpave gyratory compaction process at different compaction angles.

- The developed model and finite elements implementation will allow predicting the mixture compactability in the field based on laboratory measurements. It will also allow studying the influence of changes in material properties and mixture designs on the mixture compactability under various laboratory and field conditions.

C. Field Compaction

A finite element model for simulation of asphalt compaction in the field. The details of the finite element model with regards to the mesh, geometry, loading methodology and boundary conditions have been presented. The primary findings of the study of the field compaction through numerical means are as follows:

- A loading algorithm is developed for use in CAPA-3D for pavement compaction simulations. The loading algorithm utilizes non-uniform pressure loads being applied over the surface of the finite elements in contact with a roller, in order to simulate their interaction.

- Moving loads are applied in a quasi-static manner by incrementally translating the necessary element surface loads during the simulation.

- The vibratory loads are applied in a quasi-static manner as well. The inertial effects of the HMA layer are neglected owing to the short time scale the loading system is active.

- Interface layer elements are utilized to resolve contact issues pertaining to the layer interactions.

- Impedance layers are introduced to the finite element mesh so they can be utilized when simulating true dynamic loads with mass effects being dominant

in the finite element mesh. However, it has been shown that the impedance layers need not be used for the quasi-static type of loading utilized in this study as they do not affect the solution (due to absence of dynamic loads).

- The finite element model developed in this study is capable of capturing the compaction characteristics experienced at the longitudinal joints of a pavement. Also, the compaction characteristics at the fixed/free edges agree with what is commonly observed during practical compaction operations. The fixed longitudinal joints exhibits higher compaction than the free edges as in the field.

- The numerical model validated against data from three highway projects and it agrees well with the general trends of compaction observed in the field. Model parameters have been adapted from those obtained by calibrating the laboratory compaction simulation with the laboratory compaction data. These parameters are then used to obtain a set of parameters, for each mix design, to be used in field compaction simulations. The two sets of parameters for each mix design vary from each other through a single shift in one of the parameters, the shear modulus parameter $\hat{\mu}$.

- The simulation model is demonstrated to be capable of providing insight into which mix design and rolling pattern combination provides more compaction at different location across the mat.

- Finally, a sensitivity and parametric analysis are conducted for completeness and to gauge the structural response of the HMA mat for different parametric sets. It has been found that the parameter sensitivity matches that exhibit in the case of the laboratory compaction simulations as recorded in a previous study, Masad et. al. [3]. There is, however, one parameter (n_2) that needs to

be calibrated with field data. For the purposes of determining what factors influence n_2 , we need to collect and examine more data pertaining to factors influencing field compaction.

D. Recommendations for Future Investigations

The study conducted can be extended further in the following ways:

- The model developed can be used to develop a database of parameters for different mix designs. This database of model parameters can be used for further numerical investigations.

- The model developed and implemented here can be readily modified to include the thermal effects. The non-isothermal model thus developed can be used to study the effect of temperature gradients in the pavements structures on their responses.

- It is suggested that future experimental investigations into compaction of pavements seriously consider the problem of measuring temperature along the length, breadth and depth of pavement layers at different compaction levels. This shall provide adequate data that can be used for refining and improving the efficacy of the theoretical and simulation models for compaction.

REFERENCES

[1] S. Plan, S. Committees, P. Committees, L. Performance, M. Board, T. Coverage, and T. Serials, *Glossary of Highway Quality Assurance Terms*. Washington DC: Transportation Research Board, 2005, vol. 5.

[2] S. Koneru, "A thermodynamic approach for compaction of asphaltic composites," Master's thesis, Texas A&M University, December 2006.

[3] E. Masad, S. Koneru, K. R. Rajagopal, A. Scarpas, and C. Kasbergen, "Modeling of asphalt mixture laboratory and field compaction using a thermodynamics framework," *Journal of the Association of Asphalt Paving Technologists*, vol. 78, pp. 569–606, 2010.

[4] U. S. A. C. of Engineers, *Hot-Mix Asphalt Paving Handbook*. Washington DC: US Army Corps of Engineers, 2000.

[5] F. L. Roberts, P. Kandhal, E. R. Brown, D. Lee, and T. W. Kennedy, *Hot Mix Asphalt Materials, Mixture Design and Construction*. Lanham, MD: National Asphalt Pavement Association, 1996.

[6] A. Institute, *The Asphalt Handbook*. College Park, MD: The Asphalt Institute, 1989.

[7] E. T. Harrigan, R. B. Leahy, and L. S. Youtcheff, "SHRP-A-379: The superpave mix design system manual of specifications, test methods and practices," Strategic Highway Research Program, Washington DC, Tech. Rep., 1994.

[8] I. Abaqus, *Abaqus User's Manual*. Providence, RI: Dassault Systèmes, 2007.

[9] S. F. Brown and M. S. Snaith, "The permanent deformation characteristics of a dense bituminous macadam subjected to repeated loading," in *Proc. Fourth Conference on Structural Design of Asphalt Pavements*. Ann Arbor, MI: University of Michigan, 1978, pp. 225–248.

[10] J. M. Krishnan and K. R. Rajagopal, "Review of the uses and modeling of bitumen from ancient to modern times," *Applied Mechanics Reviews*, vol. 56, no. 2, pp. 149–214, 2003.

[11] E. A.-R. Kassem, "Compaction effects on uniformity, moisture diffusion, and mechanical properties of asphalt pavements," Ph.D. dissertation, Texas A&M University, December 2008.

[12] A. Consuegra, D. N. Little, H. Von Quintus, and J. L. Burati Jr, "Comparative evaluation of laboratory compaction devices based on their ability to produce mixtures with engineering properties similar to those produced in the field," *Transportation Research Record*, no. 1228, pp. 80–87, 1989.

[13] J. Harvey and C. L. Monismith, "Effects of laboratory asphalt concrete specimen preparation variables on fatigue and permanent deformation test results using strategic highway research program a-003: A proposed testing equipment," *Transportation Research Record*, no. 1417, pp. 38–48, 1993.

[14] B. Peterson, K. Mahboub, M. Anderson, E. Masad, and L. Tashman, "Comparing superpave gyratory compactor data to field cores," *Journal of Materials in Civil Engineering*, vol. 16, no. 1, pp. 78–83, 2004.

[15] E. Masad, B. Muhunthan, N. Shashidhar, and T. Harman, "Internal structure characterization of asphalt concrete using image analysis," *Journal of Computing in Civil Engineering*, vol. 13, pp. 88–95, 1999.

[16] L. Tashman, E. Masad, B. Peterson, and H. Saleh, "Internal structure analysis of asphalt mixes to improve the simulation of superpave gyratory compaction to field conditions," *Journal of the Association of Asphalt Paving Technologists*, vol. 70, pp. 605–645, 2001.

[17] H. L. Huerne, "Compaction of asphalt road pavements," Ph.D. dissertation, University of Twente, Enschede, The Netherlands, 2004.

[18] A. R. Lee and A. H. D. Markwick, "The mechanical properties of bituminous surfacing materials under constant stress," *J. Soc. Chem. Ind*, vol. 56, pp. 146–154, 1937.

[19] R. N. J. Saal and J. W. A. Labout, "Rheological properties of asphalts," *Rheology: Theory and Applications*, vol. 2, pp. 363–400, 1958.

[20] R. N. J. Saal, "Rheological properties," in *The Properties of Asphaltic Bitumen: with Reference to its Technical Applications*, J. P. Pfeiffer, Ed. Amsterdam, The Netherlands: Elsevier, 1950, ch. Physical properties of asphaltic bitumen.

[21] C. Van der Poel, "Road asphalt," in *Building Materials: Their Elasticity and Inelasticity*, M. Reiner, Ed. Amsterdam, The Netherlands: North-Holland, 1954.

[22] M. Reiner, *Deformation, Strain and Flow: an Elementary Introduction to Rheology*. New York: Interscience Publishers, 1960.

[23] C. L. Monismith and K. E. Secor, "Viscoelastic behavior of asphalt concrete pavements," in *Proc. International Conference on the Structural Design of Asphalt Concrete Pavements*, Ann Arbor, MI, 1962, pp. 476–498.

[24] K. E. Secor and C. L. Monismith, "Analysis and interrelation of stress-strain-time data for asphalt concrete," *Journal of Rheology*, vol. 8, pp. 19–32, 1964.

[25] C. A. Pagen, "Rheological response of bituminous concrete," *Highway Research Record*, no. 67, pp. 1–26, 1965.

[26] C. L. Monismith, R. L. Alexander, and K. E. Secor, "Rheologic behavior of asphalt concrete," in *Proc. Association of Asphalt Paving Technologists*, vol. 35, Lino Lakes, MN, 1966, pp. 400–450.

[27] S. Huschek, "The deformation behavior of asphalt concrete under triaxial compression," in *Proc. Association of Asphalt Paving Technologists*, vol. 54, 1985, pp. 407–431.

[28] E. F. Davis, E. M. Krokosky, and E. Tons, "Stress relaxation of bituminous concrete in tension," *Highway Research Record*, no. 67, pp. 38–58, 1965.

[29] Y. H. Huang, "Deformation and volume change characteristics of a sand-asphalt mixture under constant direct and triaxial compressive stresses," *Highway Research Record*, no. 178, pp. 60–74, 1967.

[30] F. Moavenzadeh and J. Soussou, "Viscoelastic constitutive equation for sand-asphalt mixture," *Highway Research Record*, vol. 256, pp. 36–52, 1968.

[31] M. Perl, J. Uzan, and A. Sides, "Visco-elasto-plastic constitutive law for a bituminous mixture under repeated loading," *Transportation Research Record*, no. 911, pp. 20–27, 1983.

[32] Y. R. Kim, "One-dimensional constitutive modeling of asphalt concrete," *Journal of Engineering Mechanics*, vol. 116, pp. 751–772, 1990.

[33] A. C. Collop, D. Cebon, and M. S. A. Hardy, "Viscoelastic approach to rutting in flexible pavements," *Journal of Transportation Engineering*, vol. 121, no. 1, pp. 82–93, 1995.

[34] J. Eisenmann and A. Hilmer, "Influence of wheel load and inflation pressure on the rutting effect at asphalt pavements–experiments and theoretical investigations," in *Proc. Sixth International Conference on the Structural Design of Asphalt Pavements*, Ann Arbor, MI, 1987, pp. 392–403.

[35] L. W. Nijboer, *Plasticity as a Factor in the Design of Dense Bituminous Road Carpets*. Amsterdam, The Netherlands: Elsevier, 1948.

[36] C. Van der Poel, "On the rheology of concentrated dispersions," *Rheologica Acta*, vol. 1, no. 2, pp. 198–205, 1958.

[37] H. Frohlich and R. Sack, "Theory of the rheological properties of dispersions," vol. 185, no. 1003. The Royal Society, 1946, pp. 415–430.

[38] J. F. Hills, "The creep of asphalt mixes," *Journal of the Institute of Petroleum*, vol. 59, no. 570, pp. 247–262, 1973.

[39] C. Y. Cheung, A. C. F. Cocks, and D. Cebon, "Isolated contact model of an idealized asphalt mix," *International Journal of Mechanical Sciences*, vol. 41, no. 7, pp. 767–792, 1999.

[40] V. S. Deshpande and D. Cebon, "Steady-state constitutive relationship for idealised asphalt mixes," *Mechanics of Materials*, vol. 31, no. 4, pp. 271–287, 1999.

[41] V. S. Deshpande and D. Cebon, "Uniaxial experiments on idealized asphalt mixes," *Journal of Materials in Civil Engineering*, vol. 12, no. 3, pp. 262–271, 2000.

[42] C. Boutin and J. L. Auriault, "Dynamic behaviour of porous media saturated by a viscoelastic fluid: Application to bituminous concretes," *International Journal of Engineering Science*, vol. 28, no. 11, pp. 1157–1181, 1990.

[43] D. Florea, "Associated elastic/viscoplastic model for bituminous concrete," *International Journal of Engineering Science*, vol. 32, no. 1, pp. 79–86, 1994.

[44] D. Florea, "Nonassociated elastic/viscoplastic model for bituminous concrete," *International Journal of Engineering Science*, vol. 32, no. 1, pp. 87–93, 1994.

[45] J. M. Krishnan and C. L. Rao, "Mechanics of air voids reduction of asphalt concrete using mixture theory," *International Journal of Engineering Science*, vol. 38, no. 12, pp. 1331–1354, 2000.

[46] J. M. Krishnan and C. L. Rao, "Permeability and bleeding of asphalt concrete using mixture theory," *International Journal of Engineering Science*, vol. 39, no. 6, pp. 611–627, 2001.

[47] K. R. Rajagopal, "Multiple configurations in continuum mechanics," Institute for Computational and Applied Mechanics, Pittsburgh, PA, Tech. Rep. 6, 1995.

[48] K. R. Rajagopal and A. R. Srinivasa, "On the thermomechanics of materials that have multiple natural configurations Part I: Viscoelasticity and classical plasticity," *Zeitschrift für Angewandte Mathematik und Physik (ZAMP)*, vol. 55, no. 5, pp. 861–893, 2004.

[49] K. R. Rajagopal and A. R. Srinivasa, "On the thermomechanics of materials that have multiple natural configurations Part II: Twinning and solid to solid phase transformation," *Zeitschrift für Angewandte Mathematik und Physik (ZAMP)*, vol. 55, no. 6, pp. 1074–1093, 2004.

[50] J. M. Krishnan and K. R. Rajagopal, "On the mechanical behavior of asphalt," *Mechanics of Materials*, vol. 37, no. 11, pp. 1085–1100, 2005.

[51] M. Guler, P. J. Bosscher, and M. E. Plesha, "A porous elasto-plastic compaction model for asphalt mixtures with parameter estimation algorithm," *Geotechnical Special Publication*, vol. 123, pp. 126–143, 2002.

[52] S. Koneru, E. Masad, and K. R. Rajagopal, "A thermomechanical framework for modeling the compaction of asphalt mixes," *Mechanics of Materials*, vol. 40, no. 10, pp. 846–864, 2008.

[53] W. Moore, "Intelligent compaction: Outsmarting soil and asphalt," *Construction Equipment*, vol. 4, pp. 39–48, April 2006.

[54] F. Rahman, M. Hossain, and M. Hunt, "Intelligent compaction control of highway embankment soil," in *Compendium of Papers CD-ROM, The 86th Annual Transportation Research Board Meeting*, no. 07–2962, Washington DC, 2007.

[55] I. MathWorks, *MATLAB User Guide*. Natick, MA: The MathWorks Inc, 2007.

[56] A. Scarpas, *CAPA-3D Finite Element System Users Manual I, II, and III*. Delft, The Netherlands: TU Delft publication, 2000.

[57] A. Scarpas, *A Mechanics Based Computational Platform for Pavement Engineering*. Delft, The Netherlands: TU Delft Publication, 2004.

[58] L. Sluys, *Wave Propagation, Localisation and Dispersion in Softening Solids*. Delft, The Netherlands: TU Delft Publication, 1992.

[59] K. Bathe, *Finite Element Procedures*. Upper Saddle River, NJ: Prenctice Hall, 1995.

[60] K. Johnson, *Contact Mechanics*. New York: Cambridge University Press, 1987.

APPENDIX A

FUNCTIONS USED FOR FINITE ELEMENT NUMERICAL IMPLEMENTATION IN CAPA-3D

The following is a listing of the functions to be used in the numerical implementations involving the appropriate residual formulations in Chapter IV:

1. $\epsilon_1 = \dfrac{\mathrm{I}_{\mathbf{B}_{pe}} - 1 - \ln(\mathrm{III}_{\mathbf{B}_{pe}})}{2\sqrt{\mathrm{III}_{\mathbf{B}_{pe}}}}$
2. $\epsilon_2 = \dfrac{\left(\mathrm{I}_{\mathbf{B}_{pe}} - 3 - \ln(\mathrm{III}_{\mathbf{B}_{pe}})\right)}{2\sqrt{\mathrm{III}_{\mathbf{B}_{pe}}}}$
3. $\epsilon_3 = \mathrm{III}_{\mathbf{G}} \dfrac{\partial \mu}{\partial \mathrm{III}_{\mathbf{G}}} + \mu$
4. $\alpha_1 = -\mu\epsilon_1$
5. $\alpha_2 = \dfrac{\mu}{\sqrt{\mathrm{III}_{\mathbf{B}_{pe}}}}$
6. $k = \epsilon_2\epsilon_3$
7. $\alpha = -\hat{\mu} n_1 \lambda_1 q_1 \mathrm{III}_{\mathbf{G}}^{2n_1} \left(1 + \lambda_1 \mathrm{III}_{\mathbf{G}}^{2n_1}\right)^{(q_1 - 1)}$
8. $\beta = -\hat{\eta} n_2 \lambda_2 q_2 \mathrm{III}_{\mathbf{G}}^{2n_2} \left(1 + \lambda_2 \mathrm{III}_{\mathbf{G}}^{2n_2}\right)^{(q_2 - 1)}$
9. $\sigma = -\left(\alpha - \dfrac{\mu}{2}\right)\epsilon_1 + \dfrac{\alpha_2}{2}$
10. $\gamma = \dfrac{1}{2\sqrt{\mathrm{III}_{\mathbf{B}_{pe}}}}\epsilon_3$
11. $\omega = -\dfrac{\epsilon_1\epsilon_3}{2} + \epsilon_2 \left[\alpha - 2\hat{\mu} n_1^2 \lambda_1 q_1 \mathrm{III}_{\mathbf{G}}^{2n_1} (1 + \lambda_1 \mathrm{III}_{\mathbf{G}}^{2n_1})^{(q_1 - 2)} \left\{1 + \lambda_1 q_1 \mathrm{III}_{\mathbf{G}}^{2n_1}\right\}\right]$
12. $\delta = \dfrac{2\Delta t}{\eta}$

13. $\varphi_1 = \dfrac{\beta\alpha_2}{\eta} - \dfrac{1}{\sqrt{\mathrm{III}_{\mathbf{B}_{pe}}}}\left(\alpha - \dfrac{\mu}{2}\right)$

14. $\varphi_2 = \dfrac{\beta}{\eta}(\alpha_1 - k) - (\sigma - \omega)$

15. $\varphi_3 = \dfrac{\mu}{2\sqrt{\mathrm{III}_{\mathbf{B}_{pe}}}} + \gamma$

16. $\phi_1 = \dfrac{1}{\sqrt{\mathrm{III}_{\mathbf{B}_{pe}}}}\left(\alpha - \dfrac{\mu}{2}\right) - \dfrac{\beta}{\eta}\alpha_2 = -\varphi_1$

17. $\phi_2 = (\sigma - \omega) - \dfrac{\beta}{\eta}(\alpha_1 - k) = -\varphi_2$

18. $\phi_3 = \dfrac{\mu}{2\sqrt{\mathrm{III}_{\mathbf{B}_{pe}}}} + \gamma = \varphi_3$

APPENDIX B

ALGORITHMS FOR NUMERICAL IMPLEMENTATION IN CAPA-3D

An algorithm illustrating the actions necessary to obtain an updated value for $\mathbf{B}_{pe}$ at the current time integration step, $t + \Delta t$, is presented in Algorithm B.1.

Algorithm B.1 Calculation of $\mathbf{B}_{pe}^{t+\Delta t}$

Require: $\mathrm{III}_{\mathbf{G}} \leq 1 \, \forall \, t \geq 0$

Ensure: $\mathrm{III}_{\mathbf{F}_r} = \mathrm{III}_{\mathbf{G}} \sqrt{\mathbf{B}_{pe}} \, \forall \, t$

$\mathbf{B}_{pe} \leftarrow \mathbf{I}, \ when \ t = 0$

$Residual = 1$; $Iteration(k) = 0$; $Tolerance = 10^{-r}$

while $Residual > Tolerance$ **do**

$k = k + 1$

$$\frac{\partial \mathbf{R}^{(k-1)}}{\partial \mathbf{B}_{pe}^{(k-1)}} \Delta \mathbf{B}_{pe}^{(k)} = -\mathbf{R}^{(k-1)}$$

$$\mathbf{B}_{pe}^{(k)} \leftarrow \mathbf{B}_{pe}^{(k-1)} + \Delta \mathbf{B}_{pe}^{(k)}$$

$$Evaluate: \quad \left(\mathrm{I}_{\mathbf{B}_{pe}}\right)^{(k)}, \left(\mathrm{III}_{\mathbf{B}_{pe}}\right)^{(k)}$$

$$\left(\mathrm{III}_{\mathbf{G}}\right)^{(k)} = \left(\frac{\mathrm{III}_{\mathbf{F}_r}}{\sqrt{\left(\mathrm{III}_{\mathbf{B}_{pe}}\right)^{(k)}}} \right)$$

$$Residual \leftarrow \left(\Delta \mathbf{B}_{pe}^{(k)} \cdot \Delta \mathbf{B}_{pe}^{(k)} \right)^{1/2}$$

end while

$$\mathbf{B}_{pe}^{t+\Delta t} \leftarrow \mathbf{B}_{pe}^{(k)}$$

$$Evaluate: \quad \left(\mathrm{I}_{\mathbf{B}_{pe}}\right)^{t+\Delta t}, \left(\mathrm{III}_{\mathbf{B}_{pe}}\right)^{t+\Delta t}$$

$$\left(\mathrm{III}_{\mathbf{G}}\right)^{t+\Delta t} = \left(\frac{\mathrm{III}_{\mathbf{F}_r}}{\sqrt{\mathrm{III}_{\mathbf{B}_{pe}}}} \right)^{t+\Delta t}$$

$$Calculate: \quad \mathbf{T}^{t+\Delta t}, \mathbf{S}^{t+\Delta t}$$

An algorithm illustrating the actions necessary to obtain an updated value for $\mathbf{C}_{VE}^{-1}$ at the current time integration step, $t + \Delta t$, is presented in Algorithm B.2.

Algorithm B.2 Calculation of $\left(\mathbf{C}_{VE}^{-1}\right)^{t+\Delta t}$

Require: $\mathrm{III}_{\mathbf{G}} \leq 1 \, \forall \, t \geq 0$

Ensure: $\mathrm{III}_{\mathbf{F}_r} = \mathrm{III}_{\mathbf{G}} \sqrt{\mathbf{B}_{pe}} \, \forall \, t$

$\mathbf{C}_{VE}^{-1} \leftarrow \mathbf{I}, \ \textit{when } t = 0$

$\textit{Residual} = 1$; $\textit{Iteration}(k) = 0$; $\textit{Tolerance} = 10^{-r}$

while $\textit{Residual} > \textit{Tolerance}$ **do**

$k = k + 1$

$$\frac{\partial \mathbf{R}^{(k-1)}}{\partial \left(\mathbf{C}_{VE}^{-1}\right)^{(k-1)}} \Delta \left(\mathbf{C}_{VE}^{-1}\right)^{(k)} = -\mathbf{R}^{(k-1)}$$

$$\left(\mathbf{C}_{VE}^{-1}\right)^{(k)} \leftarrow \left(\mathbf{C}_{VE}^{-1}\right)^{(k-1)} + \Delta \left(\mathbf{C}_{VE}^{-1}\right)^{(k)}$$

$$\textit{Evaluate}: \quad \mathbf{B}_{pe}^{(k)}, \ \left(\mathrm{I}_{\mathbf{B}_{pe}}\right)^{(k)}, \ \left(\mathrm{III}_{\mathbf{B}_{pe}}\right)^{(k)}$$

$$\left(\mathrm{III}_{\mathbf{G}}\right)^{(k)} = \left(\frac{\mathrm{III}_{\mathbf{F}_r}}{\sqrt{\left(\mathrm{III}_{\mathbf{B}_{pe}}\right)^{(k)}}} \right)$$

$$\textit{Residual} \leftarrow \left(\Delta \left(\mathbf{C}_{VE}^{-1}\right)^{(k)} \cdot \Delta \left(\mathbf{C}_{VE}^{-1}\right)^{(k)} \right)^{1/2}$$

end while

$$\left(\mathbf{C}_{VE}^{-1}\right)^{t+\Delta t} \leftarrow \left(\mathbf{C}_{VE}^{-1}\right)^{(k)}$$

$$\textit{Evaluate}: \quad \mathbf{B}_{pe}^{t+\Delta t}, \ \left(\mathrm{I}_{\mathbf{B}_{pe}}\right)^{t+\Delta t}, \ \left(\mathrm{III}_{\mathbf{B}_{pe}}\right)^{t+\Delta t}$$

$$\left(\mathrm{III}_{\mathbf{G}}\right)^{t+\Delta t} = \left(\frac{\mathrm{III}_{\mathbf{F}_r}}{\sqrt{\mathrm{III}_{\mathbf{B}_{pe}}}} \right)^{t+\Delta t}$$

$$\textit{Calculate}: \quad \mathbf{T}^{t+\Delta t}, \ \mathbf{S}^{t+\Delta t}$$

Note: $\mathbf{B}_{pe}$ and $\mathbf{C}_{VE}^{-1}$ are related by the relation given in Chapter IV (A.3d).

VITA

Hailing from southern India, Saradhi Koneru enrolled in this university in the fall of 2004 in pursuit of his higher educational needs. After receiving his Bachelor of Engineering degree in mechanical engineering from the Osmania University, Hyderabad, India in June 2004 he acquired a Master of Science degree in mechanical engineering from Texas A&M University in December 2006. This manuscript has been submitted in accordance with the requirements for a Doctoral degree in Civil Engineering at the same institution. The author maybe contacted by email at koneru.saradhi@gmail.com or at the following address:

Department of Civil Engineering
Texas A&M University
3136 TAMU
College Station, Texas 77843-3136
USA

This document was typeset in LaTeX by Saradhi Koneru.